Finite Element Analysis of Glass Fiber Reinforced Polymer Bridge Decks

by

Cheng Zhang

A Thesis submitted to the Faculty of Graduate Studies of
The University of Manitoba
in partial fulfillment of the requirements for the degree of

MASTER OF SCIENCE

Department of Civil Engineering
University of Manitoba
Winnipeg, Manitoba

Abstract

Deterioration of concrete bridge decks has become a serious problem in the past few decades. Fortunately, non-corrosive, light-weight Fiber Reinforced Polymer (FRP) material provides an excellent alternative. More than 117 bridges in the USA have been built or repaired with FRP. In Canada, no FRP bridge deck has been used in the field, yet. However, Wardrop Engineering Inc., Faroex Ltd., and ISIS Canada have successfully designed, manufactured, and patented the filament-wound Glass Fiber Reinforced Polymer (GFRP) bridge deck. Since there is no design code for FRP bridge decks, a finite element method, labeled "L&D", is proposed in this thesis to help bridge engineers better understand the structural behavior of FRP bridge decks. The L&D method is validated by comparing the analysis results with the experimental results of three filament-wound GFRP bridge decks. This L&D method is also applicable for analyzing FRP bridge decks manufactured by other processes.

Acknowledgements

I would like to show my deepest gratitude to Dr. Aftab Mufti and Dr. Emile Shehata for their technical guidance and unceasing encouragement throughout this research project. The financial support from ISIS Canada Research Network and the Manitoba Government is gratefully acknowledged.

I would like to thank Dr. Douglas Thomson and Dr. Ahmed Shalaby for being part of my research team. Thanks are extended to Mr. Walter Saltzberg and Dr. Dimos Polyzois for their valuable suggestions regarding this research.

I am indebted to Dr. Brea Williams and Ms. Heather Wallace for providing me with valuable photos and experimental data regarding the filament-wound GFRP bridge decks.

I would like to express my thanks to Ms. Myrna Donald for editing this thesis. Continual support from fellow graduate students and structural laboratory technicians is deeply appreciated.

Dedication

To my parents

Table of Contents

List of Tables

List of Figures

List of Symbols and Abbreviations

Abbreviations

AASHTO	American Association of State Highway and Transportation Officials
CLT	Classical Lamination Theory
CP	Creative Pultrusions
CZM	Cohesive Zone Model
DCB	Double Cantilever Beam
ELS	End-Loaded Split
ENF	End-Notched Flexure
ESYS	Element Coordinate System
FHWA	Federal Highway Administration
FPF	First-Ply Failure
FRP	Fiber Reinforced Polymer
GFRP	Glass Fiber Reinforced Polymer
HC	Hardcore Composites
ISIS	Intelligent Sensing for Innovative Structures
KSCI	Kansas Structural Composites, Inc.
LAM	Linear Analysis Model
LN	Layer Number
LSG	Longitudinal Strain Gauge
LVDT	Linear Variable Differential Transformer
NL	Total Number of Layers

TSG	Transverse Strain Gauge
VARTM	Vacuum-Assisted Resin-Transfer Moulding
WTDCB	Width-Tapered Double Cantilever Beam

Symbols

d_n	debonding parameter
E	Young's modulus of the material
E_{11}	longitudinal Young's modulus of the lamina
E_{22}	transverse Young's modulus of the lamina
E_{33}	out-of-plane Young's modulus of the lamina
E_f	Young's modulus of fibers
E_m	Young's modulus of matrix
G_{12}	in-plane shear modulus of the lamina
G_{13}	out-of-plane shear modulus of the lamina (in 1-3 plane)
G_{23}	out-of-plane shear modulus of the lamina (in 2-3 plane)
G_c	critical fracture energy
G_{cn}	critical fracture energy for normal separation
G_{ct}	critical fracture energy for tangential slip
G_f	shear modulus of fibers
G_m	shear modulus of matrix
G_n	normal fracture energy
G_t	tangential fracture energy
K_n	normal contact stiffness

K_t	tangential contact stiffness
k_σ	stress concentration factor
k_τ	shear stress concentration factor
l_{cz}	length of the cohesive zone
P	normal contact stress
S_{12}	in-plane shear strength of the lamina
S_{1C}	longitudinal compressive strength of the lamina
S_{1T}	longitudinal tensile strength of the lamina
S_{2C}	transverse compressive strength of the lamina
S_{2T}	transverse tensile strength of the lamina
S_f	fiber tensile strength
S_{m12}	matrix shear strength
S_{mC}	matrix compressive strength
S_{mT}	matrix tensile strength
t	thickness of an adjacent sublaminate
$\overline{u}_n$	contact gap at the maximum normal contact stress
u_n^c	contact gap at the completion of debonding
u_n	contact gap
V_f	fiber volume fraction
V_m	matrix volume fraction
α	a parameter much larger than 1 ($\alpha \gg 1$)
α_{frpL}	coefficient of thermal expansion of fibers in the longitudinal direction

α_{frpT}	coefficient of thermal expansion of fibers in the radial direction
ε_{ft}^{u}	ultimate tensile strain of fibers
ε_{mt}^{u}	ultimate tensile strain of matrix
ε_{rm}	maximum residual radial strain
ξ_3	failure index of Tsai-Wu failure criterion
ξ_f	safety factor for the actual state of stress $(\sigma_1, \sigma_2, \tau_{12})$
σ_1	longitudinal stress in the lamina
σ_2	transverse stress in the lamina
σ_{max}	maximum normal contact stress
σ_{rm}	maximum residual radial stress
τ^o	maximum interfacial strength
τ_{12}	in-plane shear stress in the lamina
τ_{max}	maximum equivalent tangential contact stress
υ_{12}	major Poisson's ratio of the lamina
υ_f	Poisson's ratio of fibers
υ_m	Poisson's ratio of matrix

List of Appendixes

Chapter 1

Introduction

1.1 Status of Bridges in North America

Based on data provided by the Federal Highway Administration (FHWA), the total number of bridges in the USA as of December 2008 was 601,411. About half of these bridges (291,335) are more than 40 years old. Among these old bridges, 20.3% (59,128) are classified as structurally deficient; 19.2% (55,947) are classified as functionally obsolete (Federal Highway Administration, 2009). Structural deficiencies and functional obsolescence are not mutually exclusive. However, a bridge, which is both structurally deficient and functionally obsolete, is identified only as structurally deficient, because structural deficiencies are more crucial regarding safety concerns (Federal Highway Administration; Federal Transit Administration, 2006).

Zureick et al. (1995) discovered that concrete deck deterioration is the main reason for bridges being categorized as “deficient”. Cracking and spalling of concrete and corrosion of steel rebars, considered extremely undesirable by bridge engineers, are ubiquitous across North America. It is apparent that severe climate in North America, extensive use

of de-icing salts, and ever-increasing traffic loads are the key factors causing damage to concrete bridge decks. Unfortunately, these outside factors can never be changed. The governments of Canada and of the USA have to spend millions of dollars on repairing and maintaining these deficient bridge structures every year.

The traditional concrete deck repair approach is to replace unsound concrete and deteriorated reinforcing steel with new reinforced concrete. This repair method is time-consuming and labor intensive, and causes economic loss due to traffic delay. At best, this technique delays the deterioration process, and does not solve the problem completely. Many material scientists and engineers are trying to find a noncorrosive material as a substitute for reinforced concrete. FRPs are now available as a possible solution.

FRPs were originally used in the aerospace and automotive industries where their high strength-to-weight ratio and corrosion resistance were extremely beneficial (Telang et al., 2006). In the last two decades, the use of FRPs in the construction industry has been booming. Several commercial FRP manufacturers and universities successfully developed FRP bridge decks as replacements for conventional deck systems.

1.2 Objective

More than 117 bridges in the USA have been built or repaired with FRP (O'Connor, 2008). FRP bridge decks are becoming more and more popular around the world. Despite this popularity, there are no design guidelines available for the design of bridges with

FRP decks. Without guidelines, it is quite difficult for bridge engineers to understand and predict the structural performance and failure mechanism of FRP bridge decks. The focus of this research is to develop a systematic method for analysis of FRP bridge decks using currently available finite element technology.

A total of four generations of filament-wound GFRP bridge decks were designed and manufactured by industrial partners. All of these decks were tested at the McQuade Structural Laboratory, The University of Manitoba (Williams, 2000a; Crocker et al., 2002; Dawood, 2003). The proposed finite element method was employed to analyze the second-generation, third-generation and fourth-generation filament-wound GFRP bridge decks. The validity of this analytical method can be assessed by comparing its results with the test results. This finite element method is applicable for FRP bridge decks manufactured by other processes, such as hand lay-up, VARTM, and pultrusion, too.

1.3 Thesis Organization

This thesis is organized into five chapters. The specific chapters of the thesis are as follows:

Chapter 1 – Introduction: This chapter provides general information on current bridge conditions in North America, the objective of this thesis, and the thesis organization.

Chapter 2 – Background of FRP Bridge Decks: This chapter provides background information on FRP material and its mechanical properties, different manufacturing

methods of FRP bridge decks, the benefits and challenges of FRP bridge decks, and the development of FRP bridge decks in the USA and Canada.

Chapter 3 – Summary of Experimental Research: This chapter provides detailed information of the second-generation, third-generation and fourth-generation filament-wound GFRP bridge decks, including dimensions, design parameters, material properties, test setup, instrumentation, and test results.

Chapter 4 – Validation Study of a Finite Element Method against Experimental Results: This chapter provides a finite element method for the analysis of FRP bridge decks, and the comparison between analysis results and test results of the second-generation, third-generation and fourth-generation filament-wound GFRP bridge decks.

Chapter 5 – Conclusions and Recommendations: This chapter provides the conclusions of this thesis, and recommendations for future work.

Chapter 2

Background of FRP Bridge Decks

2.1 FRP Material

Different from conventional construction materials, FRP is an engineered material. Engineers can design the material properties and structural shapes of FRPs based on their requirements. Therefore, it is essential to know the composition of FRP material.

FRP material consists of two major components: a polymer matrix resin and fiber reinforcements. Fillers and additives, as a third component, can improve certain characteristics of the final product.

2.1.1 Matrix Resin

The main functions of matrix resins are creating volume, transferring stresses between fibers, protecting fibers from mechanical and environmental damage, and providing lateral support to fibers against buckling.

Two types of polymeric matrices are widely used for FRP composites: thermosetting polymers and thermoplastic polymers. Thermosetting polymers are low molecular-weight liquids with very low viscosity, and their molecules are connected through chemical cross-links (Newhook and Svecova, 2007). During the curing process, the cross-linking process generates a molecule with a larger molecular weight, which increases the melting point of the material. Thermosetting polymers cannot be reshaped after curing, because uncontrolled reheating causes the material to reach its decomposition temperature before its increased melting point (Plastic Plus, Inc., 2009). On the contrary, thermoplastic polymers are usually not highly cross-linked. They are held in place by weak secondary bonds that can be broken by heat or pressure, which means thermoplastic polymers can be remelted and remoulded as many times as necessary (Newhook and Svecova, 2007). Currently, only thermosetting polymers are being used in manufacturing FRP bridge decks (Telang et al., 2006). The most desirable thermosetting resins are epoxies, polyesters, and vinyl esters. Table 2.1 lists the typical mechanical properties of these three types of resins.

Table 2.1: Typical mechanical properties of common resins (Newhook and Svecova, 2007)

Resin	Specific Gravity	Tensile Strength [MPa]	Tensile Modulus [GPa]	Cure Shrinkage [%]
Epoxy	**1.20-1.30**	**55.00-130.00**	**2.75-4.10**	**1.00-5.00**
Polyester	**1.10-1.40**	**34.50-103.50**	**2.10-3.45**	**5.00-12.00**
Vinyl Ester	**1.12-1.32**	**73.00-81.00**	**3.00-3.35**	**5.40-10.30**

2.1.2 Fiber Reinforcement

The main functions of fiber reinforcements are carrying the applied load, and providing strength and stiffness to FRP composites. The fiber reinforcements are usually oriented in the direction of the primary loads.

There are a large variety of fibers available in the composites industry. The desirable features of fiber reinforcements are high strength, high stiffness, good durability, and low cost. Table 2.2 presents the mechanical properties of three commonly used fibers: carbon, aramid and glass. Until recently, only E-glass fiberglass and high-strength carbon fibers were successfully used to manufacture bridge decks due to their competitive prices and wide-ranging availability.

Table 2.2: Typical mechanical properties of fibers (Newhook and Svecova, 2007)

FIBER TYPE		Tensile Strength [MPa]	Modulus of Elasticity [GPa]	Elongation [%]	Coefficient of Thermal Expansion [$\times 10^{-6}$]	Poisson's Ratio
CARBON						
PAN	High Strength	3500	200-240	1.3-1.8	(-1.2) to (-0.1) (α_{frpL}) 7 to 12 (α_{frpT})	-0.2
	High Modulus	2500-4000	350-650	0.4-0.8		
Pitch	Ordinary	780-1000	38-40	2.1-2.5	(-1.6) to (-0.9) (α_{frpL})	N/A
	High Modulus	3000-3500	400-800	0.4-1.5		
ARAMID						
Kevlar 29		3620	82.7	4.4	N/A	0.35
Kevlar 49		2800	130	2.3	-2.0 (α_{frpL}), 59 (α_{frpT})	
Kevlar 129		4210 (est.)	110 (est.)	- -	N/A	
Kevlar 149		3450	172-179	1.9	N/A	
Twaron		2800	130	2.3	(-2.0) (α_{frpL}), 59 (α_{frpT})	
Technora		3500	74	4.6	N/A	
GLASS						
E-Glass		3500-3600	74-75	4.8	5.0	0.2
S-Glass		4900	87	5.6	2.9	0.22
Alkali Resistant Glass		1800-3500	70-76	2.0-3.0	N/A	N/A

Note:

α_{frpL} = coefficient of thermal expansion of fibers in the longitudinal direction

α_{frpT} = coefficient of thermal expansion of fibers in the radial direction

N/A = not available

Reinforcing fibers are thin, high-strength strands. They are usually bundled together to create a thicker strand named a "roving". Roving is the lowest usable form of reinforcement and it can be directly used in some manufacturing procedures. Roving can also be further processed into more complicated forms, and then used for fabrication. The typical forms of fiberglass and carbon reinforcements are continuous roving, discontinuous roving, woven roving, mat, and non-crimp fabric (Telang et al., 2006). Detailed information about these fiber reinforcement forms can be found readily on the websites of major FRP manufacturers.

2.1.3 Other Constituents

a. Fillers

The purposes of adding fillers into the matrix resin are as follows:

- To take up volume and reduce the overall cost;
- To enhance the mechanical properties;
- To reduce the cracking and shrinkage;
- To improve resistance to environmental corrosion;
- To control the viscosity; and,
- To reach higher temperature of polymerization.

Commonly used fillers are clay, silica, mica, calcium carbonate, aluminum trihydrate.

b. Additives

The main functions of additives are:

- To control the curing rate;

- To reduce shrinkage during curing;
- To improve the weathering resistance;
- To control the viscosity;
- To reduce the porosity; and,
- To color the final products.

Besides fillers and additives, other constituents involved in the manufacturing of FRP products are adhesives, foam cores, and gelcoat.

2.2 Manufacturing Methods of FRP Bridge Decks

The following sections give general descriptions of methods used in manufacturing FRP bridge decks. Each manufacturing method has its own advantages and disadvantages, so FRP bridge deck designers need to choose the most appropriate method to manufacture their FRP products.

2.2.1 Hand Lay-up

Hand lay-up is the oldest and simplest method for composite manufacturing, and it is still widely used in the composite industry. Before hand lay-up begins, the mold is treated with several layers of release wax to make sure the part can be released from the mold easily. Dry fiber reinforcements can be laid in the mold according to the requirements of design engineers. The lay-up crew uses brushes or rollers to impregnate the fibers with the resin. It is important for the crew to control the amount of resin and the quality of

saturation. After the layer is fully saturated, the crew repeats the process until the lamination is complete. Then, the part is left to cure at standard atmospheric pressure and room temperature for a few hours. At last, the part is removed from the mold and may need final trimming and surface preparation. The schematic of the hand lay-up process is shown in Figure 2.1.

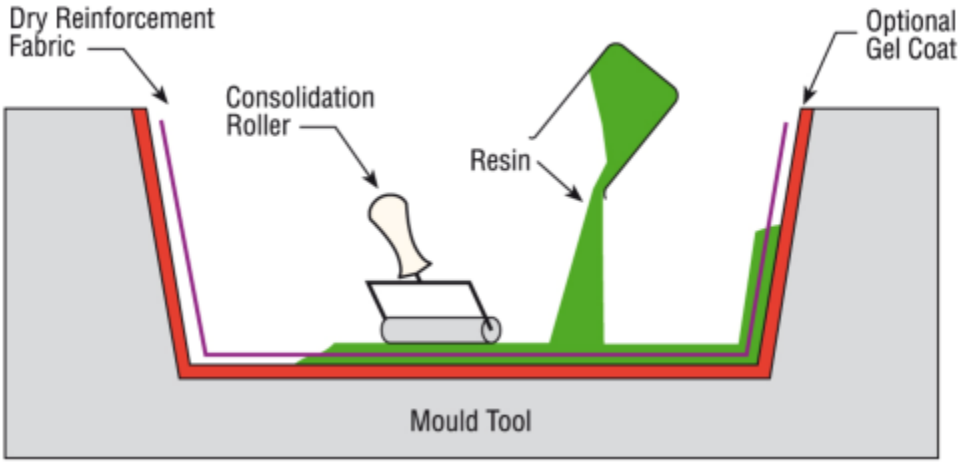

Figure 2.1: Schematic of the hand lay-up process (Gurit, 2009)

The advantages and disadvantages of the hand lay-up manufacturing method are presented as follows.

Advantages:

- Widely accepted and simple to learn;
- Low capital equipment costs;
- Wide choice of suppliers and material types;
- Design changes are easy to realize;
- The least expensive method for small volume production; and,
- Possibility to manufacture large and complex products.

Disadvantages:

- Quality is very dependent on the laborers' skills;
- Labor intensive;
- Health and safety considerations;
- Waste factor can be high; and,
- Low viscosity resins are more workable by hand, but their mechanical and thermal properties are compromised due to high diluent/styrene level (Gurit, 2009).

2.2.2 Vacuum-Assisted Resin-Transfer Molding (VARTM)

The VARTM method, also called vacuum infusion process molding, is a liquid molding process used to manufacture large-scale composite structures. A vacuum bag is placed over the part to form a vacuum-tight seal. The vacuum pump creates about 1 atm pressure gradient within the bag, which is sufficient to draw the resin into the mold and impregnate the dry fiber reinforcement (Adams et al., 2003). The part is allowed to cure under atmospheric pressure without heat. Figure 2.2 shows the VARTM process on Tycor reinforced bridge deck.

Figure 2.2: VARTM process on Tycor reinforced bridge deck (Telang et al., 2006)

The advantages and disadvantages of the VARTM manufacturing method are presented as follows.

Advantages:

- Rapid infusion of large parts, as seen in Figure 2.2;
- Flexibility in design variations on a deck-to-deck basis;
- High fiber volume fraction can be reached;
- Good dimensional tolerance;
- Relatively low cost for small volume production; and,
- Fewer environmental concerns.

Disadvantages:

- Volumetrically nearly solid sections are required to prevent resin-rich areas or resin pools in cavities (Telang et al., 2006);
- Foam core has to sustain the atmospheric pressure without damage; and,
- Cost of bagging materials.

2.2.3 Pultrusion

Pultrusion is a continuous process for manufacturing composite materials with constant cross-section. The raw fiber reinforcements, rolls of fiber mat or doffs of fiber roving, are pulled through a resin bath or resin impregnation system. As the fibers are fully wet-out, the preforming system squeezes out the excess resin and positions the fibers into the correct shape. Then, a heated steel die is used to initiate the gelation of thermosetting resin. After curing, the rigid profile, which has the same shape as the die, is cut to the

desired length and ready for delivery. The schematic of the pultrusion process is presented in Figure 2.3.

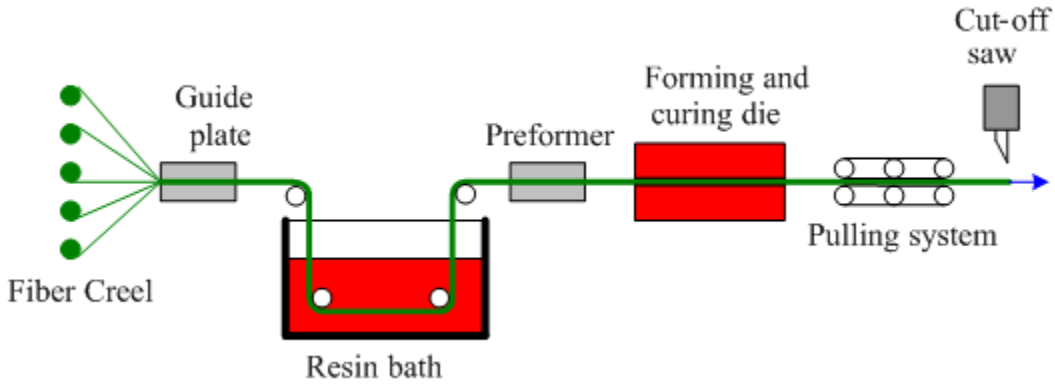

Figure 2.3: Schematic of the pultrusion process (Kopeliovich, 2009)

The advantages and disadvantages of the pultrusion manufacturing method are presented below.

Advantages:

- Well-controlled and consistent dimensional profile;
- Highly automated, and low labor required;
- High fiber volume fraction;
- Good mechanical properties;
- High production rate;
- Low cost; and,
- Open or wrap-around shapes are allowed in the design of internal die segments.

Disadvantages:

- Tapered and complex shapes cannot be pultruded;
- High capital equipment cost;

- Mats and fabrics are needed to get transverse strength;
- Suitable only for large volume production;
- Shrinkage (normally 2% - 3%) is difficult to control (Bhat, 2009); and,
- Voids could result in parts if too much opening is given at the die entrance.

2.2.4 Filament Winding

Filament winding is a composite manufacturing method for fabricating parts with high fiber volume fraction and precise fiber orientation. The fibers are first directed into a resin bath system before winding, which is called "wet-winding" in the composite industry (Lee, 1989). Then, the impregnated fibers are wound on the mandrel in a geometrical pattern predesigned by the composite engineer. This winding process is implemented by rotating the mandrel while a carriage moves horizontally to lay down fibers on the mandrel surface. The angle at which the fiber is laid down has significant influence on the mechanical property of the final part. A large angle "hoop" or "circumferential" layer will enhance crush strength, while a small angle "closed" or "helical" layer will improve the longitudinal strength. When the mandrel is wound to the desired thickness, depending upon the chemical characteristic of the resin system, it may be placed in an oven to cure the resin or just left at room temperature. Once the resin has cured, the mandrel can be removed, or can be left as an integral component of the part. Figure 2.4 shows the schematic of the filament winding process.

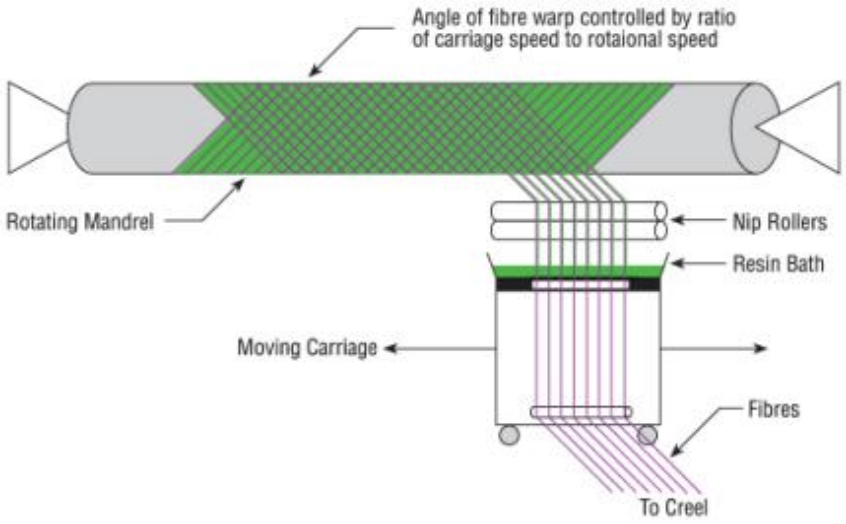

Figure 2.4: Schematic of the filament winding process (Gurit, 2009)

The advantages and disadvantages of the filament winding manufacturing method are presented below.

Advantages:

- Automated process results in cost savings;
- Excellent material properties;
- Highly reproducible (layer to layer, part to part);
- High fiber volume fraction;
- Continuous fiber over the whole part; and,
- Controllable fiber orientation angle (from 10° to 90°).

Disadvantages:

- High capital equipment cost;
- Cost and design constraints of removable mandrels;
- Incapability of winding on concave surfaces; and,
- Wound external surface is not smooth enough for certain applications.

2.3 Benefits and Challenges of FRP Bridge Decks

FRP bridge decks have successfully transitioned over the past decade from the experimental research stage to the field application stage. More than 100 bridges have been built or repaired with FRP bridge deck systems in the USA alone. This section summarizes the main benefits and challenges of FRP bridge decks based on their laboratory results and field performances.

The benefits of using FRP bridge deck systems are summarized as follows:

1) Non-corrosive properties of FRP material can extend the service life of FRP bridge deck;
2) High quality results from well controlled factory environment;
3) Construction of FRP bridge decks is easier and faster than conventional bridge deck construction, which leads to less traffic control time, and less negative environmental impact;
4) Lightweight FRP bridge decks make it possible to increase the live load carrying capacity of a bridge without retrofitting its substructure;
5) Compared with conventional materials, FRP material has high strength but relatively low stiffness. Since the design of FRP bridge deck systems is based on stiffness requirements, this innovative bridge deck has a very high safety factor;
6) For the bridges in seismically active zones, lightweight FRP bridge deck is the optimal option because of its lower inertia force (Aref and Parsons, 2000);
7) FRP bridge decks are excellent replacements for 19^{th} and 20^{th} century steel truss bridges and moveable bridges because they can reduce deck dead load, improve

bridge live load capacity, and allow certain bridges to be widened (Sams, 2005); and,

8) According to the projected durability of FRP material, costs of bridge deck replacement and maintenance are significantly reduced, which results in lower life cycle costs.

Although many benefits have been proven by laboratory tests and field projects, there are still some challenges in the use of FRP bridge deck systems:

1) High initial cost is the major barrier to develop the FRP bridge deck market. Constrained construction budgets make it difficult to justify dedicating more funds in the beginning even though the life cycle cost of FRP bridge decks is relatively lower;
2) The design of FRP bridge deck is based on finite element analysis. No official guidelines nor specifications for the design and construction of FRP bridge decks are available on the market;
3) The lightweight attribute of FRP bridge decks may cause the bridge superstructure to be aerodynamically unstable, especially for large-scale bridges (Tang, 2003);
4) For field installation, the joint details need to be examined and further developed, which include joints between FRP panels, joints between FRP deck and superstructure, and joints between FRP deck and traffic railing;
5) Durability of the wearing surface needs to be well addressed;

6) Exchange of knowledge is still required between composite engineers and bridge engineers; and,
7) A database for each FRP bridge deck system needs to be available to bridge engineers in a format consistent with their procedures (Reeve, 2002).

2.4 Development of FRP Bridge Decks in the USA

In the USA, the first vehicular bridge using a FRP deck system was built in 1996 over an unnamed creek in the state of Kansas (O'Connor, 2008). After that, 117 more bridges were built or retrofitted with FRP bridge decks. Figure 2.5 shows the geographic distribution of these projects in the USA according to 2004 data.

Figure 2.5: Number of FRP decks and superstructures in the USA (O'Connor, 2008)

Over the past ten years, E-glass fiber has widely been used due to its low price. Vinyl ester resin is favored because of its long term durability. Deck panels are assembled in

the factory to ensure their quality, and then delivered to the bridge site. After site preparation work, deck panels are bonded together and secured to the girders. Thin polymer concrete or asphalt is poured on top of the deck surface to prevent the deck from damage while providing a smooth and skid-resistant surface.

As with the conventional bridge decks, GFRP bridge decks must meet the design criteria. GFRP decks are sufficient to carry AASHTO HS-20 or HS-25 design truck loading with an impact factor of 0.3. Due to the low modulus of elasticity of GFRP decks, deflection criterion always controls the design. The typical deflection criterion requires the span to deflection ratio to be between 500 and 800 (Telang et al., 2006). Because GFRP materials may creep under sustained loading, dead load strains are limited to 10% of ultimate strains. Total stresses are kept under 20% (O'Connor, 2008). Although GFRP deck designers try to establish composite behavior between GFRP decks and bridge girders, no composite action is assumed in the design. Connections must be carefully designed to withstand the horizontal shear forces. Besides these design criteria, bridge owners may have additional design requirements based on their specific needs.

It is interesting to note that unlike conventional construction products, there are only a few GFRP deck manufacturers that serve the whole country. Table 2.3 gives a list of known GFRP deck suppliers to the USA market. As shown in this table, each manufacturer has its own preferred manufacturing process. According to the statistical data of O'Connor (2008), 82 percent of the completed projects have been supplied by four

major GFRP deck manufacturers. These companies are Martin Marietta Composites, Hardcore Composites, Kansas Structural Composites, and Creative Pultrusions.

Table 2.3: Known GFRP deck suppliers to the USA market (O'Connor, 2008)

	Supplier (website)	aka	State	#[2]	Process	Tradename
1	Atlantic Research Corp	ARC	VA	1	Pultrusion	EZ-Span
2	Bedford Plastics Inc (www.bedfordplastics.com)	BPI	PA	4		Pro-Deck
3	Composite Advantage	CA	OH	3	VARTM	
4	Composite Deck Solutions	CDS	OH	1	Pultrusion	
5	Creative Pultrusions Inc) (www.creativepultrusions.com	CP	PA	9	Pultrusion	Superdeck H-Deck
6	Fiber Reinforced Systems Ltd (www.fiberreinforcedsystems.com)	FRS	OH	2	Pultrusion	TechDeck
7	Hardcore Composites (www.hardcorecomposites.com)	HC	DE	28	VARTM[1]	
8	Infrastructure Composites International Inc (www.infracomp.com)	ICI	CA	1	Open mould lay-up	
8	Kansas Structural Composites Inc (www.ksci.com)	KSCI	KS	9	Open mould lay-up	
10	Martin Marietta Composites (www.martinmariettacomposites.com)	MMC	NC	28	Pultrusion	DuraSpan
11	MFG Construction Products Inc	MFG	CA	2		
12	Strongwell (www.strongwell.com)	Str	VA	5	Pultrusion	EXTREN
13	Wagners Composite Fibre Technologies (www.wagner.com.au)	WCFT	AUS	3	Pultrusion	
14	Webcore Technologies/Comptek	W	OH	2	VARTM	TYCOR
15	E.T. Techtonics	ETT	PA	ped	Pultrusion	
16	ZellComp (www.zellcomp.com)	ZC	NC	2	Pultrusion	

* Systems that have been used in the USA
[1] VARTM = vacuum assisted resin transfer moulding
[2] # completed projects; ped = supplies pedestrian bridges only

The DuraSpan® FRP bridge deck system is developed by Martin Marietta Composites, which is a subsidiary of Martin Marietta Materials. Pultrusion technology is employed to fabricate the trapezoid cross-sectional panels (Martin Marietta Composites, 2005). These panels are glued together using epoxy or urethane adhesive through their tongue-and-groove connections. If more stiffness is required, additional facesheets are used on the contiguous top and bottom surfaces. Currently, DuraSpan® decks have two configurations: DuraSpan® 500 and DuraSpan® 766. DuraSpan® 500 has a depth of 127 mm and can span up to 1.52 m beam spacing; DuraSpan® 766 has a depth of 195 mm and can span up to 3.05 m beam spacing.

Hardcore Composites (HC) is specialized in manufacturing FRP decks with various forms of VARTM technology. Since a vacuum is applied to draw resin, the HC decks are typically the solid core sandwich type. HC has successfully designed various sandwich core patterns, but Telang et al. (2006) find that the majority of decks in service use vertical standing foam boxes wrapped with fiberglass fabric and arranged in a regular array as shown in Figure 2.6.

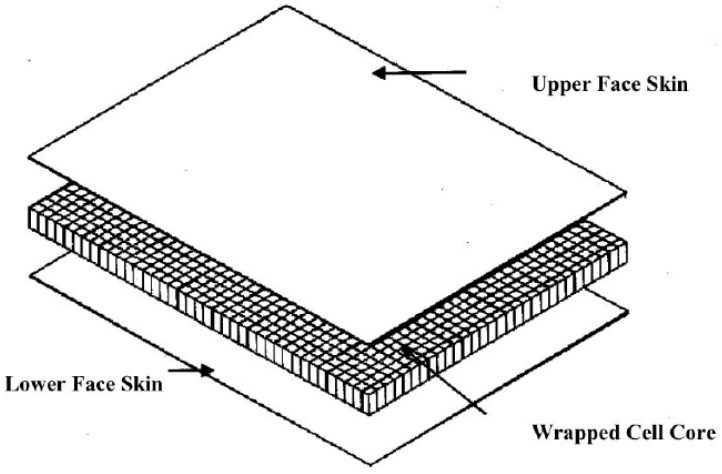

Figure 2.6: HC filled-core sandwich deck detail (Telang et al., 2006)

Kansas Structural Composites, Inc. (KSCI) was the first company in the USA to build a bridge with FRP panels. This No-Name Creek Bridge is 7.01 m long and 8.23 m wide, and is designed to carry AASHTO HS-25 truck loadings in both lanes. KSCI's sandwich-type deck consists of a top facesheet, a bottom facesheet, and a deep corrugated core (Kansas Structural Composites, Inc., 1999). Since KSCI uses the open-mold hand lay-up method to manufacture its deck panels, size, weight, and thickness of the sandwich panel can be easily adjusted to meet design needs.

Creative Pultrusions (CP), in partnership with West Virginia University, developed a FRP bridge deck system named Superdeck^{TM}. The pultrusion process is used to manufacture two types of beam-like components. The bridge truss component has a half-depth trapezoid cross-section, and the bridge shear key component has a full-depth hexagon cross-section (Creative Pultrusions, Inc., 2009). Bridge trusses and bridge shear keys are glued together to form the desired width of deck. The Superdeck^{TM} has a depth of 203 mm and can span up to 2.74 m beam spacing. As pultruded products, Superdeck^{TM} is quite similar to DuraSpan® deck in many areas. It is worth noting that CP has been manufacturing both the Superdeck^{TM} and DuraSpan® lines.

As described in Section 2.2.4, filament winding is an efficient, economical, automated composite manufacturing method. However, no field FRP bridge decks are fabricated by this process (Telang et al., 2006). Researchers are still working on building a structurally efficient and economic filament-wound FRP bridge deck. For instance, the University of Illinois at Urbana-Champaign completed an NCHRP-IDEA Project 63 entitled

"Manufacture and Testing of a Filament-wound Composite Bridge Superstructure" in 2002. This research project uses the filament-wound bridge superstructure conceptual design proposed by Aref and Parsons (2000). As shown in Figure 2.7, the bridge superstructure consists of two components: a series of filament-wound oval inner cells lying parrallel to the traffic direction, and a filament-wound outer shell. Several one tenth scale size filament-wound bridge superstructures were successfully fabricated in their laborotary. The specimens were tested under both static and fatigue loads to examine their structural performances. Finite element models were also developed to predict the stiffness and first-ply failure load of the specimens. The detailed manufacturing process and test results were reported in Parsons et al. (2002).

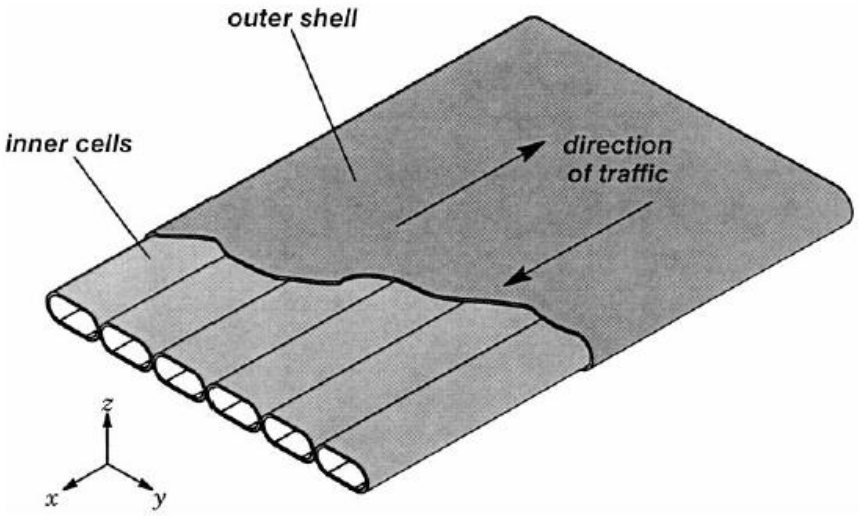

Figure 2.7: Filament-wound bridge superstructure design (Aref and Parsons, 2000)

2.5 Development of FRP Bridge Decks in Canada

There are no field FRP bridge deck projects in Canada, but researchers in Manitoba are trying to develop an efficient and high performance filament-wound GFRP bridge deck

system. Wardrop Engineering Inc. designed a total of four generations of GFRP deck panels. These deck panels were manufactured by Faroex Ltd. and tested by ISIS Canada at the W.R. McQuade Structures Laboratory. Figure 2.8 shows the cross-sections of four generations of filament-wound GFRP decks. Note that all the dimensions in this figure are in millimeters.

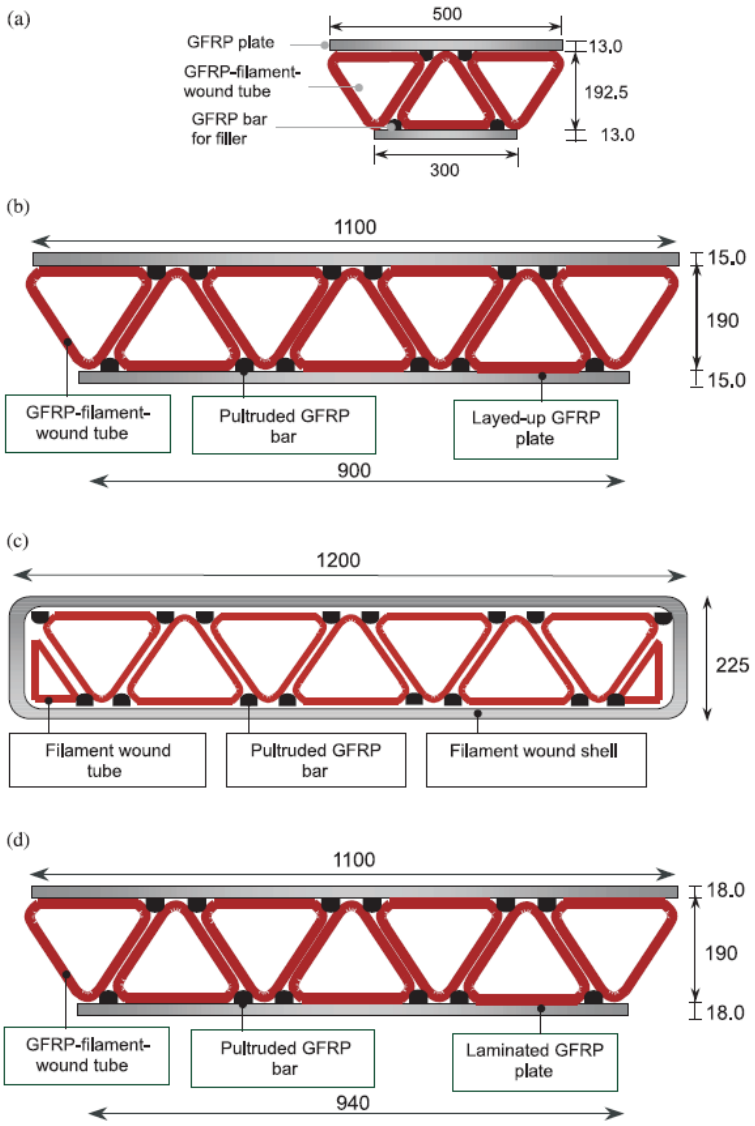

Figure 2.8: Schematic of filament-wound GFRP deck cross-sections: (a) first-generation GFRP bridge deck; (b) second-generation GFRP bridge deck; (c) third-generation GFRP bridge deck; and (d) fourth-generation GFRP bridge deck (Shehata and Mufti, 2007)

The first-generation GFRP bridge deck consisted of three filament-wound triangular tubes, four filler bars, and two laminated, pultruded plates. All these components were bonded by epoxy resin. After the assembly, the whole deck was wrapped in a plastic bag and cured at 82°C for 8-10 hours. Static test results showed that the primary failure mode of the first-generation GFRP deck was the delamination buckling of the outside plates, which resulted from an insufficient bond between the plies of the outside plate (Williams, 2000a).

Some improvements were made to the second-generation GFRP bridge deck. Instead of three inside tubes, the second-generation GFRP deck had seven filament-wound triangular tubes. The top and bottom deck plates were fabricated by hand lay-up process. The deck was assembled and wrapped in plastic sheeting. Resin infusion process was employed to glue all components into one piece, and then followed by curing. Internal failure, tube layer delamination and tube slippage were the failure modes of the second-generation GFRP bridge deck (Williams, 2000a).

The third-generation GFRP bridge deck had seven equilateral triangular tubes and two end triangular tubes. After positioning all nine triangular elements and pultruded GFRP filler bars, the entire section was filament wound and then infused with resin. Two-million load cycles was applied to the specimen, and no damage was found after the cyclic testing. Then the deck specimen was statically loaded to failure to determine its ultimate capacity. The final failure mode of this specimen was delamination buckling between two of the middle triangular tubes. It was proven that the filament-wound

outside shell was sufficient to provide bending stiffness, and the third-generation GFRP bridge deck had excellent fatigue resistance (Crocker et al., 2002).

The fourth-generation GFRP bridge deck consisted of seven filament-wound triangular tubes, twelve pultruded filler bars, and two laminated, pultruded plates. All components were bonded together through the resin infusion process and followed by curing. The fourth-generation GFRP deck had the optimum amount of fibers, which made it the most cost-effective deck of all four generations. The specimen exhibited very good structural performances during the static test, and finally failed due to delamination buckling that lead to punching around the loading plate (Crocker et al., 2002).

After the success of the fourth-generation GFRP bridge deck, a hollow, filament-wound, triangular shear key was developed to connect adjacent bridge deck panels, as shown in Figure 2.9. The load was applied at an eccentricity of 190 mm to the specimen longitudinal centerline. After two million load cycles, the shear-keyed specimen lost only three percent of its original stiffness. Then the specimen was statically tested to failure. The observed failure mode of this specimen was the punching failure at the load point. Overall, the shear key connection can effectively transfer the load between two adjacent panels with extremely small deflection difference. A detailed description of the shear keyed GFRP bridge deck test was reported in Dawood (2003).

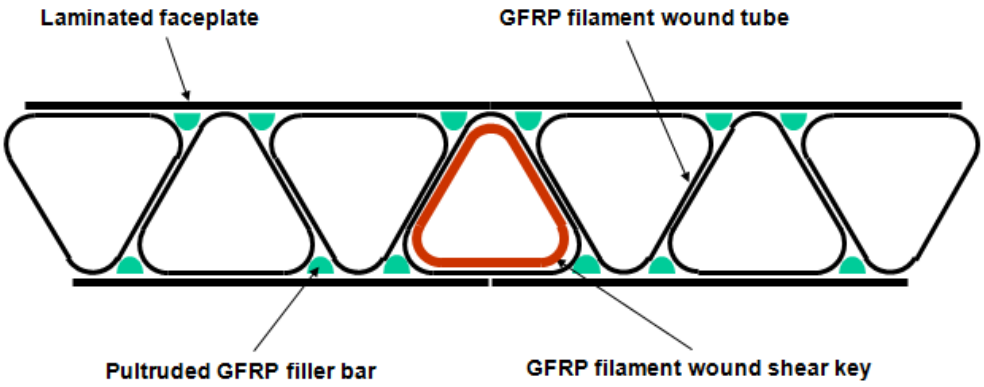

Figure 2.9: Schematic of the shear keyed GFRP deck cross-section (Crocker, 2001)

Chapter 3

Summary of Experimental Research

3.1 General

The experimental study for filament-wound GFRP bridge decks was done as part of extensive research program at ISIS Canada (Williams, 2000a; Crocker et al., 2002; Dawood, 2003). The purpose of the experimental research was to check whether the structural behavior of filament-wound GFRP bridge decks satisfied the requirements of AASHTO specifications, and to validate the accuracy of the proposed finite element method.

Since the first-generation GFRP bridge deck was the preliminary design of the whole filament-wound GFRP bridge deck project, some design and manufacturing defects were found by Williams (2000a). Therefore, only the experimental programs of the second-generation, third-generation and fourth-generation GFRP bridge decks are described in this chapter.

3.2 Second-generation GFRP Bridge Deck

There were two specimens of the second-generation GFRP bridge deck, designated as F7-1 and F7-2 respectively (Williams, 2000a). Based on the manufacturing experience of deck F7-1, several manufacturing details were improved in the fabrication of deck F7-2, such as the cross-section of GFRP filler bars and the number of plate layers. Test results demonstrated the better structural performance of deck F7-2, therefore deck F7-2 was chosen as the representative of the second-generation GFRP bridge deck.

Figure 3.1 shows the cross-section of deck F7-2, and also some of the main dimensions.

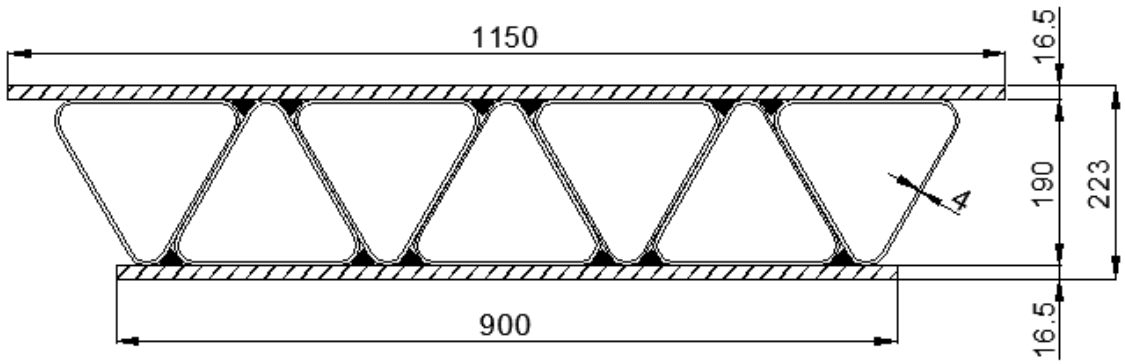

Figure 3.1: Cross-section of filament-wound GFRP bridge deck F7-2 (Unit: mm)

Deck F7-2 consisted of seven filament-wound equilateral-triangular tubes, two laid-up plates, and twelve pultruded GFRP bars. Each inside tube was filament wound in a sequence of [90/±45/±10/±45/90], for a total eight layers. The first seven layers were wet wound on the styrofoam mandrel. The eighth layer was dry wound in order to enhance the connection between the tubes after epoxy infusion process. The 90 degree layers were full layers that had the thickness of 0.5 mm and 42.6% fiber volume fraction; the ±45

degree and ±10 degree layers were half layers that had the thickness of 0.5 mm and 28% fiber volume fraction.

The top and bottom plates were manufactured by hand lay-up method. For deck F7-2, each plate had 42 layers of unidirectional glass fiber mats fabricated in a sequence of $[90/(\pm 45/\pm 10/\pm 10)_3/45/\pm 10/-45/(\pm 10/\pm 10/\pm 45)_3/90]$.

The purpose of the rounded corner design of equilateral-triangular tubes was to avoid stress concentration initiated by the filament winding process. The inside radius of the rounded corners was 20 mm, which created large voids at the top and bottom of the deck. Pultruded GFRP bars were used to fill the voids and also provide some stiffness to the deck. In order to improve the mechanical interaction and prevent bar slippage, 3 mm wide by 3 mm deep grooves were cut out every 25 mm along the length of the filler bars.

The detailed manufacturing procedures of the second-generation GFRP bridge deck can be found in Williams (2000a).

3.3 Third-generation GFRP Bridge Deck

There was only one specimen of the third-generation GFRP bridge deck, designated as F9-1 (Crocker et al., 2002). Figure 3.2 shows the cross-section of deck F9-1, and also some of the main dimensions.

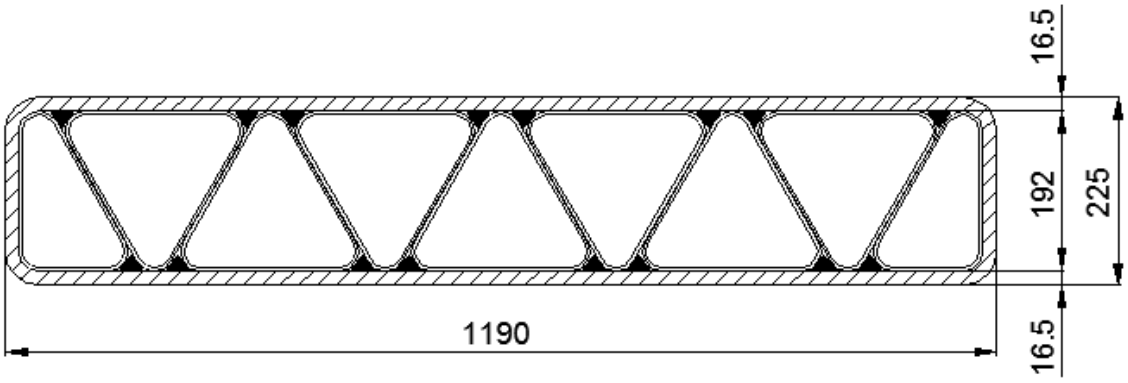

Figure 3.2: Cross-section of filament-wound GFRP bridge deck F9-1 (Unit: mm)

Deck F9-1 consisted of nine filament-wound triangular tubes, a filament-wound outside shell, and sixteen pultruded GFRP bars. Seven inside tubes had an equilateral-triangular shaped cross-section; the other two inside tubes had a right-angled triangular shaped cross-section. All nine inside tubes had exactly the same design parameters as the inside tubes of deck F7-2; for example, number of layers, stacking sequence, the thickness of each layer, and fiber volume fraction of each layer.

In order to enhance the structural integrity and performance of deck F9-1, the entire cross-section was filament wound with a 24-layer outside shell in a sequence of [90/±45/±10/±10/±45/±10/±10/±10/±45/±10/±10/±45/90].

Grooved, pultruded GFRP bars were placed in the voids that were generated by the rounded corner design of the inside tubes.

The detailed manufacturing procedures of the third-generation GFRP bridge deck can be found in Crocker et al. (2002).

3.4 Fourth-generation GFRP Bridge Deck

The fourth-generation GFRP bridge deck was designed to contain the optimum amount of fibers, so it is the most economical deck among all four generations. Only one specimen of the fourth-generation deck was manufactured, which was designated as F10-1. Figure 3.3 shows the cross-section of deck F10-1, and also some of the main dimensions.

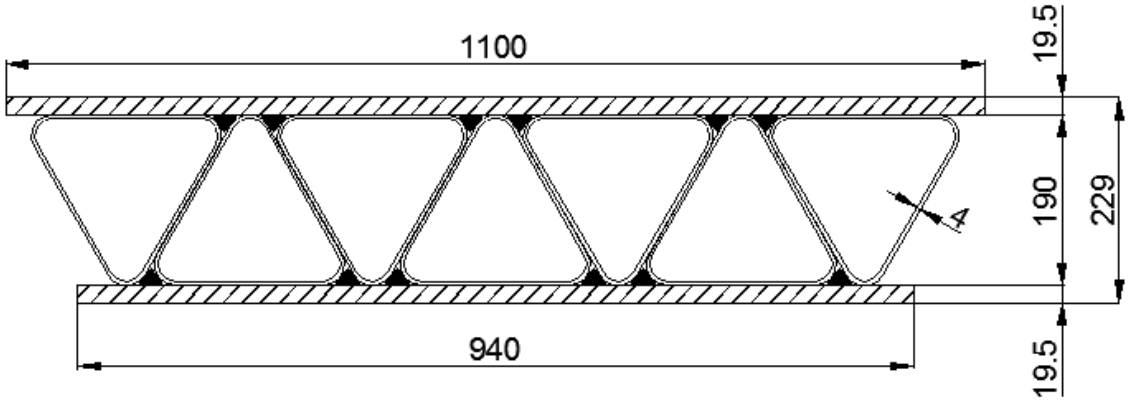

Figure 3.3: Cross-section of filament-wound GFRP bridge deck F10-1 (Unit: mm)

Deck F10-1 consisted of seven filament-wound equilateral-triangular tubes, two laminated, pultruded plates, and twelve pultruded GFRP bars. All seven inside tubes had the same design parameters as the inside tubes of deck F7-2 and deck F9-1.

Five 3.175 mm thick pultruded laminates were bonded together in a [0/90/0/90/0] sequence to form the top and bottom plates.

Grooved, pultruded GFRP bars were also used to fill the voids generated by the rounded corner design of the inside tubes.

The detailed manufacturing procedures of the fourth-generation GFRP bridge deck can be found in Crocker et al. (2002).

3.5 Material Properties

The material properties of the epoxy resin and glass fibers used for filament winding all four generations of GFRP bridge decks are provided in Table 3.1 and Table 3.2, respectively.

Table 3.1: Material properties of the epoxy resin

Property	**Value**
Density (kg/m^3)	1,160
Tensile Modulus (GPa)	3.15
Shear Modulus (GPa)	1.245
Tensile Strength (MPa)	64.8
Compressive Strength (MPa)	200
Shear Strength (MPa)	41
Poisson's Ratio	0.27
Heat Deflection Temperature (°C)	103

Table 3.2: Material properties of the glass fibers

Property	**Value**
Density (kg/m^3)	2,630
Tensile Modulus (GPa)	72.4
Shear Modulus (GPa)	29.431
Tensile Strength (MPa)	3450
Poisson's Ratio	0.22
Thermal Expansion (10^{-6}/°C)	5.8

In order to determine the modulus of elasticity of the pultruded GFRP bars, a tensile test was conducted by Brea Williams in the McQuade Structural Laboratory, The University of Manitoba. Figure 3.4 shows the stress-strain curve of the tested GFRP filler bar. The GFRP bar behaved linearly up to the stress level of 152.3 MPa, at which point the test program was stopped. The least-squares line method was used to obtain the modulus of elasticity of the filler bar (50,516 MPa).

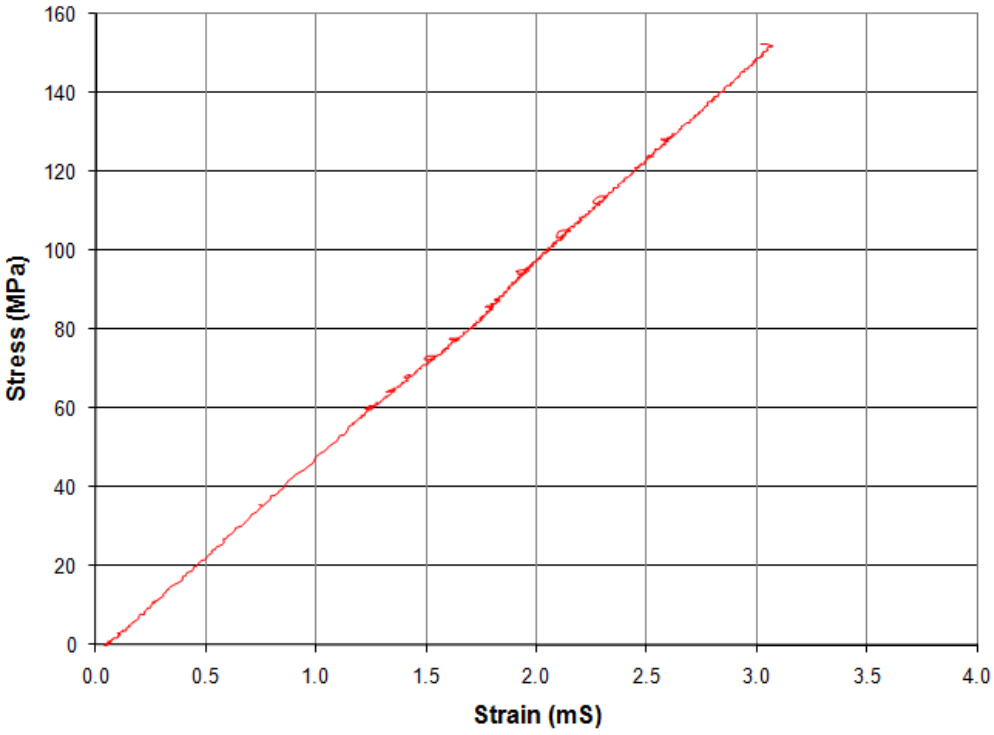

Figure 3.4: Stress-strain relationship of the pultruded GFRP filler bars

3.6 Test Setup

The experimental tests of the second-generation, third-generation and fourth-generation GFRP bridge decks were conducted at the McQuade Structural Laboratory, The University of Manitoba. As shown in Figure 3.5, all the deck specimens were 3.5 m long

and simply supported on roller supports with a span length of 3 m. A single point load was applied at the center of the specimen using a closed-loop MTS machine. A 570 mm × 225 mm loading plate was specifically chosen to simulate the tire contact area of an HS-30 design truck. Figure 3.6, Figure 3.7 and Figure 3.8 show the actual test setups of the second-generation, third-generation and fourth-generation GFRP bridge decks, respectively.

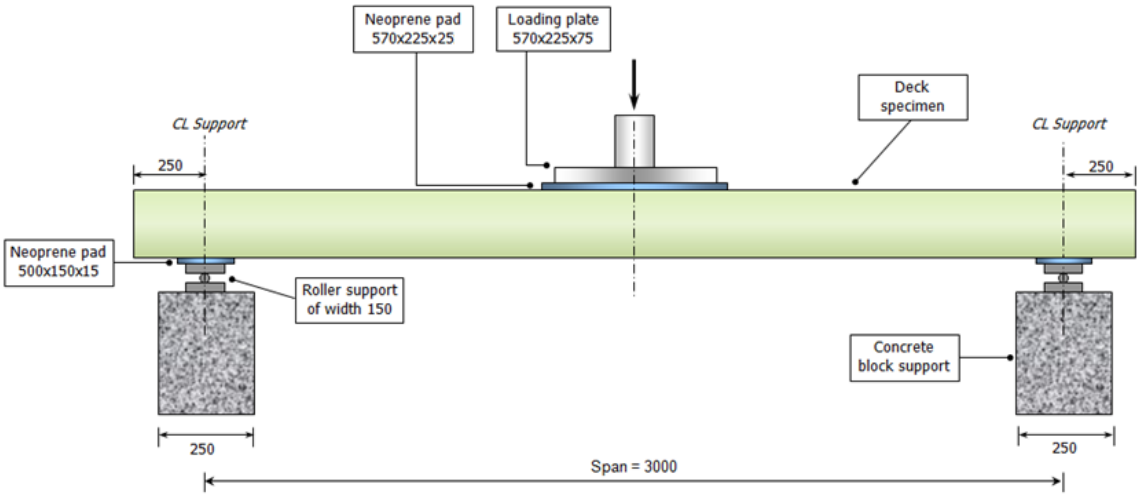

Figure 3.5: Schematic of three-point bending test setup (Unit: mm)

Figure 3.6: Test setup of the second-generation GFRP bridge deck (Williams, 2000b)

Figure 3.7: Test setup of the third-generation GFRP bridge deck (Crocker, 2000)

Figure 3.8: Test setup of the fourth-generation GFRP bridge deck (Crocker, 2001)

Electrical resistance strain gauges and LVDTs were employed to monitor the structural behaviors of these three filament-wound GFRP bridge decks during the flexural tests. The detailed instrumentation layouts of the second-generation, third-generation and fourth-generation GFRP bridge decks are presented in Appendix A, Appendix B and Appendix C, respectively.

3.7 Load Deflection Relationship and Mode of Failure

3.7.1 The second-generation GFRP bridge deck

Static testing was performed on the second-generation GFRP bridge deck. The load deflection curve of deck F7-2 is plotted in Figure 3.9. Note that the load is plotted versus the LVDT 2 located nearest to the loading area, as shown in Figure A.2 of Appendix A.

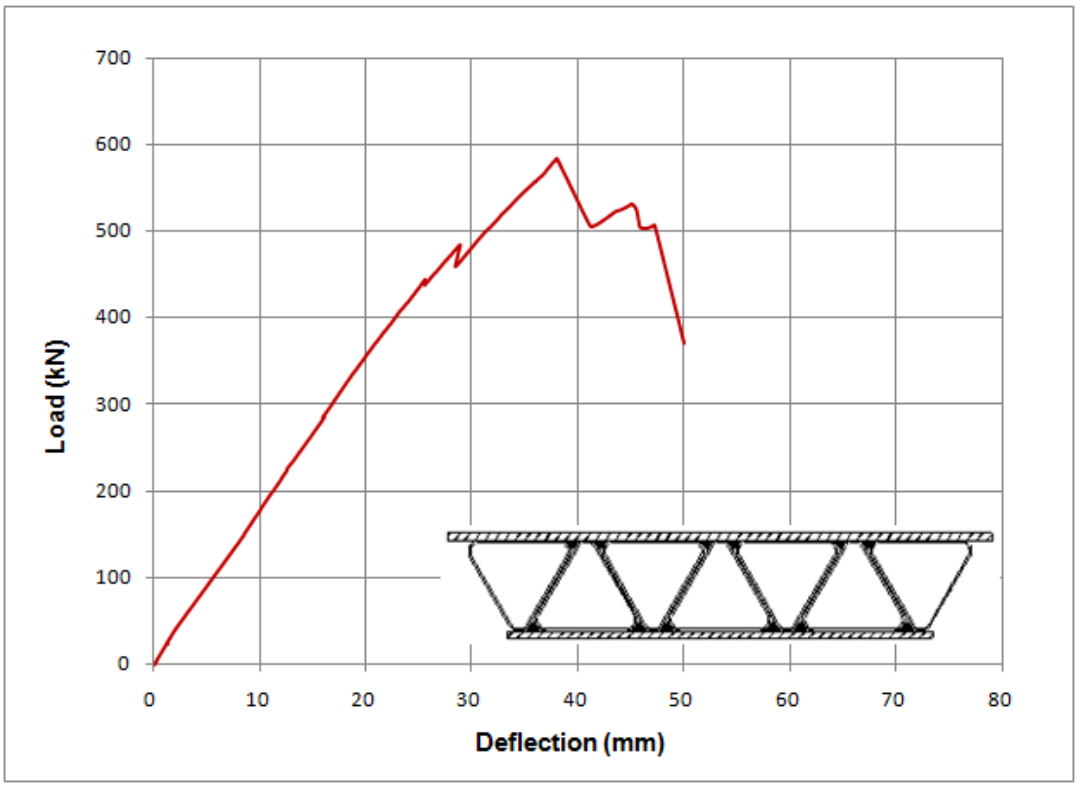

Figure 3.9: Load deflection relationship of deck F7-2 (Williams, 2000b)

Deck F7-2 displayed linear behavior up to 445 kN, at which point delamination cracking happened. Rapid delamination propagation resulted in the loss of stiffness, and led to structural failure at 584 kN. After that, the load dropped to 500 kN and then started climbing again. The final failure took place when one of the triangular inside tubes at the

west end of the deck slipped (Figure 3.10). Careful observation revealed that it was the bond between the inner wet-wound and the outer dry-wound layers that failed, and the outer dry-wound layers of adjacent triangular tubes remained intact.

Figure 3.10: Slippage of a triangular inside tube (adapted from Williams, 2000b)

Williams (2000a) verified that deck F7-2 satisfied the limiting deflection of L/360 at the service load of 139 kN, and that deck F7-2 exhibited strains well below the limiting strain level recommended to avoid creep rupture.

3.7.2 The third-generation GFRP bridge deck

The third-generation GFRP bridge deck was tested under cyclic loading varying between 10% and 135% of the HS-30 wheel load (139 kN at the service load level) for two million cycles with a frequency of 0.9 Hz. Static tests up to 135% of the service load

were performed at 0 cycles, 1,000 cycles, 10,000 cycles, 100,000 cycles, 250,000 cycles, 500,000 cycles, 750,000 cycles, 1 million cycles, 1.2 million cycles, 1.5 million cycles, 1.75 million cycles and 2 million cycles to investigate loss in stiffness. Figure 3.11 shows the calculated bending stiffness EI at various cycles. All the calculated bending stiffnesses were in the range of 1.27E7±0.10E7 $N \cdot m^2$. There were no signs of bending stiffness loss, and the small differences of the EI values were due to the deviation of the laboratory testing. It was concluded that no damage was caused to the deck F9-1 during the two-million load cycle test.

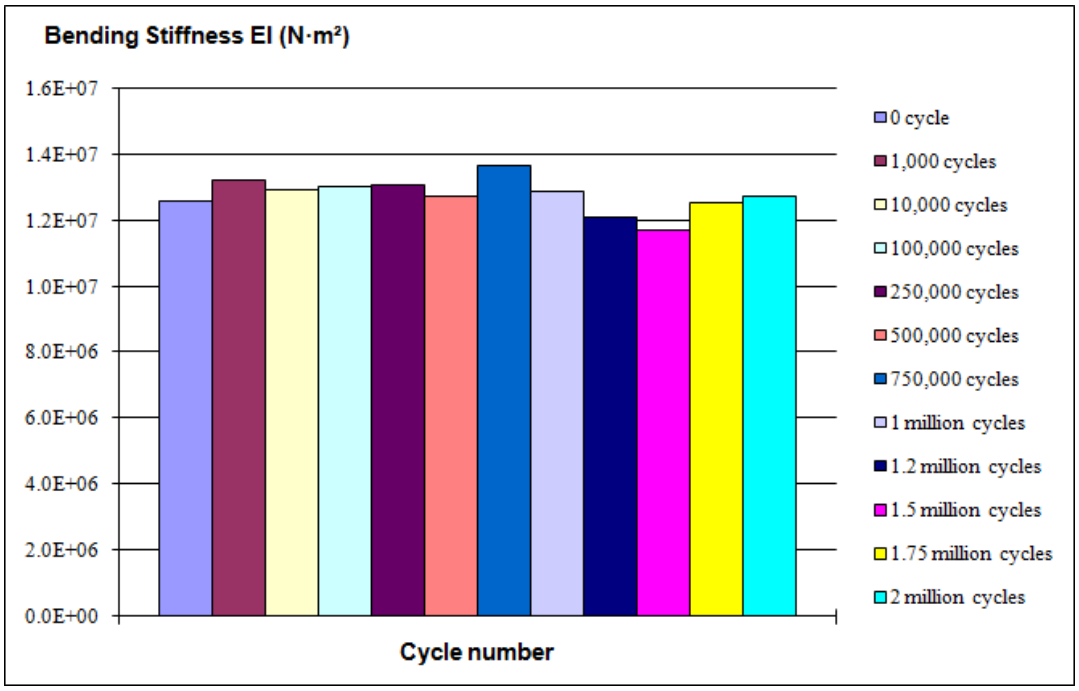

Figure 3.11: Calculated bending stiffness EI at various cycles

Static testing was then performed on deck F9-1 to determine its ultimate capacity. Figure 3.12 shows the load deflection curve of deck F9-1. The load is plotted versus the LVDT 2 located nearest to the loading area, as shown in Figure B.2 of Appendix B.

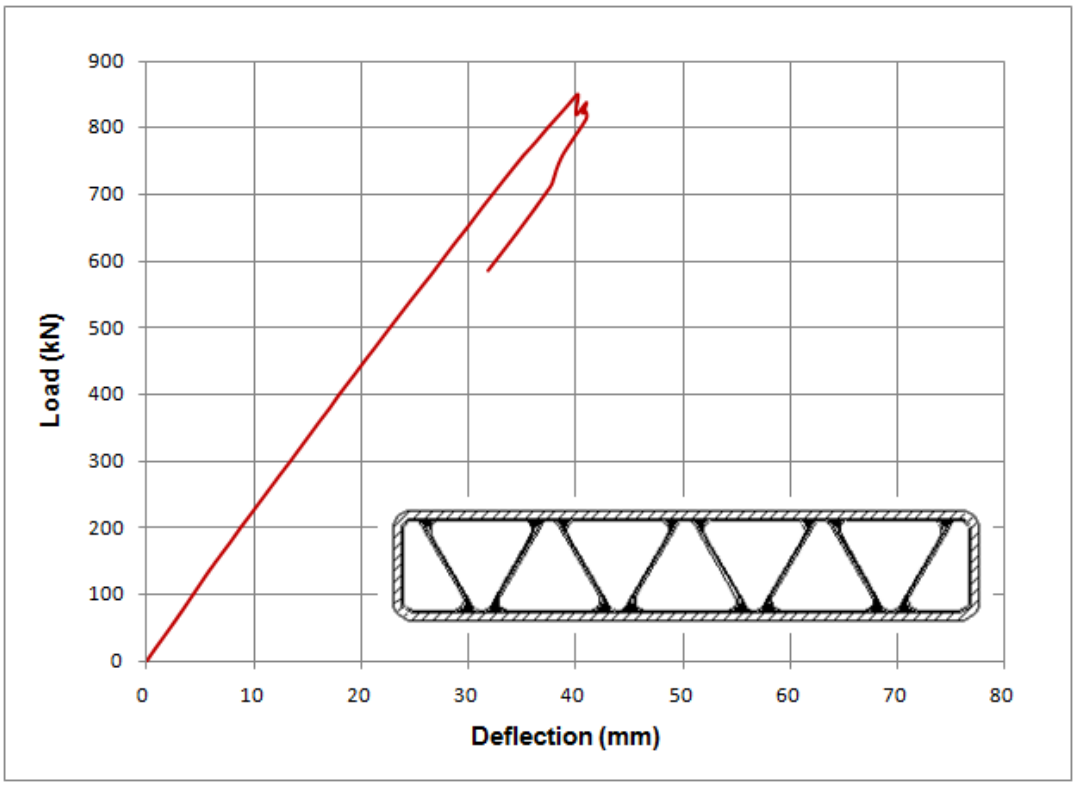

Figure 3.12: Load deflection relationship of deck F9-1 (Crocker, 2000)

Deck F9-1 was loaded to 466 kN, at which point a cracking sound was heard. This damage was very localized; therefore, the whole deck still behaved in a linear manner up to failure at 847 kN. The final failure mode was delamination buckling between two of the middle triangular tubes, as shown in Figure 3.13.

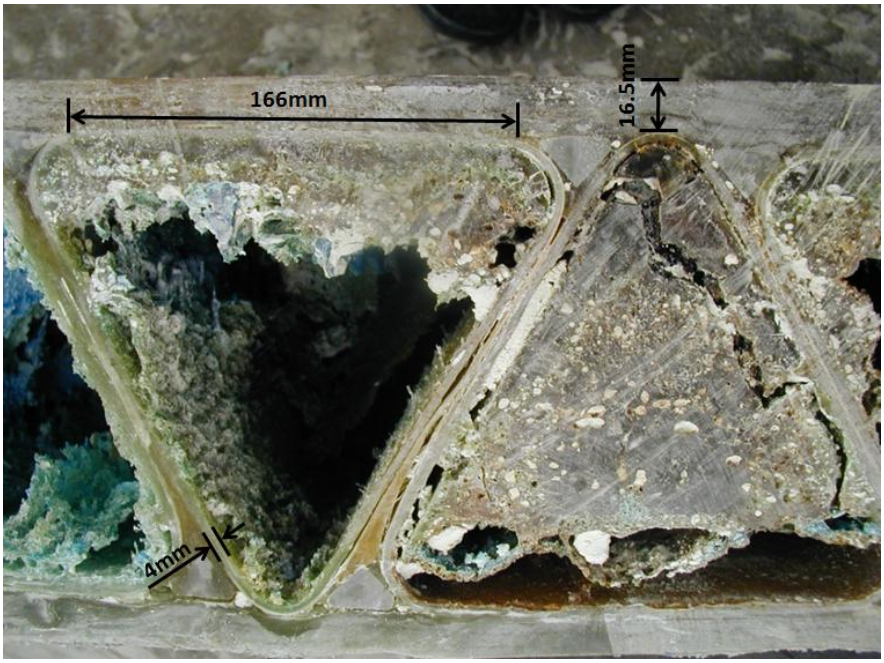

Figure 3.13: Delamination buckling failure of deck F9-1 (adapted from Crocker, 2000)

3.7.3 The fourth-generation GFRP bridge deck

Static testing was performed on the fourth-generation GFRP bridge deck. Figure 3.14 shows the load deflection curve of deck F10-1. Note that the load is plotted versus the LVDT 2 located closest to the loading area, as shown in Figure C.2 of Appendix C.

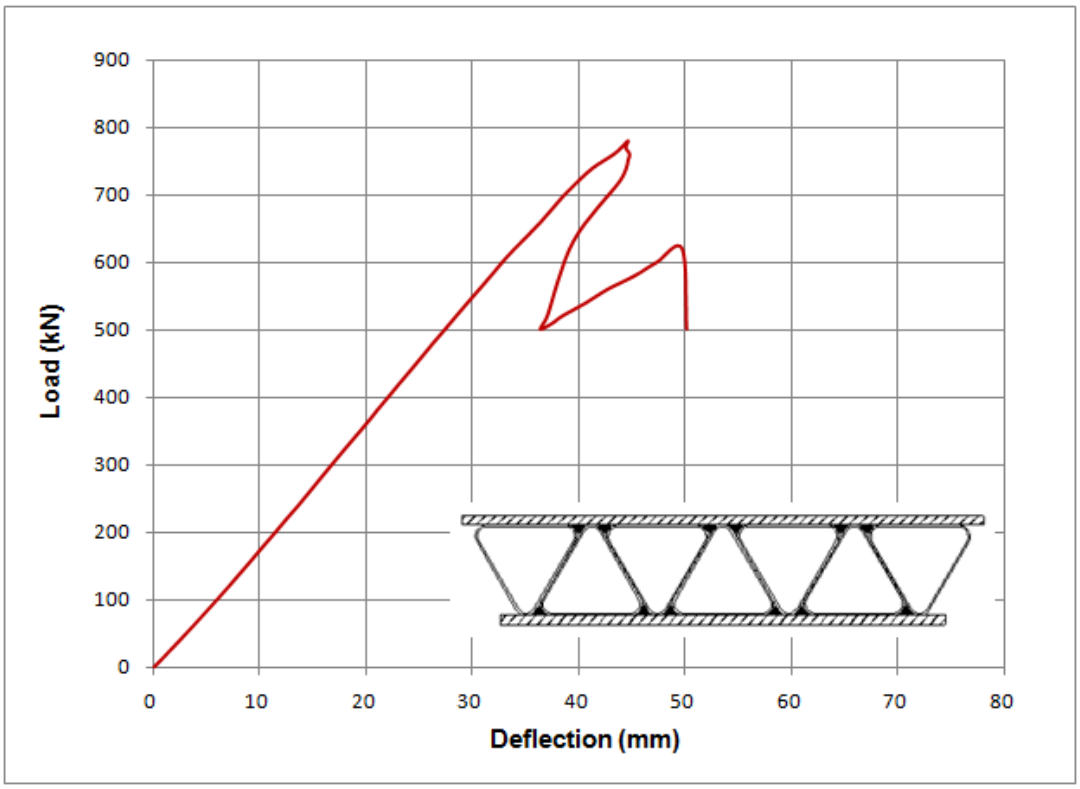

Figure 3.14: Load deflection relationship of deck F10-1 (Crocker, 2001)

Deck F10-1 behaved linearly up to failure at 780 kN. Failure was due to delamination buckling that lead to punching around the loading plate (Figure 3.15). Similar to deck F9-1, localized damage did not cause any apparent loss of stiffness before punching failure. Loading was continued until a large load drop at 620 kN when the top plate buckled, as shown in Figure 3.16.

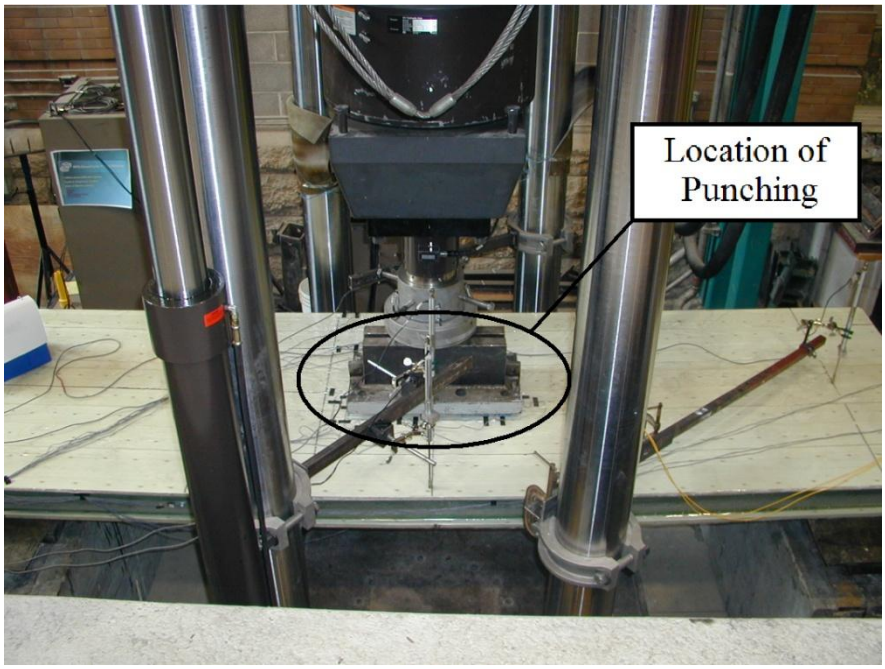

Figure 3.15: Punching failure of deck F10-1 (Crocker, 2001)

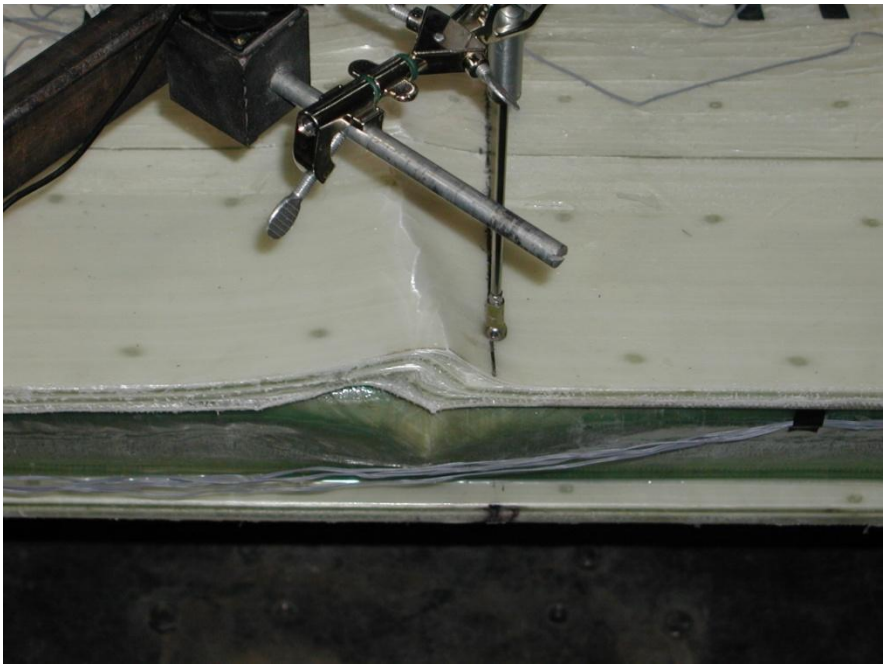

Figure 3.16: The top plate buckling of deck F10-1 (Crocker, 2001)

Chapter 4

Validation Study of a Finite Element Method against Experimental Results

4.1 General

A systematic method for analysis of FRP bridge decks using ANSYS finite element software is proposed in this chapter. This finite element method consists of two different finite element models: linear analysis model and delamination analysis model. Each finite element model has its own functioning area as described in the following sections. Combining these two analysis models can give bridge engineers a better understanding of the structural behavior of FRP bridge decks. Therefore, this proposed finite element method is labeled the "L&D" method. A validation study of the L&D method is conducted based on the experimental results of the second-generation, third-generation and fourth-generation GFRP bridge decks.

4.2 Linear Analysis Model

The functions of the linear analysis model are to predict the load/deflection ratio, to calculate the first-ply failure load, to estimate the deflections and strains, and to determine the eigenvalue buckling load of a FRP bridge deck.

4.2.1 Building the Linear Analysis Model

Two different types of elements were used to build the linear analysis model: SHELL99 and LINK8.

SHELL99 is an eight-node, linear layered structural shell element with six degrees of freedom at each node: translations in the nodal x, y and z directions and rotations about the nodal x, y and z axes (ANSYS, Inc., 2007a). Figure 4.1 shows the geometry, node locations, and the coordinate system of this element. SHELL99 is capable of modeling a composite laminate up to 250 uniform-thickness layers. A node offset option of this element allows nodes to be located at mid-surface, bottom surface or top surface. In the linear analysis model, the SHELL99 element was employed to model the equilateral-triangular inside tubes, the top and bottom plates of the second-generation and fourth-generation GFRP decks, and the outside shell of the third-generation GFRP deck.

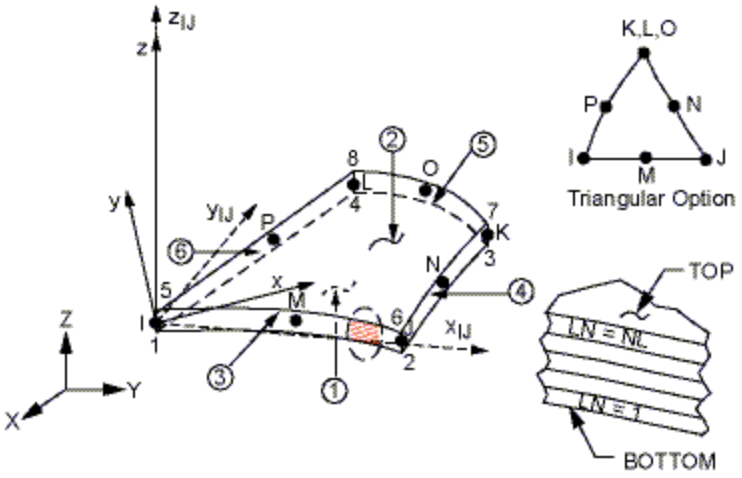

x_{IJ} = Element x-axis if ESYS is not supplied.

x = Element x-axis if ESYS is supplied.

LN = Layer Number

NL = Total Number of Layers

Figure 4.1: SHELL99 geometry (ANSYS, Inc., 2007a)

LINK8 is a 3-D spar element with three degrees of freedom at each node: translations in the nodal x, y and z directions (ANSYS, Inc., 2007a). Figure 4.2 shows the geometry, node locations, and the coordinate system of this element. LINK8 is only subject to uniaxial tension or compression (no bending considered). In the linear analysis model, LINK8 was employed to model the pultruded GFRP filler bars.

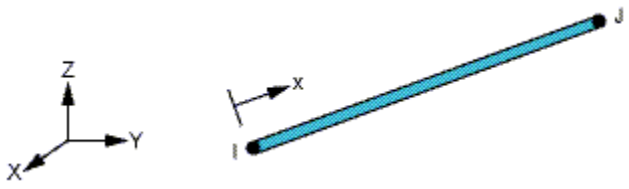

Figure 4.2: LINK8 geometry (ANSYS, Inc., 2007a)

The most important characteristic of a composite laminate structure is its layered configuration. Each layered shell element acquires its layer configuration through specifying individual layer properties, including orthotropic material properties, layer orientation angle, and layer thickness. If the fiber volume fraction of each layer and the material properties of the epoxy resin and glass fibers are known, the orthotropic material properties of individual layers can be easily calculated using the following equations derived from Classical Lamination Theory (CLT) (Mallick, 1993):

$$E_{11} = V_f E_f + V_m E_m \tag{4.1}$$

$$E_{22} = \frac{E_f E_m}{V_f E_m + V_m E_f} \tag{4.2}$$

$$E_{33} = E_{22} \tag{4.3}$$

$$G_{12} = \frac{G_f G_m}{V_f G_m + V_m G_f} \tag{4.4}$$

$$G_{23} = G_m \frac{V_f + \eta_{23}(1 - V_f)}{\eta_{23}(1 - V_f) + V_f G_m / G_f} \tag{4.5}$$

$$G_{13} = G_{12} \tag{4.6}$$

$$\upsilon_{12} = V_f \upsilon_f + V_m \upsilon_m \tag{4.7}$$

Where:

E_{11} = longitudinal Young's modulus of the lamina

E_{22} = transverse Young's modulus of the lamina

E_{33} = out-of-plane Young's modulus of the lamina

E_f = Young's modulus of fibers

E_m = Young's modulus of matrix

G_{12} = in-plane shear modulus of the lamina

G_{23} = out-of-plane shear modulus of the lamina (in 2-3 plane)

G_{13} = out-of-plane shear modulus of the lamina (in 1-3 plane)

G_f = shear modulus of fibers

G_m = shear modulus of matrix

V_f = fiber volume fraction

V_m = matrix volume fraction

υ_{12} = major Poisson's ratio of the lamina

υ_f = Poisson's ratio of fibers

υ_m = Poisson's ratio of matrix

$\eta_{23} = \frac{3-4\upsilon_m+G_m/G_f}{4(1-\upsilon_m)}$

Layer orientation angle is the angle (in degrees) between X-axes of the layer coordinate system and the element coordinate system. For constant thickness layer, only the thickness at node I needs to be specified; otherwise, the thicknesses at all four corner nodes must be entered. Figure 4.3 and Figure 4.4 show the layered configurations of the outside shell of deck F9-1 and the inside tube of deck F10-1, respectively.

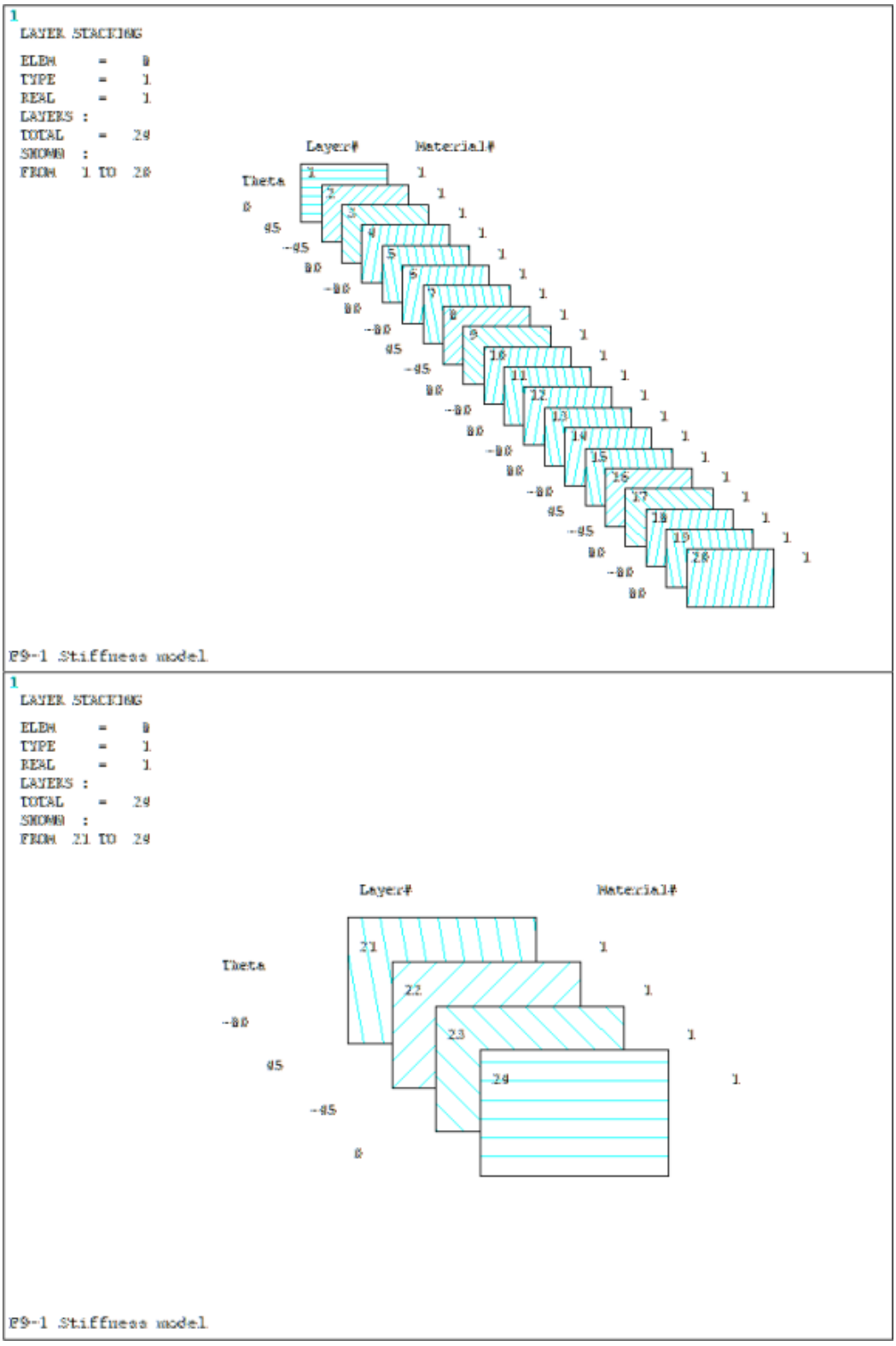

Figure 4.3: Layered configuration of the outside shell of deck F9-1

[90/±45/±10/±10/±45/±10/±10/±10/±45/±10/±10/±45/90]

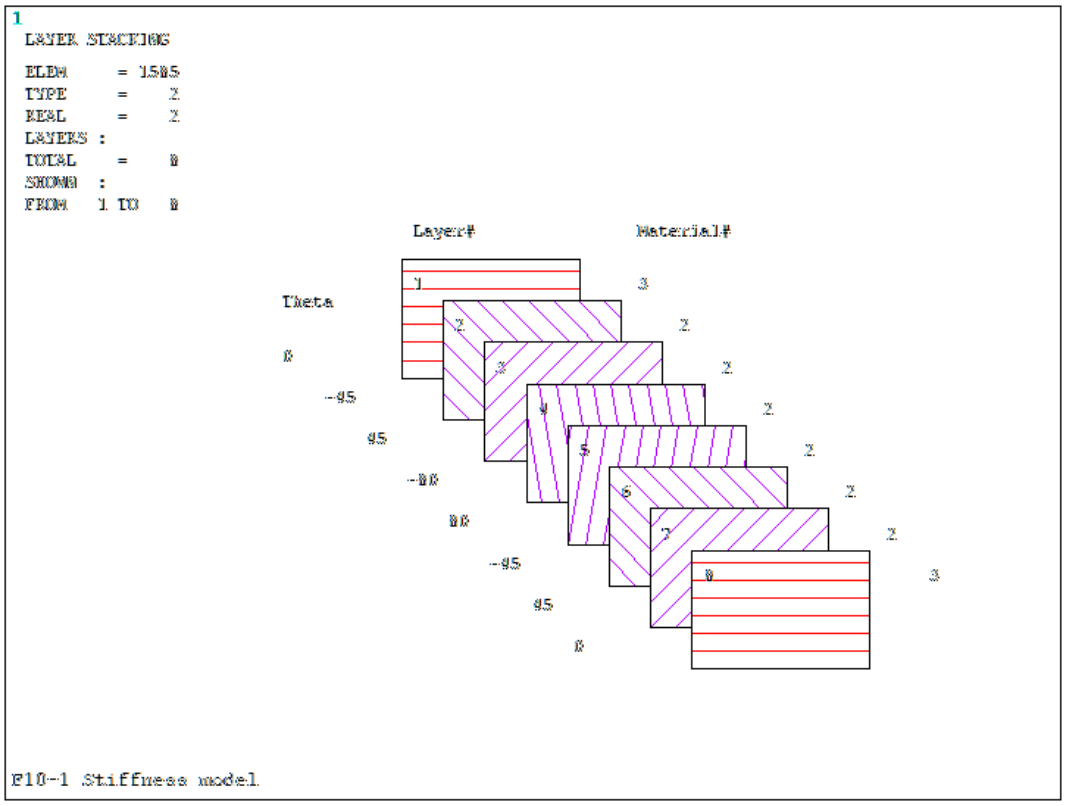

Figure 4.4: Layered configuration of the inside tube of deck F10-1

[90/±45/±10/±45/90]

Linear analysis models of all three generations of filament-wound GFRP bridge deck were built based on the dimensions of test specimens. Due to the symmetries of the specimen and the loading, only half of the model was created with appropriate boundary conditions. As shown in Figure 3.5, 25 mm thick neoprene pad was placed between the steel loading plate and the top surface of the bridge deck; therefore, the applied load was simulated as a uniformly distributed pressure over the loading area. It was assumed that all the bridge deck components were perfectly bonded and no delamination occurred during the loading process. Linear analysis models of deck F7-2, deck F9-1 and deck F10-1 are presented in Figure 4.5, Figure 4.6 and Figure 4.7, respectively. (Please refer to

Table 3.1 and Table 3.2 for the material properties of the epoxy resin and of the glass fibers.)

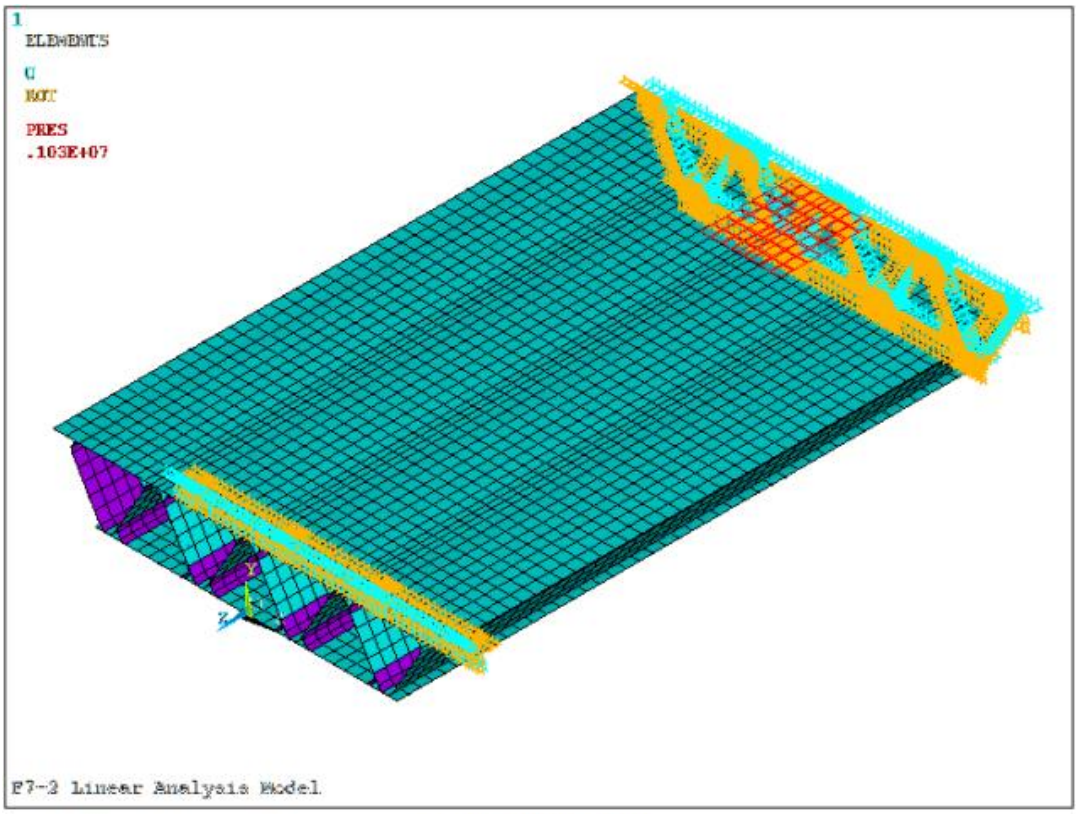

a. Isometric view

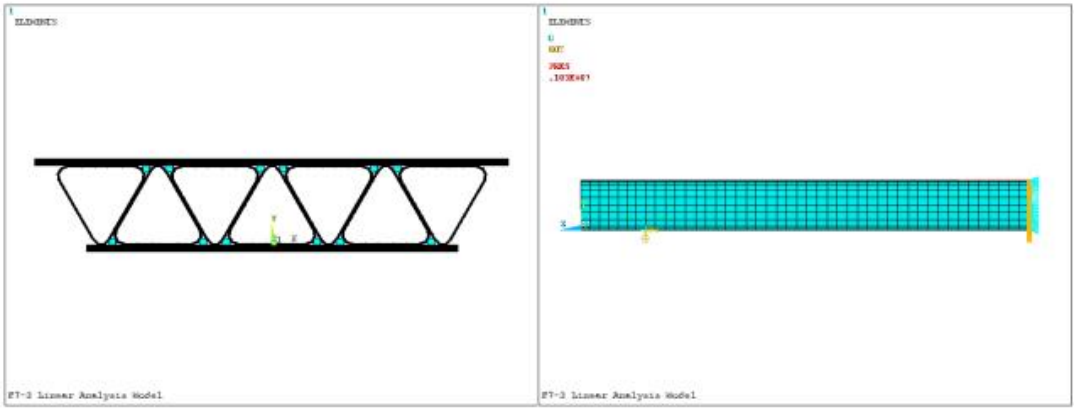

b. Front view

c. Right view

Figure 4.5: Linear analysis model of deck F7-2

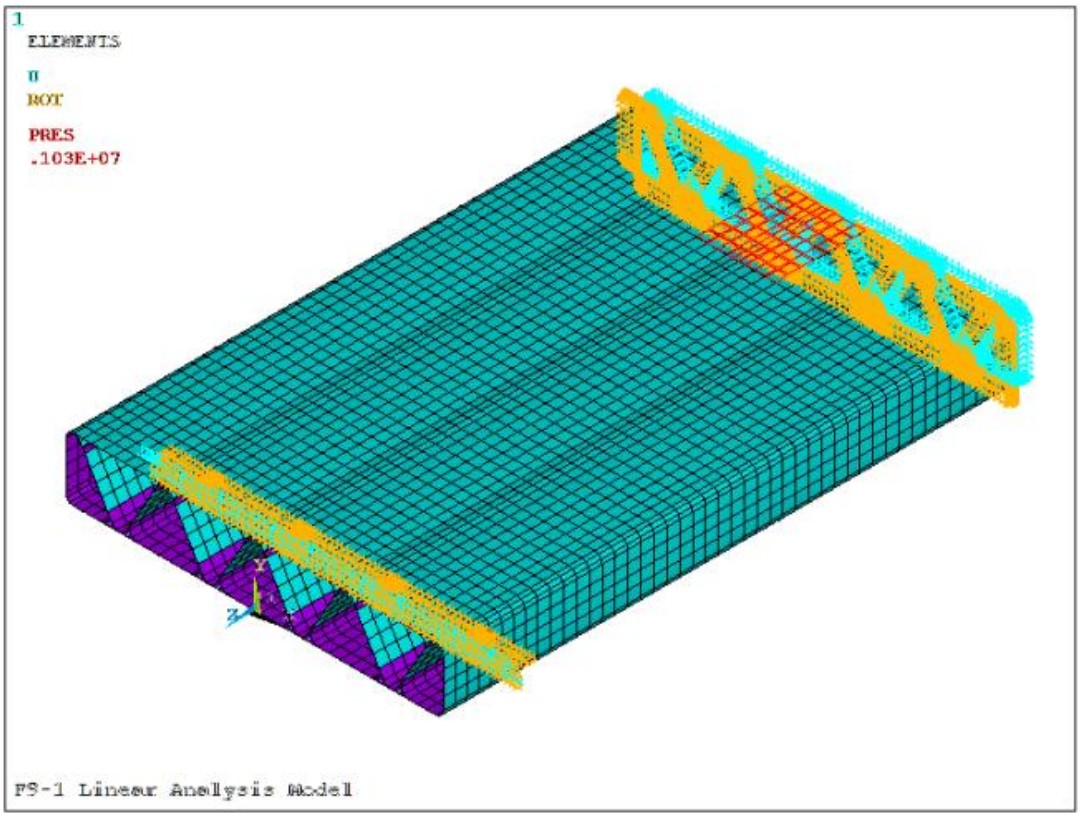

a. Isometric view

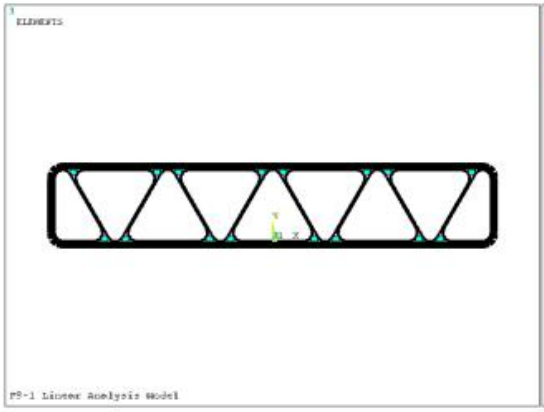

b. Front view

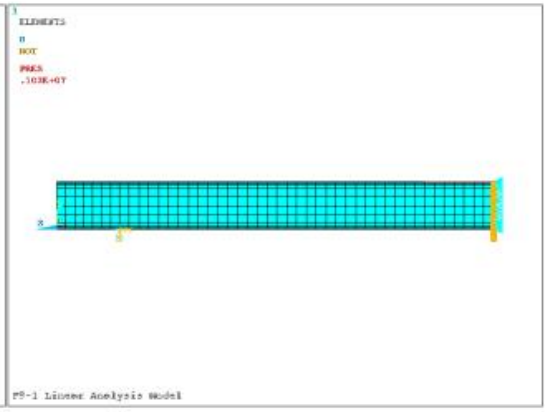

c. Right view

Figure 4.6: Linear analysis model of deck F9-1

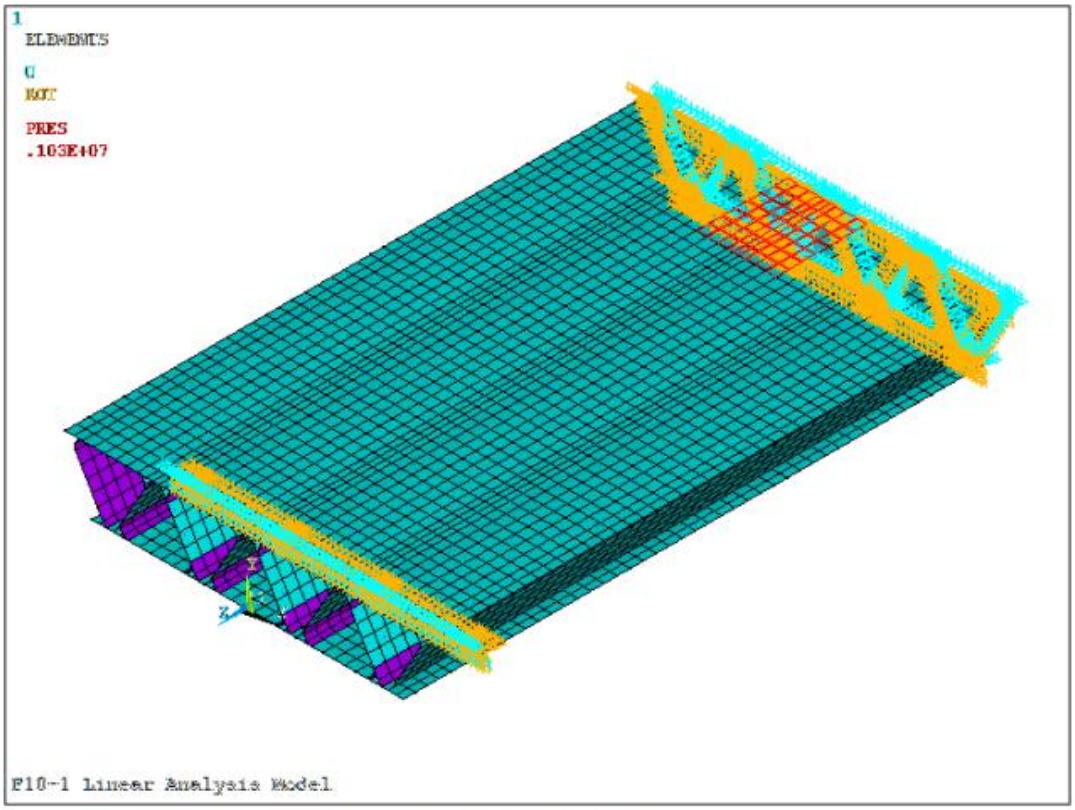

a. Isometric view

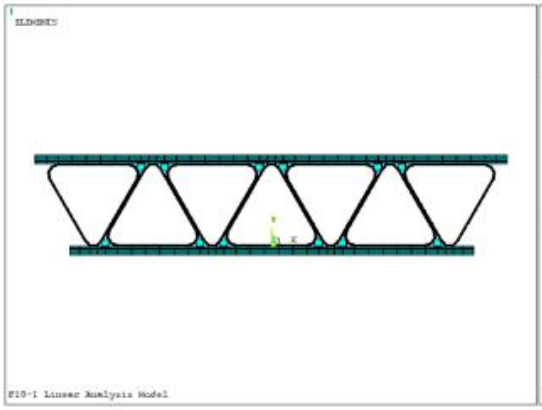

b. Front view

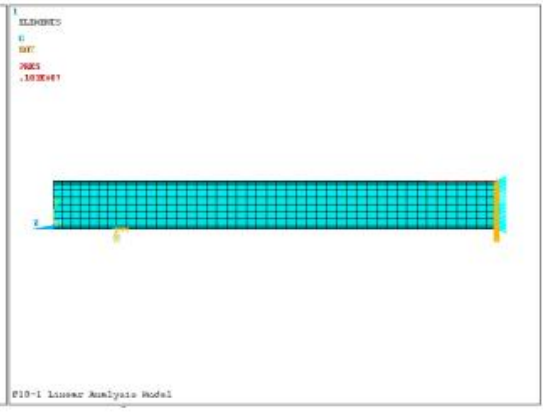

c. Right view

Figure 4.7: Linear analysis model of deck F10-1

4.2.2 Load/Deflection Ratio

Load/deflection ratio is a very important design parameter because of the relatively lower modulus of elasticity of FRP material. Good prediction of load/deflection ratio allows the FRP bridge deck designers to effectively design the deck for several applications with different parameters. An analysis spreadsheet based on CLT was developed by Williams (2000a) to estimate the load/deflection ratios of the FRP bridge decks. The Linear Analysis Model (LAM) proposed in this thesis could also calculate the load/deflection ratios.

For deck F7-2, the thickness tolerance of the top and bottom plates was ±1 mm, and the thickness tolerance of the triangular inside tubes was ±0.25 mm (private communication from Dr. Emile Shehata, Wardrop Engineering Inc.). With consideration of these manufacturing tolerances, the load deflection relationship predicted by CLT or LAM would consist of an upper limit curve and a lower limit curve. The load deflection relationships of deck F7-2 predicted by CLT (dash dotted lines) and LAM (dashed lines) are plotted against its experimental results in Figure 4.8.

For deck F9-1, the thickness tolerance of the outside shell was ±1 mm, and the thickness tolerance of the triangular inside tubes was ±0.25 mm. The load deflection relationships of deck F9-1 predicted by CLT (dash dotted lines) and LAM (dashed lines) are plotted against its experimental results in Figure 4.9. As shown in this figure, cyclic test results gave a range of load/deflection ratios due to the deviation of laboratory testing (Section 3.7.2), and the load/deflection ratio of the subsequent static test result fell in this range.

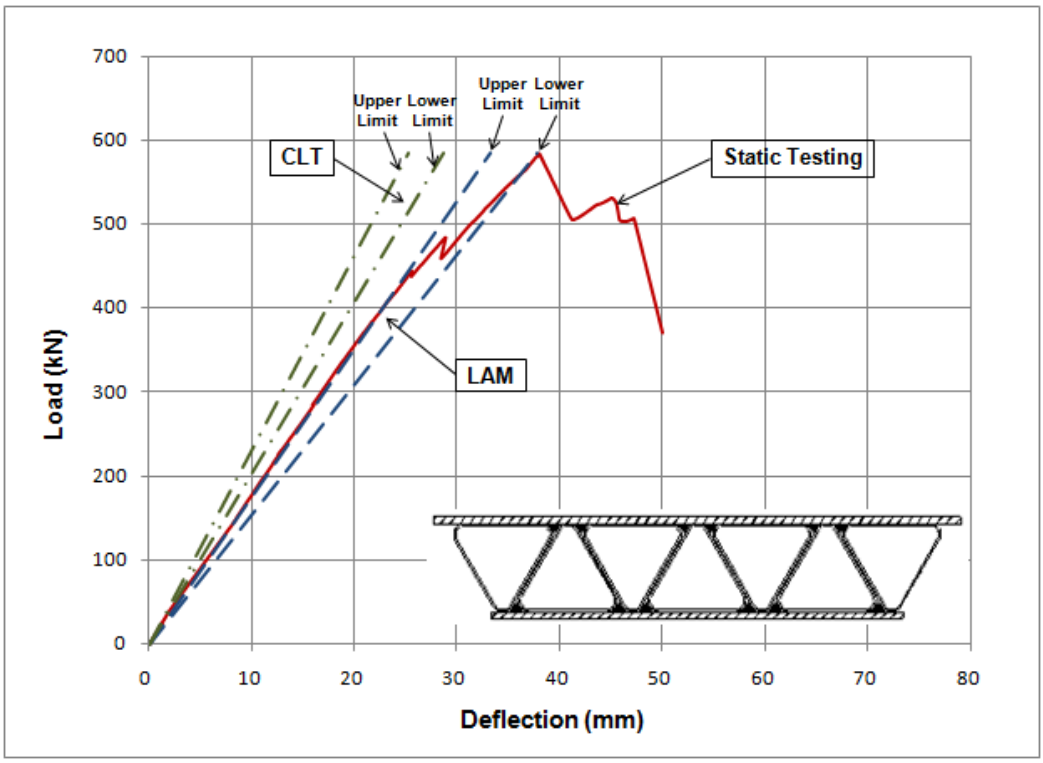

Figure 4.8: Predicted and experimental load deflection relationships of deck F7-2

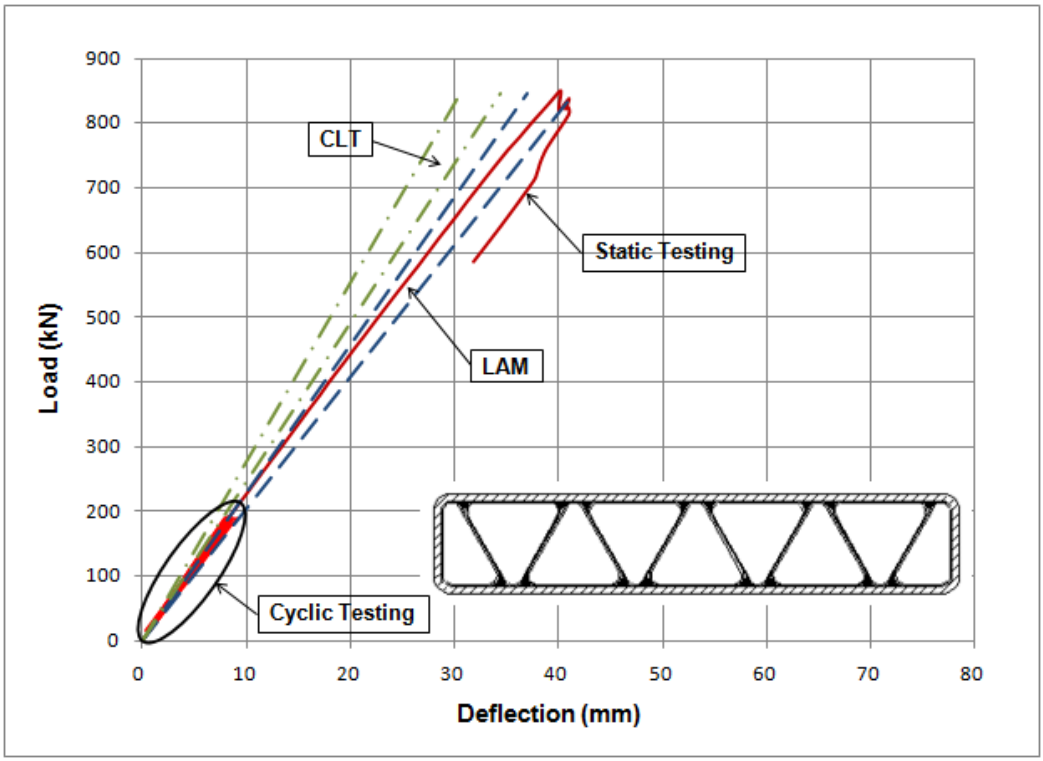

Figure 4.9: Predicted and experimental load deflection relationships of deck F9-1

For deck F10-1, the thickness tolerance of the top and bottom plates was ±1 mm, and the thickness tolerance of the triangular inside tubes was ±0.25 mm. The load deflection relationships of deck F10-1 predicted by CLT (dash dotted lines) and LAM (dashed lines) are plotted against its experimental results in Figure 4.10.

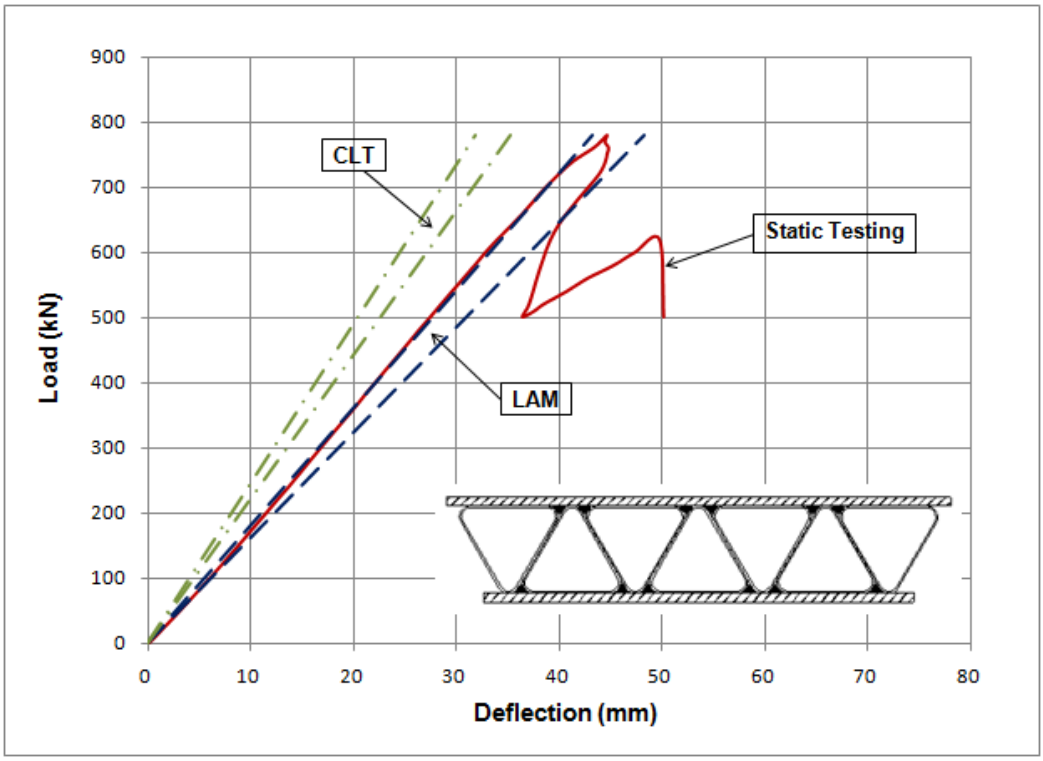

Figure 4.10: Predicted and experimental load deflection relationships of deck F10-1

As shown in Figure 4.8, Figure 4.9 and Figure 4.10, the predicted behavior is plotted up to the failure of the GFRP decks, but it should be applied only to the linear range of the relationship immediately before nonlinear behavior happens. Table 4.1 presents the percentage error between predicted and actual (static testing) load/deflection ratios within this linear range. Compared with CLT, the load/deflection ratios predicted by LAM are much closer to the static test results. The linear analysis model can predict the load/deflection ratio of a FRP bridge deck with a small percentage error.

Table 4.1: Percentage error between predicted and actual load/deflection ratios

Deck	Percentage Error of CLT	Percentage Error of LAM
F7-2	+19.0% ~ +34.5%	-9.7% ~ +2.5%
F9-1	+15.7% ~ +30.5%	-4.1% ~ +7.9%
F10-1	+20.6% ~ +33.7%	-11.8% ~ -1.4%

4.2.3 First-Ply Failure Load

The definition of first-ply failure (FPF) is that a laminate is considered to have failed when its first layer fails. The FPF approach is very conservative, because failure of a lamina does not necessarily imply the total failure of the laminate. However, the FPF signals the initiation of an interactive and progressive failure process. There are various FPF criteria for composite laminates; for example, maximum stress failure criterion, maximum strain failure criterion, Tsai-Hill failure criterion, and Tsai-Wu failure criterion. Table 4.2 summarizes some characteristics of these four failure criteria.

Table 4.2: Comparison of failure criteria (Daniel and Ishai, 1994)

Theory	Physical basis	Operational convenience	Required experimental characterization
Maximum stress	Tensile behavior of brittle material No stress interaction	Inconvenient	Few parameters by simple testing
Maximum strain	Tensile behavior of brittle material Some stress interaction	Inconvenient	Few parameters by simple testing
Deviatoric strain energy (Tsai-Hill)	Ductile behavior of anisotropic materials "Curve fitting" for heterogeneous brittle composites	Can be programmed Different functions required for tensile and compressive strengths	Biaxial testing is needed in addition to uniaxial testing
Interactive tensor polynomial (Tsai-Wu)	Mathematically consistent Reliable "curve fitting"	General and comprehensive Operationally simple	Numerous parameters Comprehensive experimental program needed

The Tsai-Wu failure theory satisfies the invariant requirements of coordinate transformation, abiding by normal tensor transformation laws (Daniel and Ishai, 1994). The strength tensors have similar symmetry properties as the stiffness tensors. If experimental data is available, the interaction terms can be considered as separate components. This failure theory takes into account the difference between tensile and compressive strengths through its linear terms. In addition, the Tsai-Wu failure criterion is operationally simple. Therefore, it was selected for the following FPF analysis.

Preliminary work before FPF analysis using the Tsai-Wu failure criterion is to calculate the strength of a single unidirectional lamina. The calculation of the longitudinal tensile strength of a unidirectional lamina depends on the relative magnitudes of the ultimate tensile strains of the fiber and matrix (Daniel and Ishai, 1994).

When $\varepsilon_{ft}^{u} < \varepsilon_{mt}^{u}$

$$S_{1T} = S_f \left(V_f + V_m \frac{E_m}{E_f} \right) \tag{4.8}$$

And when $\varepsilon_{mt}^{u} < \varepsilon_{ft}^{u}$

$$S_{1T} = S_{mT} \left(V_f \frac{E_f}{E_m} + V_m \right) \tag{4.9}$$

Where:

ε_{ft}^{u} = ultimate tensile strain of fibers

ε_{mt}^{u} = ultimate tensile strain of matrix

S_{1T} = longitudinal tensile strength of the lamina

S_f = fiber tensile strength

S_{mT} = matrix tensile strength

The longitudinal compressive strength of a unidirectional lamina is expressed as

$$S_{1C} = (2S_{m12})^{2/3}(E_{11})^{1/3} \tag{4.10}$$

Where:

S_{1C} = longitudinal compressive strength of the lamina

S_{m12} = matrix shear strength

The transverse tensile strength of a unidirectional lamina can be predicted by

$$S_{2T} = \frac{1-\upsilon_m}{k_\sigma(1+\upsilon_m)(1-2\upsilon_m)}(S_{mT} - \varepsilon_{rm} E_m) \tag{4.11}$$

Where:

S_{2T} = transverse tensile strength of the lamina

ε_{rm} = maximum residual radial strain

k_σ = stress concentration factor (Figure 4.11)

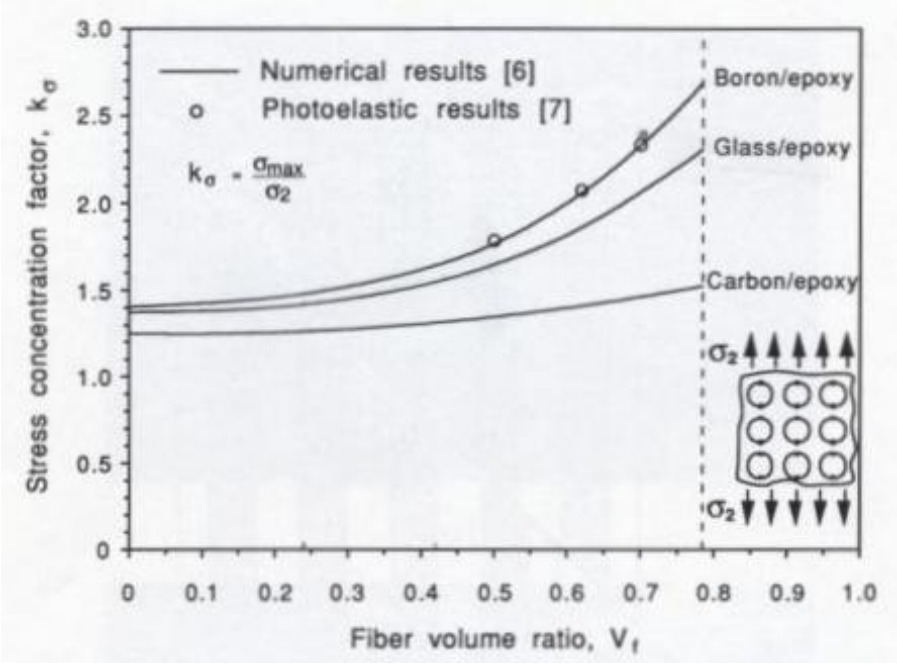

Figure 4.11: Stress concentration in matrix of unidirectional composites with square fiber array under transverse tension (Daniel and Ishai, 1994)

The transverse compressive strength of a unidirectional lamina is given by

$$S_{2C} = \frac{S_{mC} + \sigma_{rm}}{k_\sigma} \tag{4.12}$$

Where:

S_{2C} = transverse compressive strength of the lamina

S_{mC} = matrix compressive strength

σ_{rm} = maximum residual radial stress

The in-plane shear strength of a unidirectional lamina based on matrix shear failure is obtained as

$$S_{12} = \frac{S_{m12}}{k_\tau} \tag{4.13}$$

Where:

S_{12} = in-plane shear strength of the lamina

k_τ = shear stress concentration factor

The calculated strengths of a single unidirectional lamina are then substituted into the reduced form (2-D version) of Tsai-Wu failure criterion (Daniel and Ishai, 1994)

$$f_1\sigma_1 + f_2\sigma_2 + f_{11}\sigma_1^2 + f_{22}\sigma_2^2 + f_{66}\tau_{12}^2 + 2f_{12}\sigma_1\sigma_2 = 1 \tag{4.14}$$

Where:

$$f_1 = \frac{1}{S_{1T}} - \frac{1}{S_{1C}}$$

$$f_2 = \frac{1}{S_{2T}} - \frac{1}{S_{2C}}$$

$$f_{11} = \frac{1}{S_{1T}S_{1C}}$$

$$f_{22} = \frac{1}{S_{2T}S_{2C}}$$

$$f_{66} = \frac{1}{S_{12}^2}$$

$$f_{12} \cong -\frac{1}{2}(f_{11}f_{22})^{1/2}$$

σ_1 = longitudinal stress in the lamina

σ_2 = transverse stress in the lamina

τ_{12} = in-plane shear stress in the lamina

The safety factor ξ_f for the Tsai-Wu failure criterion is a multiplier, which is applied to all stress components to create a failure state. Substitution of the critical stresses in the Tsai-Wu failure criterion yields

$$f_1\xi_f\sigma_1 + f_2\xi_f\sigma_2 + f_{11}\xi_f^2\sigma_1^2 + f_{22}\xi_f^2\sigma_2^2 + f_{66}\xi_f^2\tau_{12}^2 + 2f_{12}\xi_f^2\sigma_1\sigma_2 = 1 \quad (4.15)$$

Where:

ξ_f = safety factor for the actual state of stress $(\sigma_1, \sigma_2, \tau_{12})$

The solutions of the quadratic equation (4.15) yield the safety factor ξ_f as

$$\xi_f = \frac{-(f_1\sigma_1+f_2\sigma_2)+\sqrt{(f_1\sigma_1+f_2\sigma_2)^2+4(f_{11}\sigma_1^2+f_{22}\sigma_2^2+f_{66}\tau_{12}^2+2f_{12}\sigma_1\sigma_2)}}{2(f_{11}\sigma_1^2+f_{22}\sigma_2^2+f_{66}\tau_{12}^2+2f_{12}\sigma_1\sigma_2)} \quad (4.16)$$

In ANSYS finite element software, a failure index for Tsai-Wu failure criterion, ξ_3, is defined as

$$\xi_3 = 1/\xi_f \quad (4.17)$$

Where:

ξ_3 = failure index of Tsai-Wu failure criterion

If the ξ_3 value of any lamina of any layered SHELL99 element within a FRP bridge deck model is larger than or equal to one, the FPF happens; otherwise, the FRP deck still behaves well without any lamina damage.

The FPF analysis based on Tsai-Wu failure criterion was conducted using the linear analysis model. The results showed that the FPFs of deck F7-2, deck F9-1 and deck F10-1 all happened at the middle span right beneath the loading plate. Figure 4.12 shows the FPF location of deck F7-2. For deck F7-2, it was the 39^{th} layer of the top plate element that failed; for deck F9-1, it was the 21^{st} layer of the outside shell element that failed; and for deck F10-1, it was the 9^{th} layer of the top plate element that failed. It was interesting that the fibers of these three failed layers were all oriented in a direction parallel to the deck span.

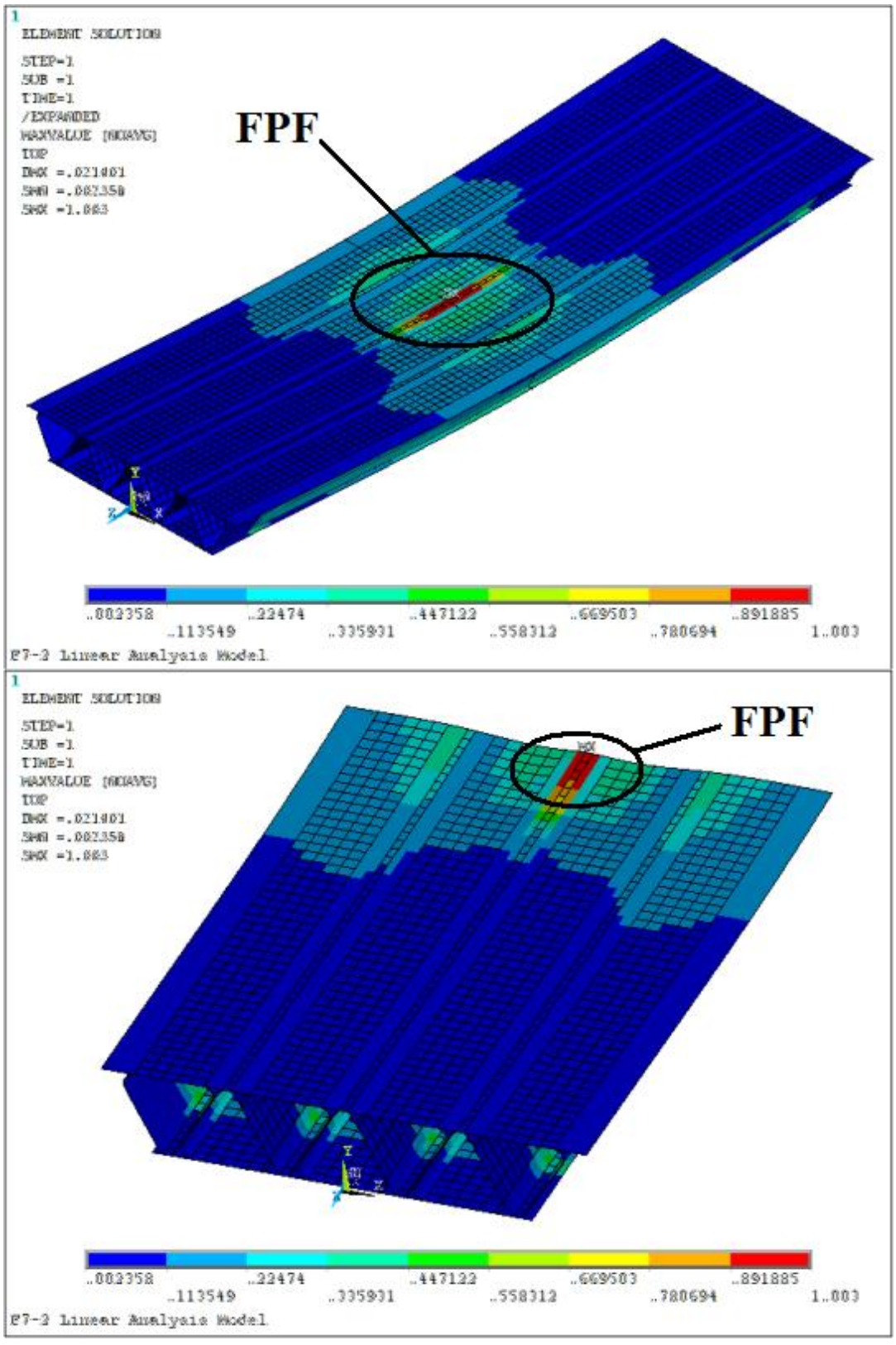

Figure 4.12: FPF location of deck F7-2

Table 4.3 presents the computed FPF loads of deck F7-2, deck F9-1 and deck F10-1. As shown in this table, the computed FPF loads of all three specimens are about 50 percent of their actual failure loads. Apparently, FPF does not mean the failure of the whole FRP bridge deck. The load deflection relationships of the specimens could still behave in a linear manner after exceeding the FPF loads, as shown in Figure 3.9, Figure 3.12 and Figure 3.14. Careful observation of these three figures shows that FPFs of deck F7-2, deck F9-1 and deck F10-1 did not lead to any noticeable changes in the measured load deflection relationships. However, it was recorded by Heather Crocker that a cracking sound was heard at 466 kN during the static test of deck F9-1, which was quite close to its FPF load of 451 kN. It is conceivable that FPF did occur at a relatively lower load and was not easy to detect because of its insignificant impact on the overall behavior.

Table 4.3: Computed FPF loads of deck F7-2, deck F9-1 and deck F10-1

Deck	**FPF Load (Tsai-Wu Criterion)**	**Percentage of Actual Failure Load**
F7-2	311 kN	53.3 %
F9-1	451 kN	53.2 %
F10-1	377 kN	48.3 %

It is extremely important to keep the service load below the FPF level in the design of FRP bridge decks. The significance of this conclusion can be verified by the cyclic testing of deck F9-1. Because the upper limit of the cyclic loading (188 kN) was much lower than the FPF load of deck F9-1 (451 kN), the deck survived two million load cycles without any stiffness loss.

It should be noted that FPF analysis, based on the linear analysis model, is easy to carry out and requires much less processing time than nonlinear analysis. It is recommended as an indicator of lower bound failure criterion for the design of FRP bridge decks.

4.2.4 Deflections and Strains

The linear analysis model can predict the deflections and strains of a FRP bridge deck at various load levels. The predicted results and instrumentation readings are plotted together at four different load levels (service load, FPF load, 3/4 of failure load and failure load) to validate the accuracy of the linear analysis results. The midspan deflections across deck width for the three specimens are shown in Figure 4.13 through Figure 4.15.

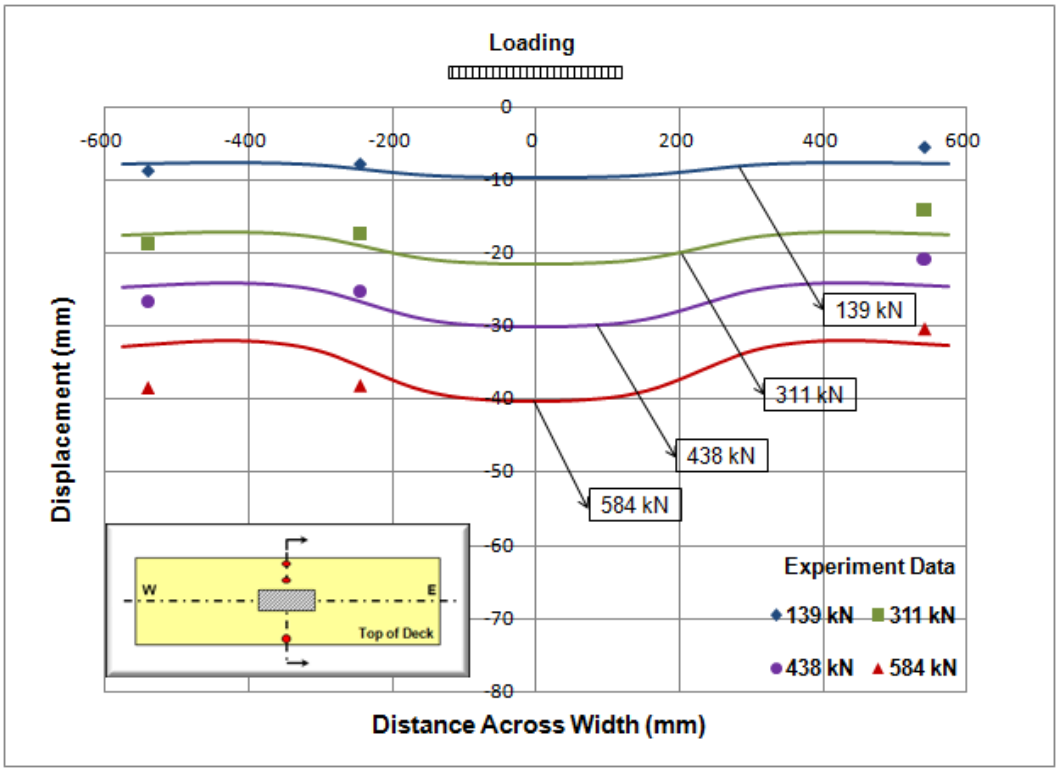

Figure 4.13: Midspan deflection across deck width (F7-2)

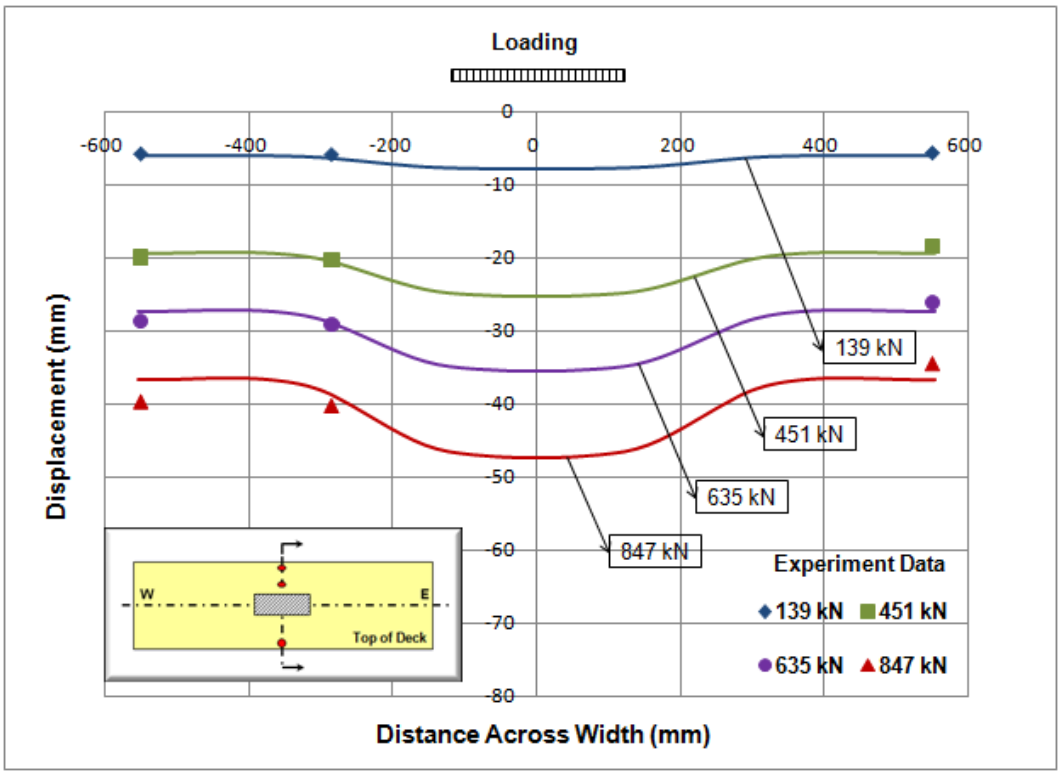

Figure 4.14: Midspan deflection across deck width (F9-1)

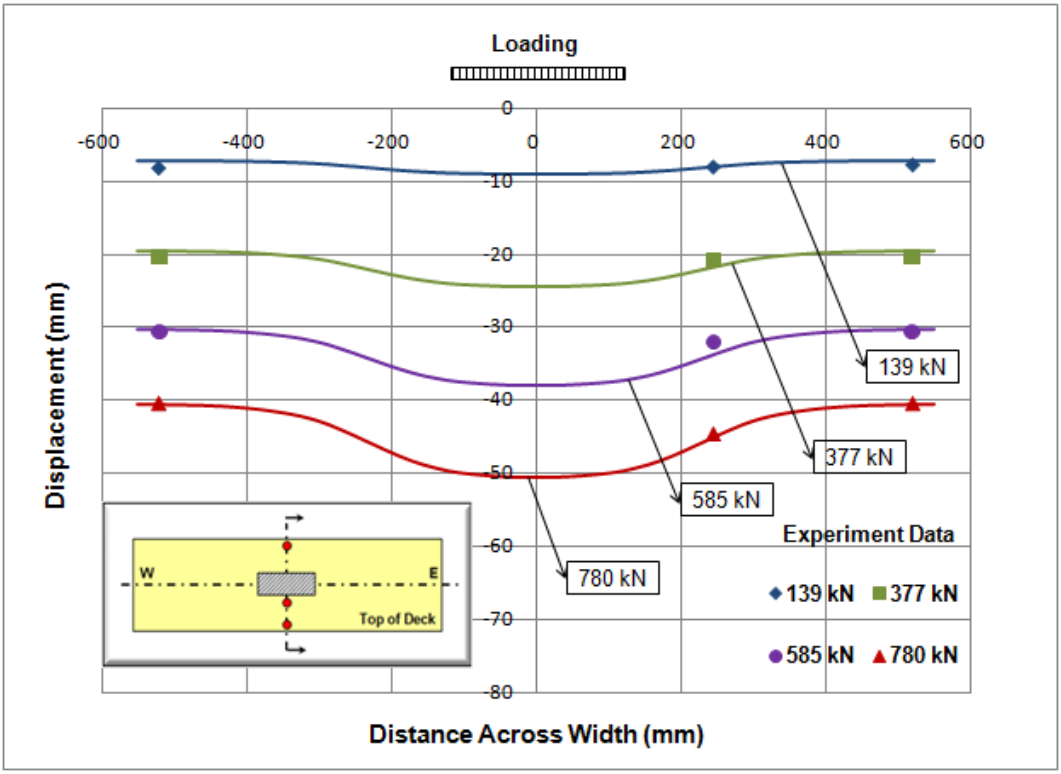

Figure 4.15: Midspan deflection across deck width (F10-1)

The data from strain gauges and fiber optic sensors of deck F10-1 were not published elsewhere (refer to Appendix C). Therefore, the following discussion about the strain distribution is limited to deck F7-2 and deck F9-1.

The axial strain distributions along deck span are shown in Figure 4.16 through Figure 4.23. The axial strain distributions across deck width are given in Figure 4.24 through Figure 4.35. The actual contact condition between the steel loading plate and the top plate of the deck was too difficult to define in the linear analysis model, and this contact problem was not the focus of this research. Moreover, due to the existence of the neoprene pad, the applied load was simulated as a uniformly distributed pressure over the loading area (refer to Section 4.2.1). However, this simplifying assumption resulted in an inaccurate strain prediction of that part of the top plate right under the loading plate. Therefore, the predicted strains within the loading area are not plotted in Figure 4.16, Figure 4.17, Figure 4.28 and Figure 4.29.

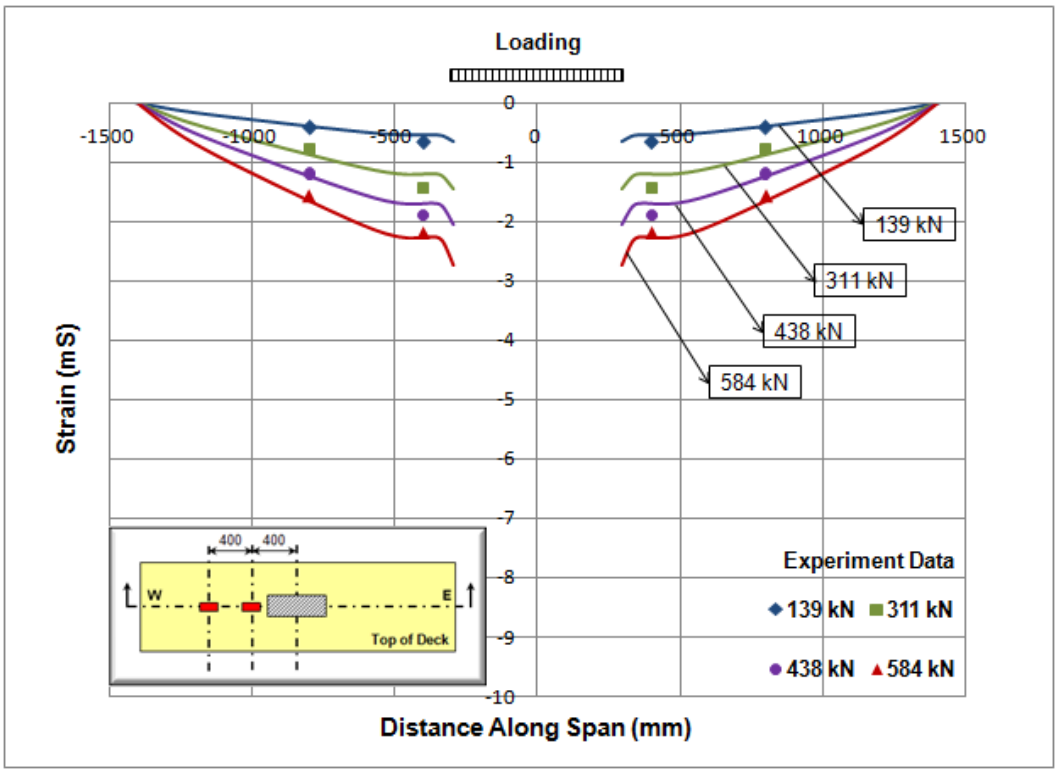

Figure 4.16: Axial strain distribution along centerline of top plate (F7-2)

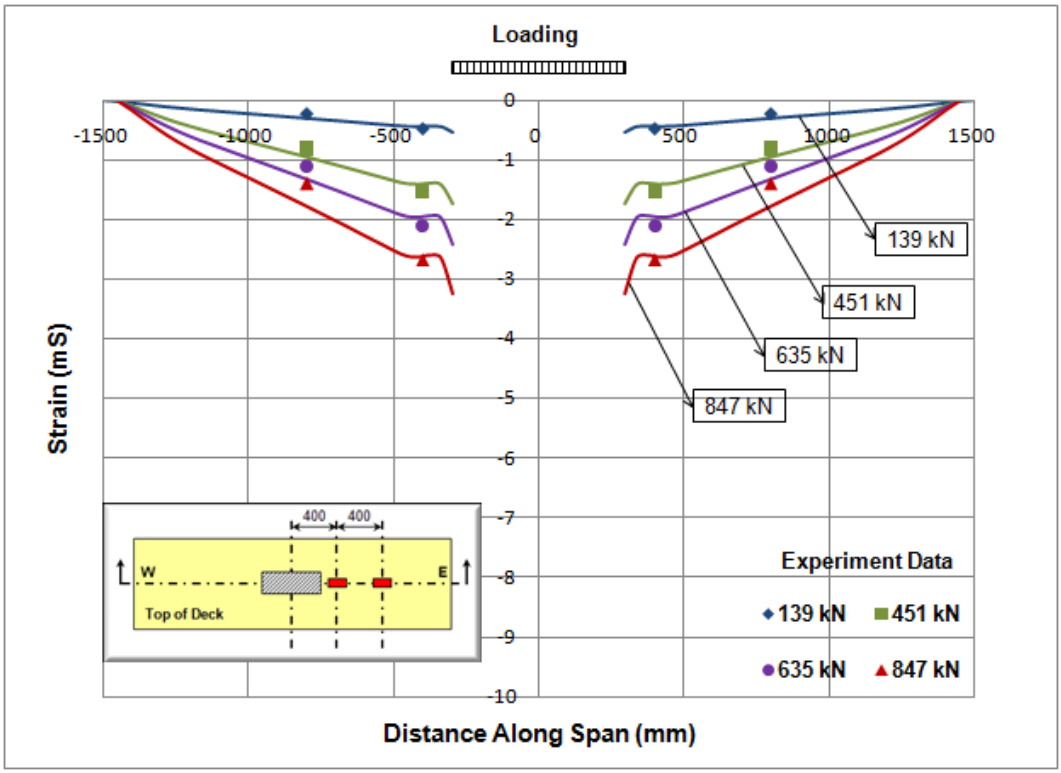

Figure 4.17: Axial strain distribution along centerline of top plate (F9-1)

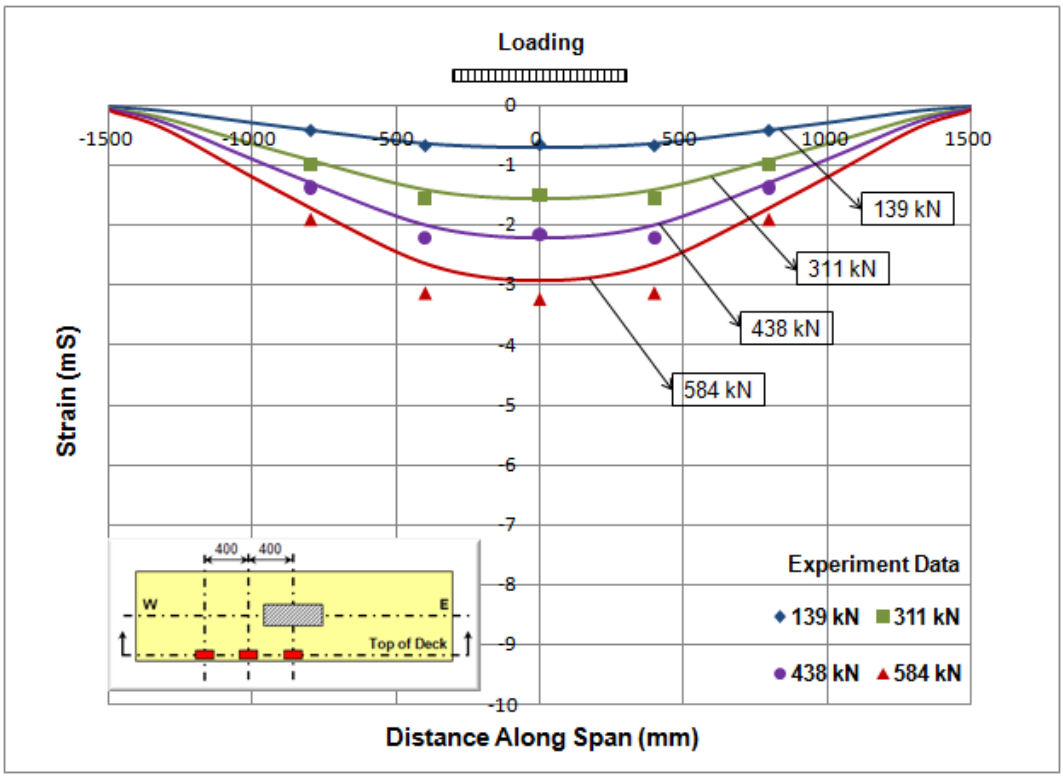

Figure 4.18: Axial strain distribution along edgeline of top plate (F7-2)

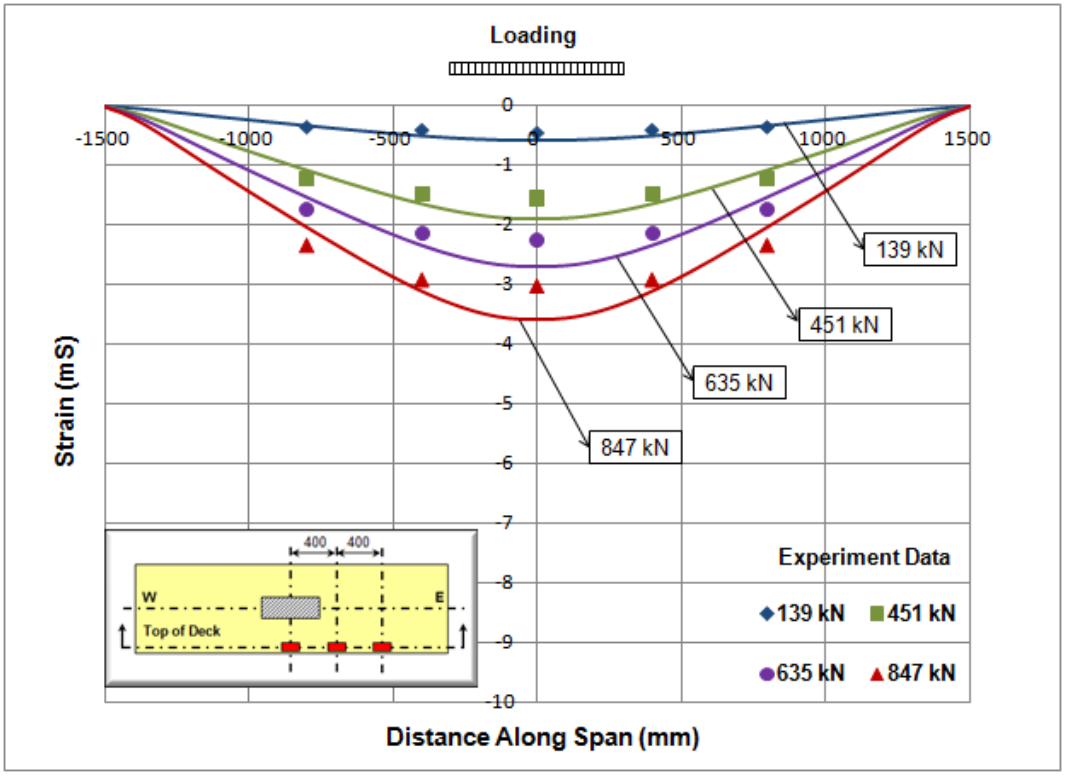

Figure 4.19: Axial strain distribution along edgeline of top plate (F9-1)

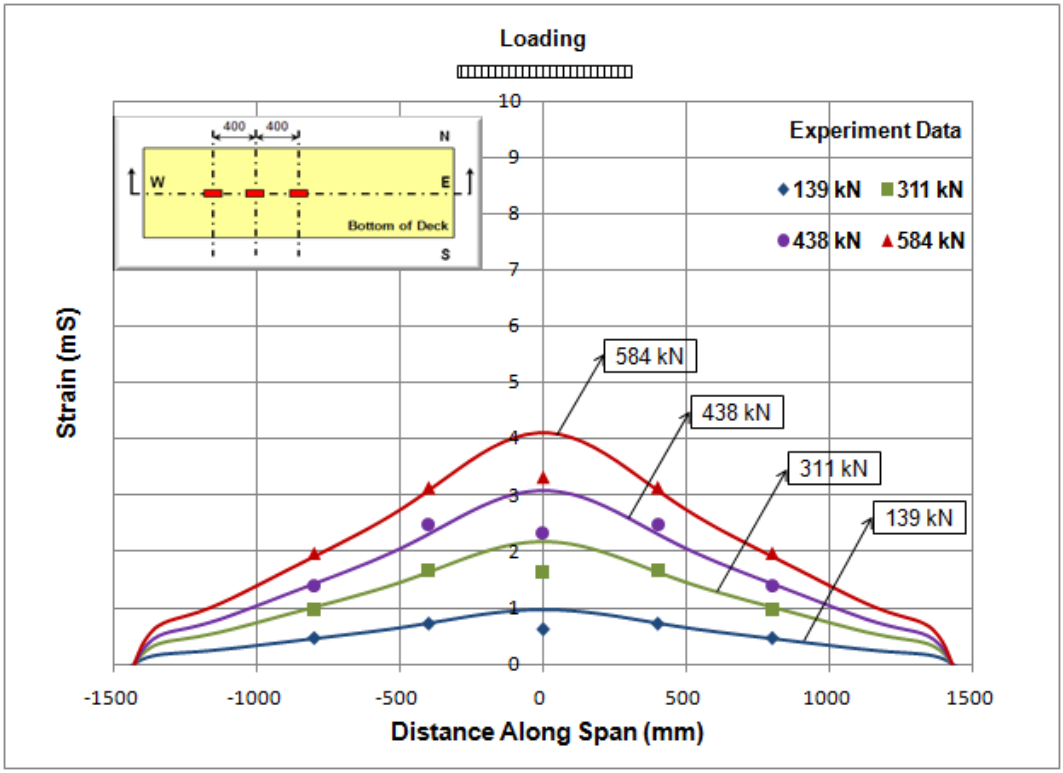

Figure 4.20: Axial strain distribution along centerline of bottom plate (F7-2)

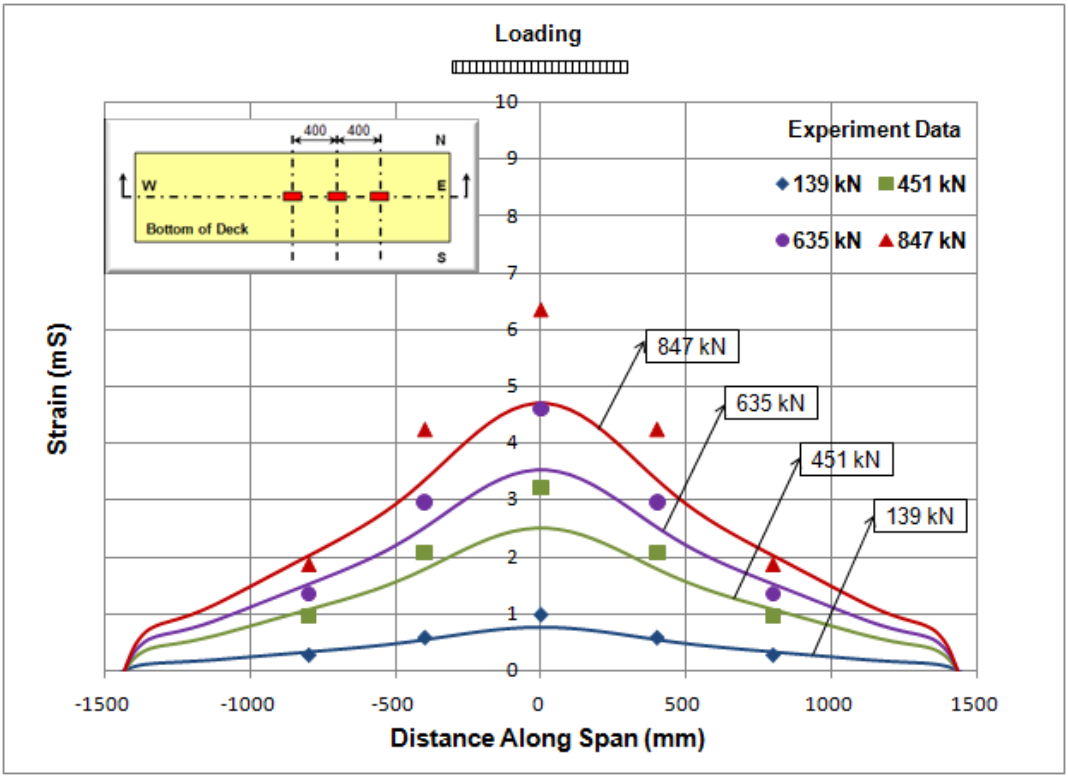

Figure 4.21: Axial strain distribution along centerline of bottom plate (F9-1)

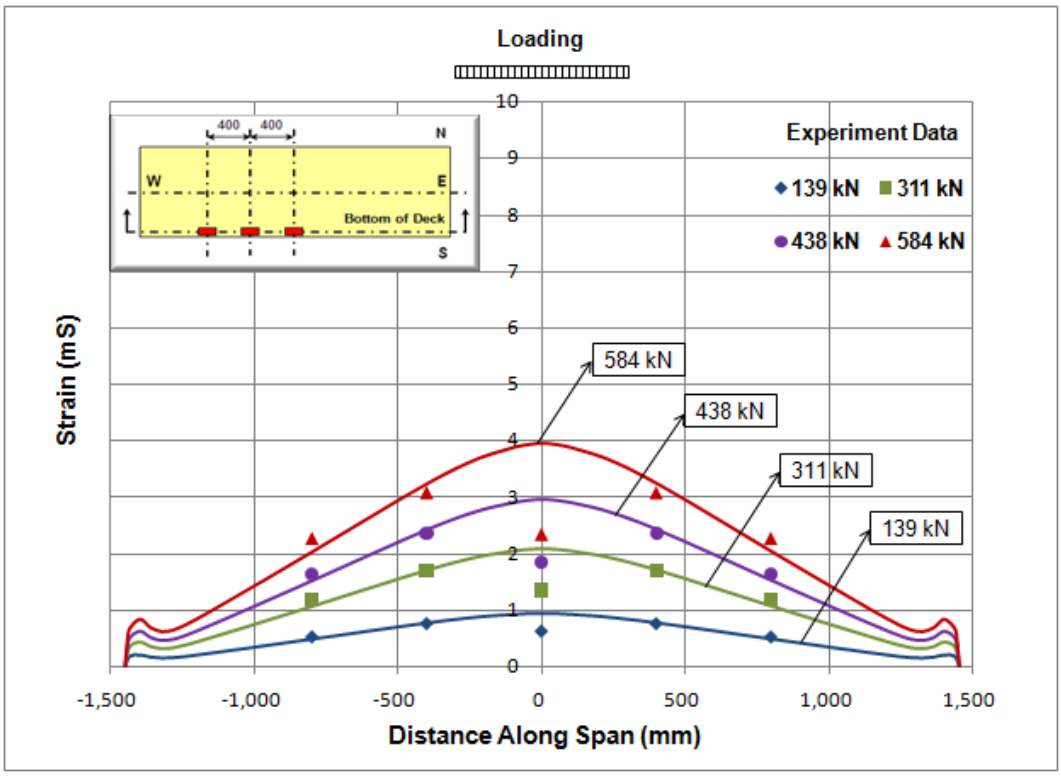

Figure 4.22: Axial strain distribution along edgeline of bottom plate (F7-2)

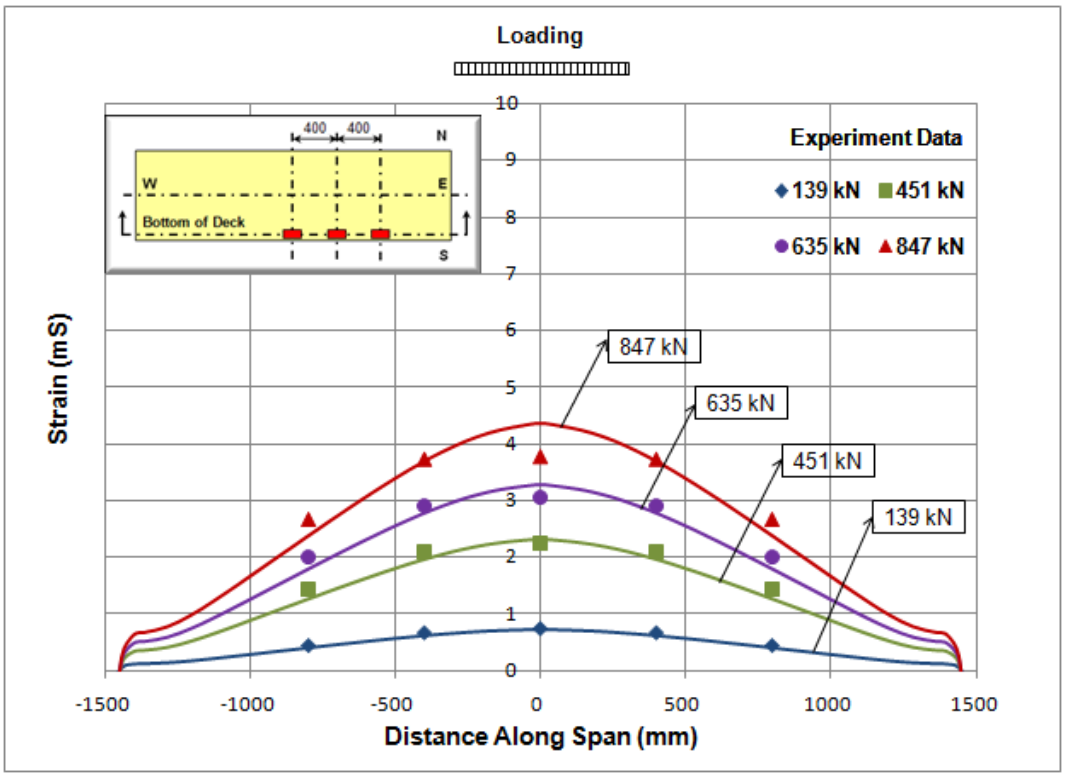

Figure 4.23: Axial strain distribution along edgeline of bottom plate (F9-1)

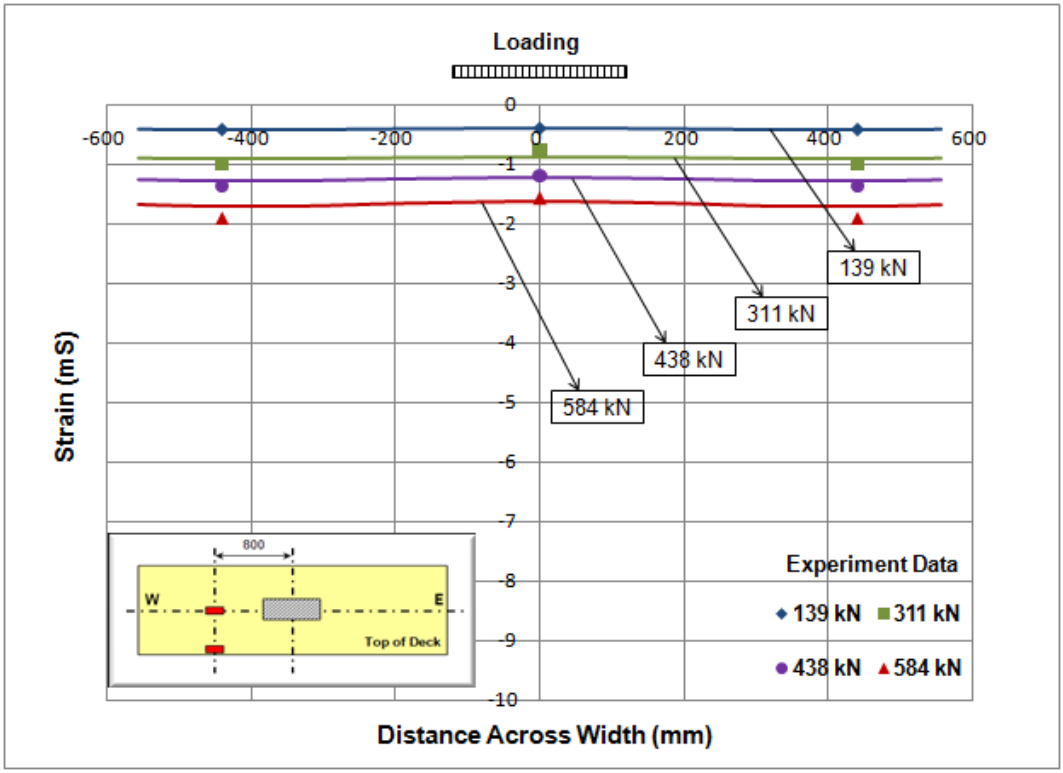

Figure 4.24: Axial strain distribution across top plate 800 mm from centerline (F7-2)

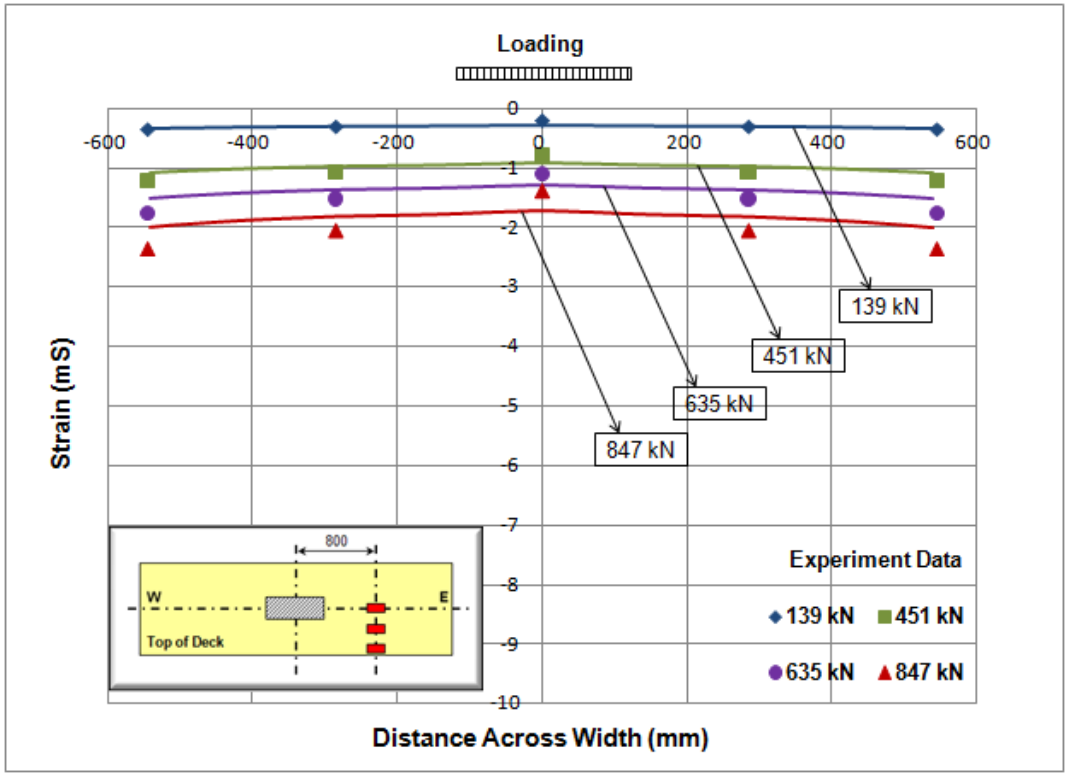

Figure 4.25: Axial strain distribution across top plate 800 mm from centerline (F9-1)

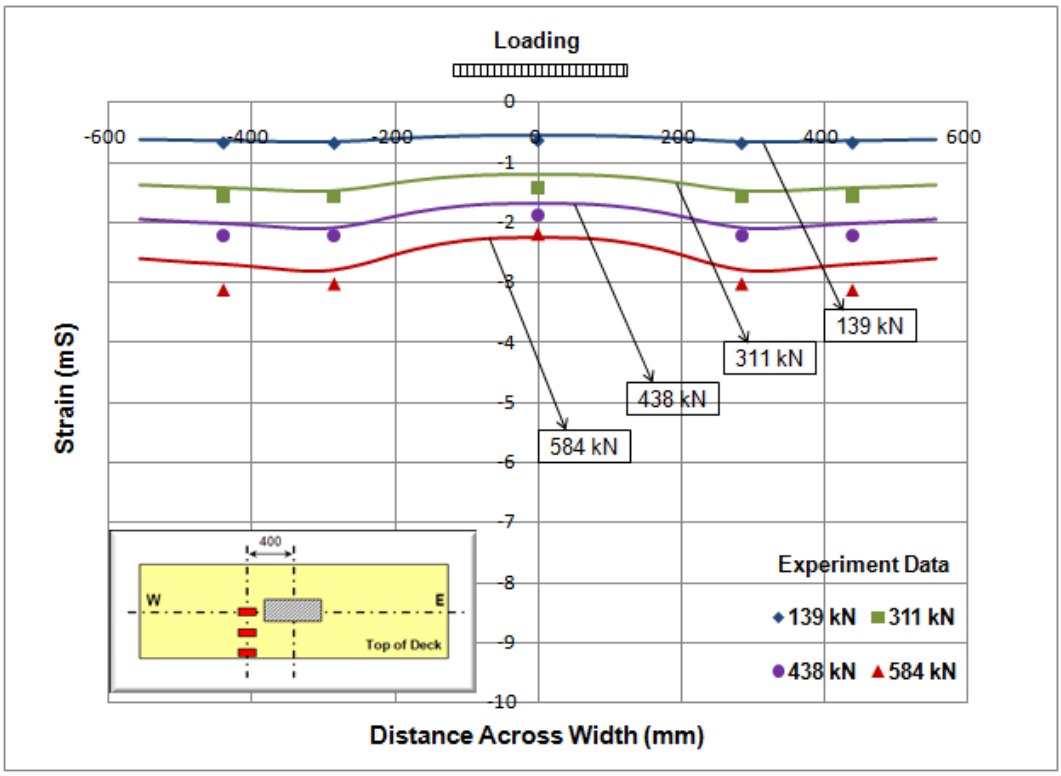

Figure 4.26: Axial strain distribution across top plate 400 mm from centerline (F7-2)

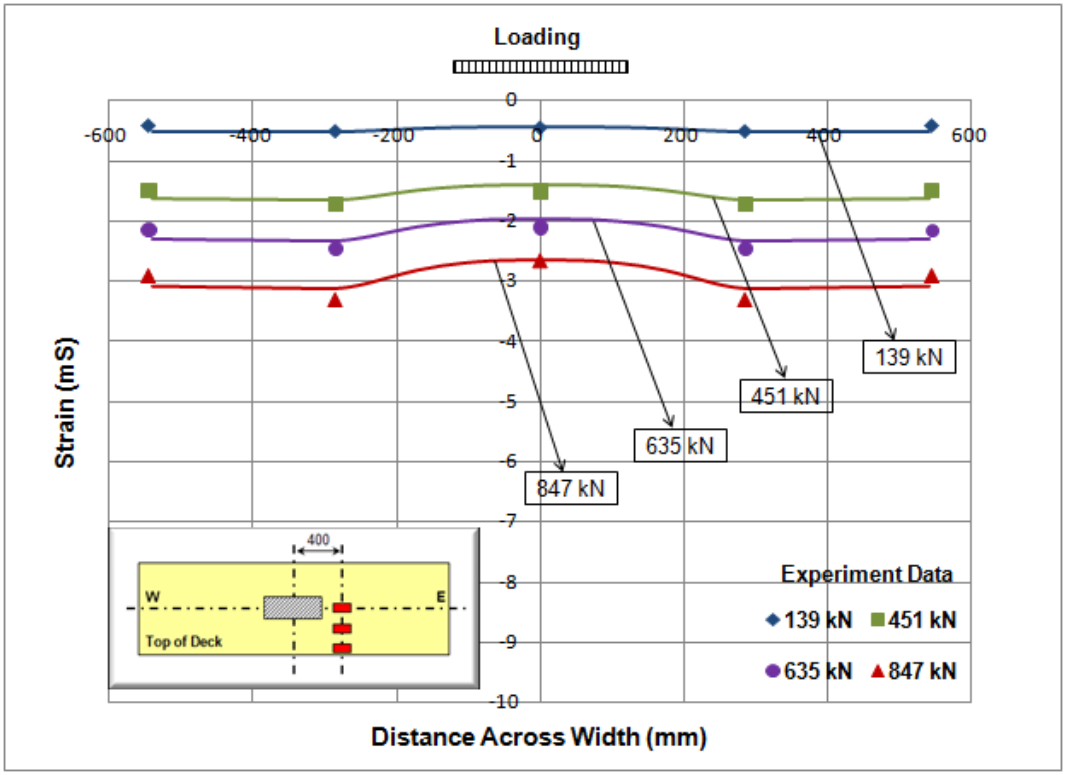

Figure 4.27: Axial strain distribution across top plate 400 mm from centerline (F9-1)

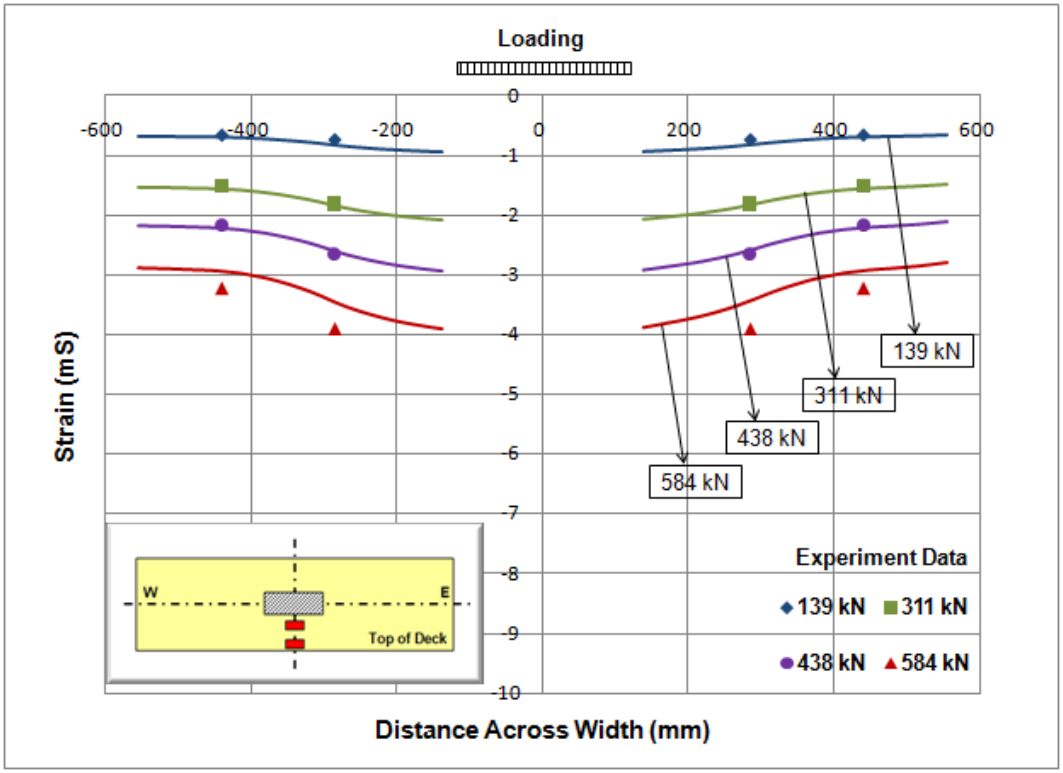

Figure 4.28: Axial strain distribution across top plate at centerline (F7-2)

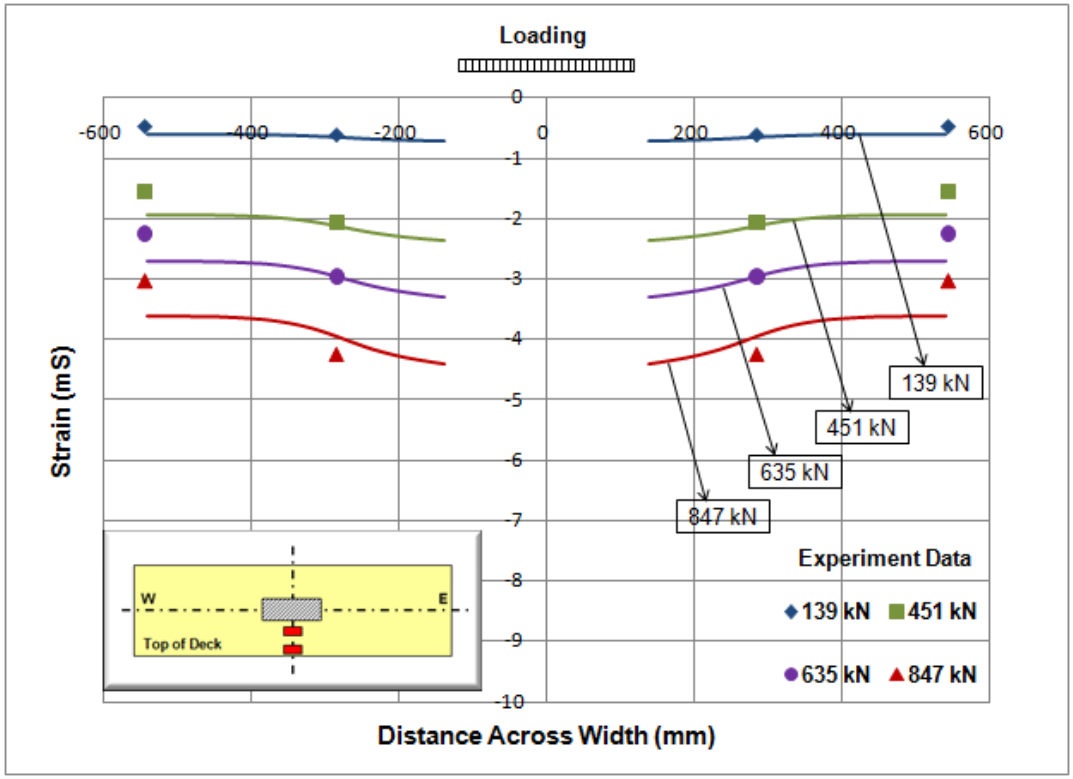

Figure 4.29: Axial strain distribution across top plate at centerline (F9-1)

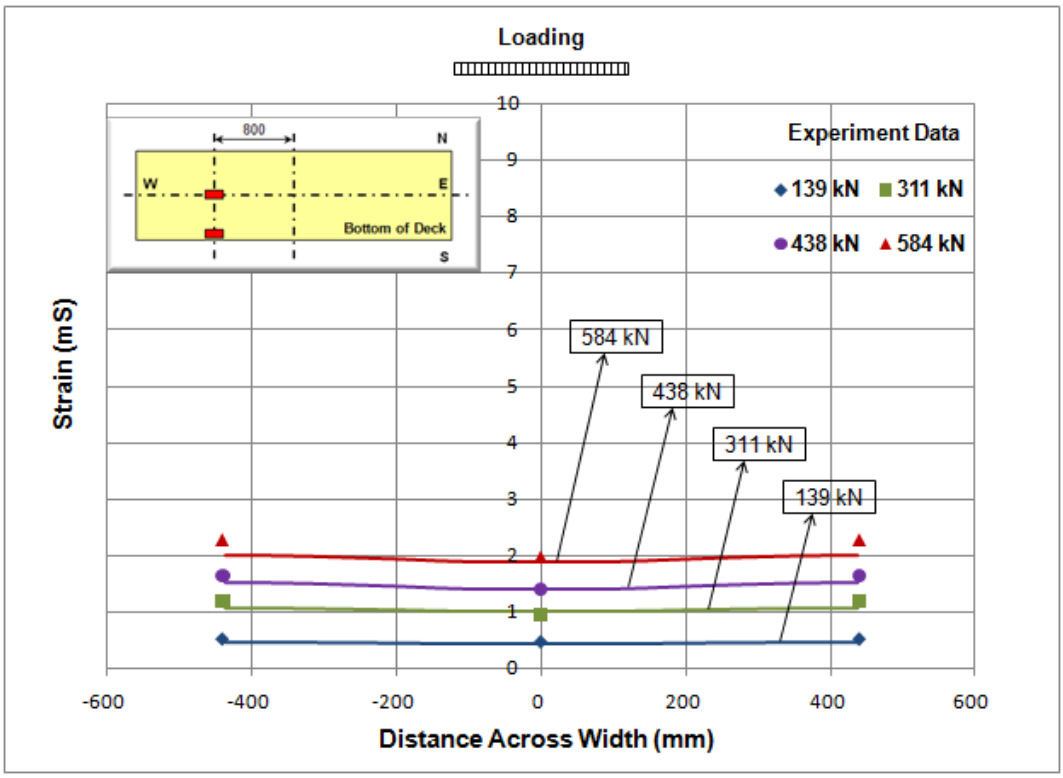

Figure 4.30: Axial strain distribution across bottom plate 800 mm from centerline (F7-2)

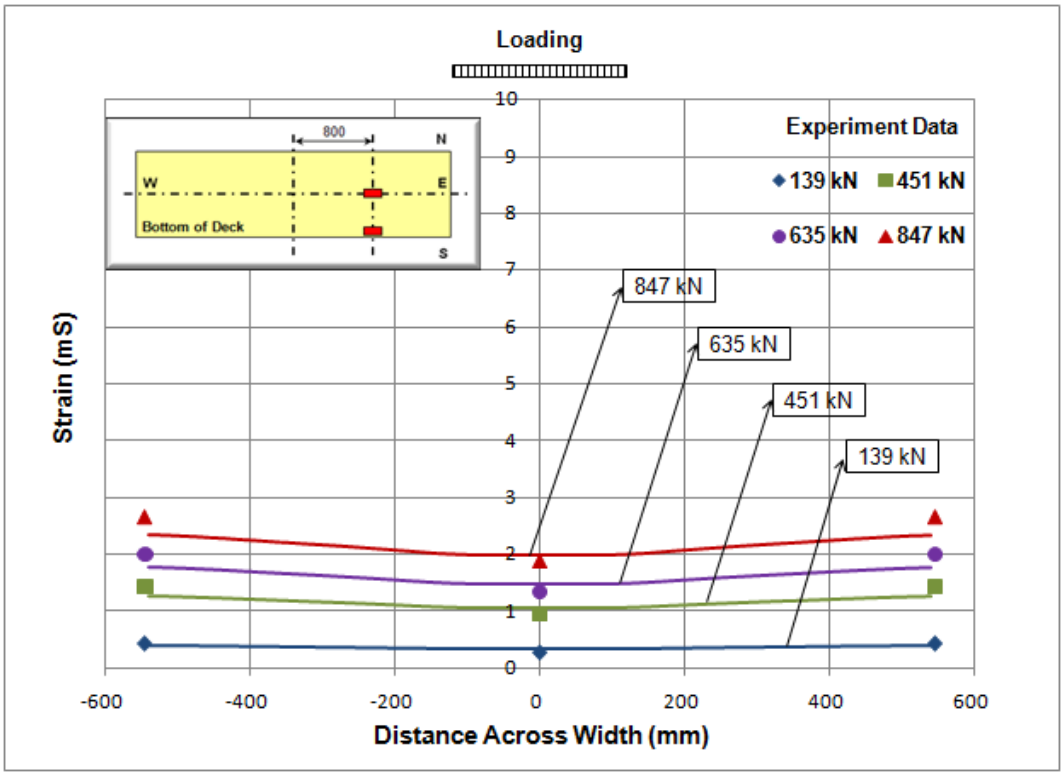

Figure 4.31: Axial strain distribution across bottom plate 800 mm from centerline (F9-1)

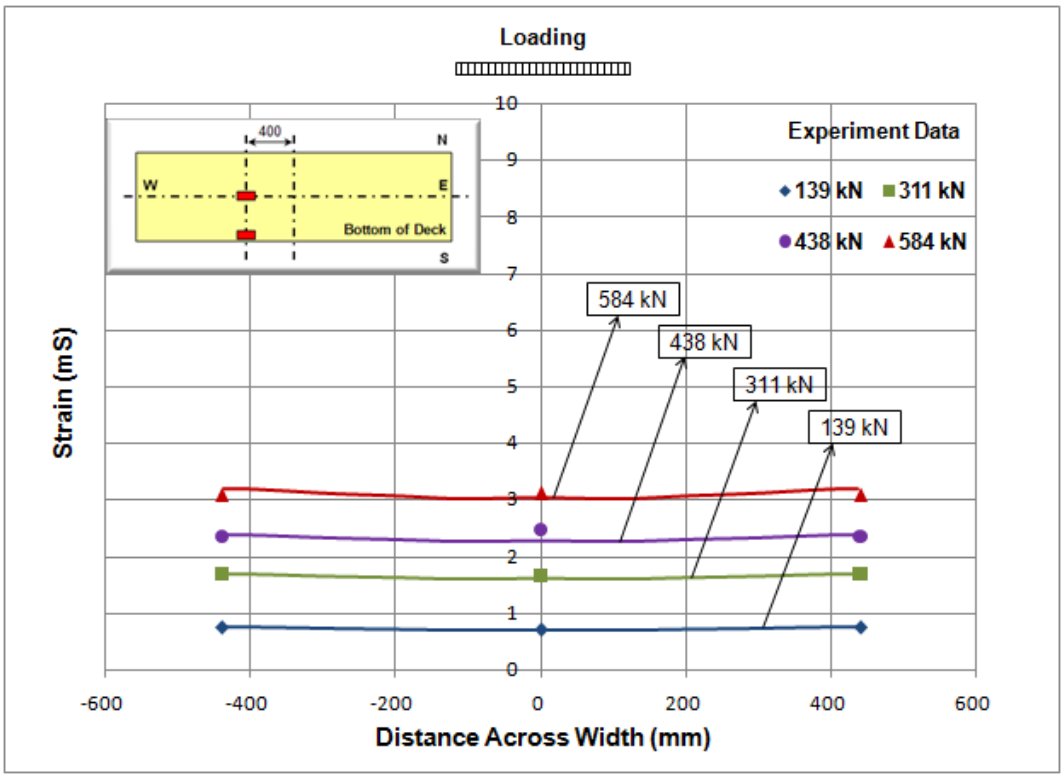

Figure 4.32: Axial strain distribution across bottom plate 400 mm from centerline (F7-2)

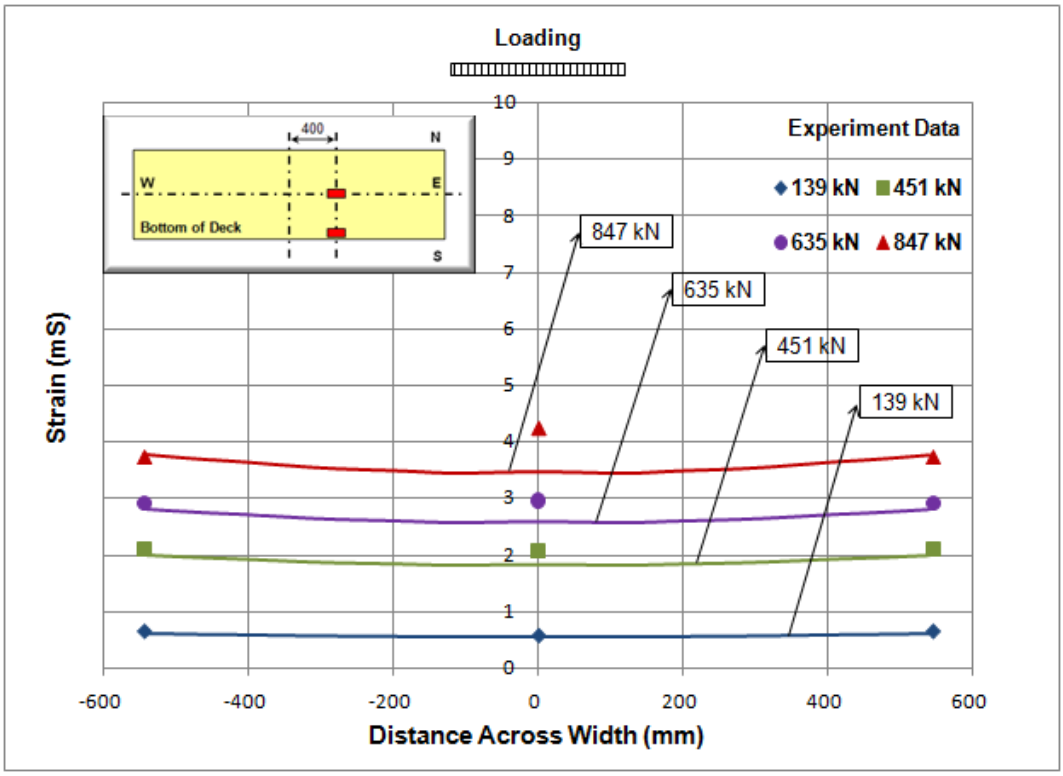

Figure 4.33: Axial strain distribution across bottom plate 400 mm from centerline (F9-1)

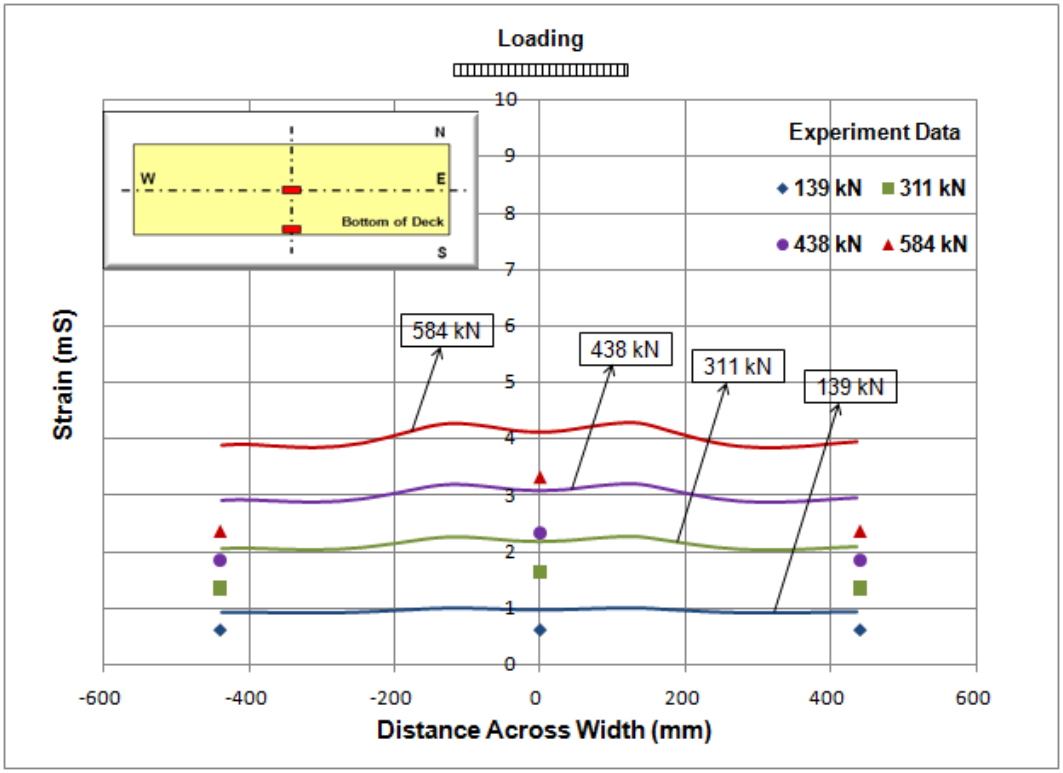

Figure 4.34: Axial strain distribution across bottom plate at centerline (F7-2)

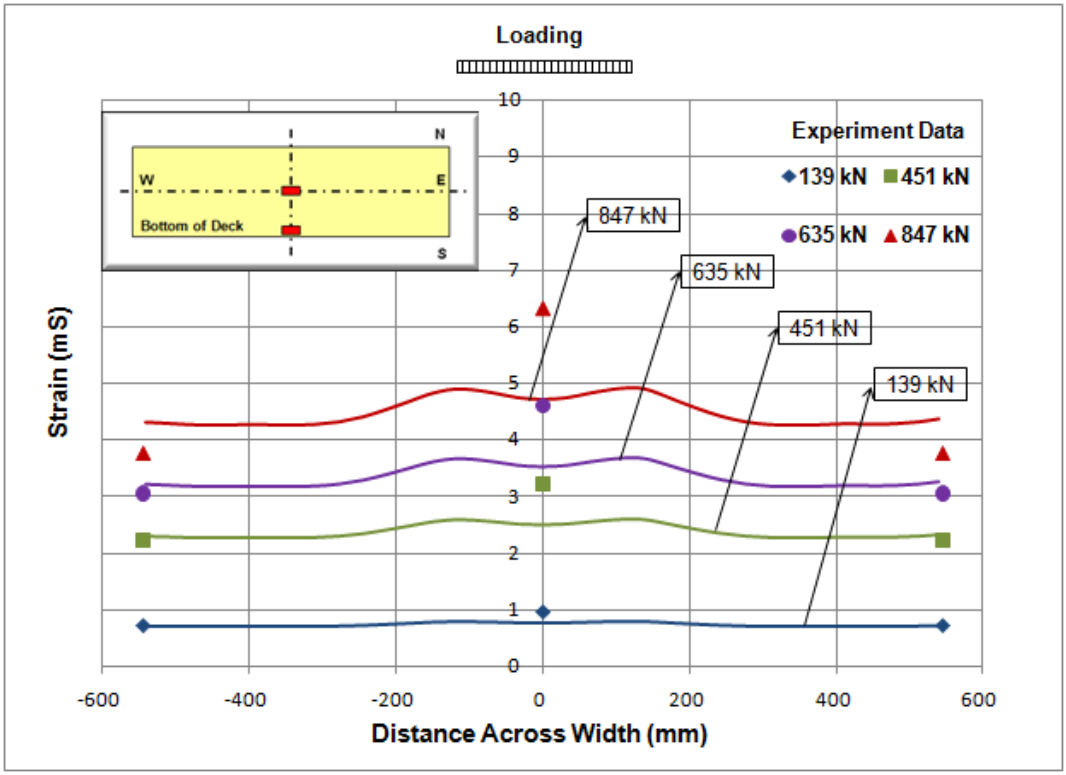

Figure 4.35: Axial strain distribution across bottom plate at centerline (F9-1)

From Figure 4.20, Figure 4.21, Figure 4.34 and Figure 4.35, it was not difficult to find that the predicted axial strain at the center of the bottom plate for each deck specimen did not match the experimental reading very well (LSG 10 of deck F7-2 and LSG 13 of deck F9-1). A possible reason for this mismatch was the simplifying assumption of the uniform load distribution.

According to the calculated axial strain distributions of deck F7-2 and the similarity between the experimental strain profiles of deck F7-2 and those of deck F9-1, the accuracy of the readings of LSG 13 of deck F7-2 was considered questionable (Figure 4.22 and Figure 4.23).

Only one transverse strain gauge was installed on each deck. As an example, the recorded transverse strain behavior of TSG 14 of deck F7-2 is plotted in Figure 4.36. As described by Williams (2000a), the transverse strain data was unreliable, so no inferences could be made.

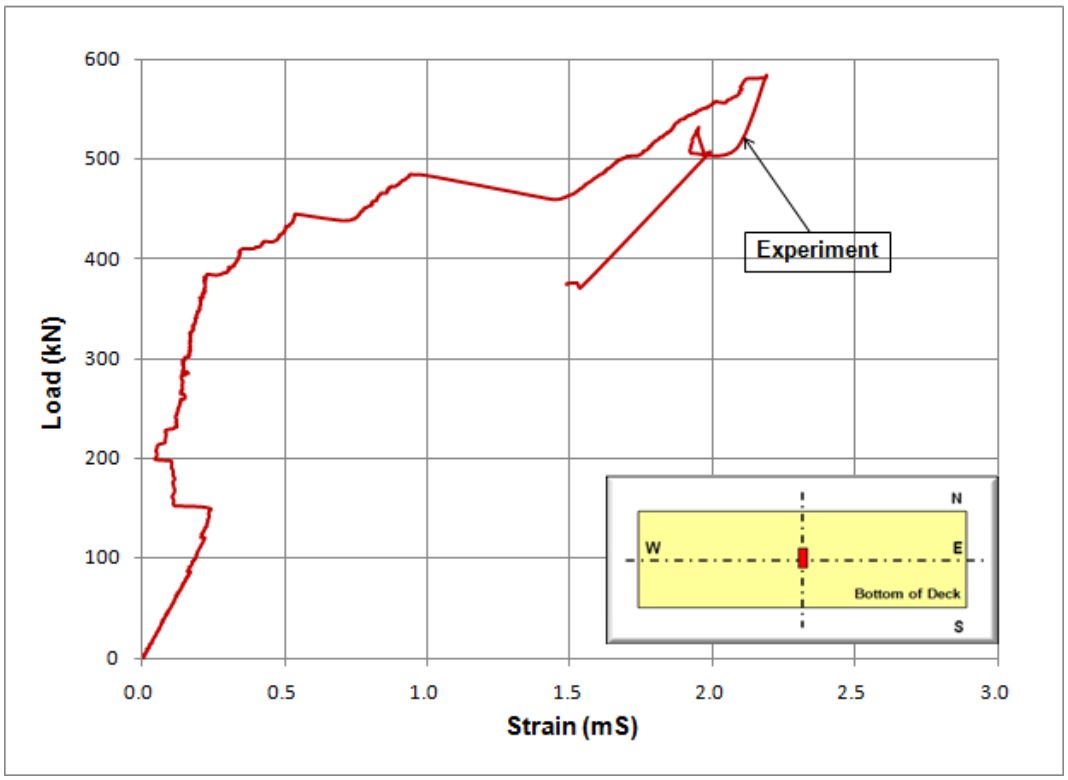

Figure 4.36: Transverse strain behavior of deck F7-2

Overall, the linear analysis model can successfully predict the deflections and axial strains of a FRP bridge deck. However, the accuracies of the predicted deflections and axial strains at certain parts of the FRP bridge deck may be compromised due to the possibilities of lamina failure, delamination propagation, and structural buckling.

4.2.5 Eigenvalue Buckling Load

A FRP bridge deck is a thin-walled structure. The webs and top surface are subjected to compressive stresses, which may cause buckling failure of the deck. Linear analysis model can be employed to predict the buckling failure load and the buckling mode shape of a FRP bridge deck.

Eigenvalue buckling analysis, also named linear buckling analysis, can determine the theoretical buckling strength of an ideal linear elastic structure. But all field structures have a certain degree of nonlinearities and imperfections that will prevent them from reaching their theoretical eigenvalue buckling loads; i.e., the eigenvalue buckling analysis always yields results that are not conservative, as shown in Figure 4.37. Nonlinear buckling analysis usually gives a better prediction of the buckling failure load; however, it is very time consuming and it is difficult to determine the extent of nonlinearities and imperfections of an actual structure. Therefore, the eigenvalue buckling analysis approach, based on linear analysis model, was chosen for this research.

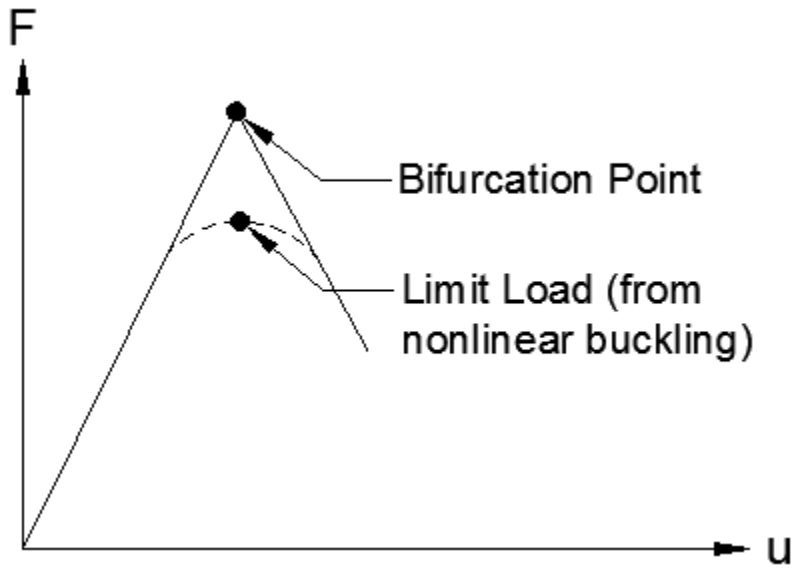

Figure 4.37: Eigenvalue buckling curve (adapted from ANSYS, Inc., 2007b)

The Block Lanczos method was selected for the extraction of the eigenvalue and eigenvector. A detailed description of the Block Lanczos method can be found in "Eigenvalue and Eigenvector Extraction" (ANSYS, Inc., 2007c).

The fundamental buckling mode shapes of all three generations of filament-wound GFRP bridge deck were the same. It was the web right beneath the loading plate that buckled. Figure 4.38 presents the fundamental buckling mode shape of deck F9-1.

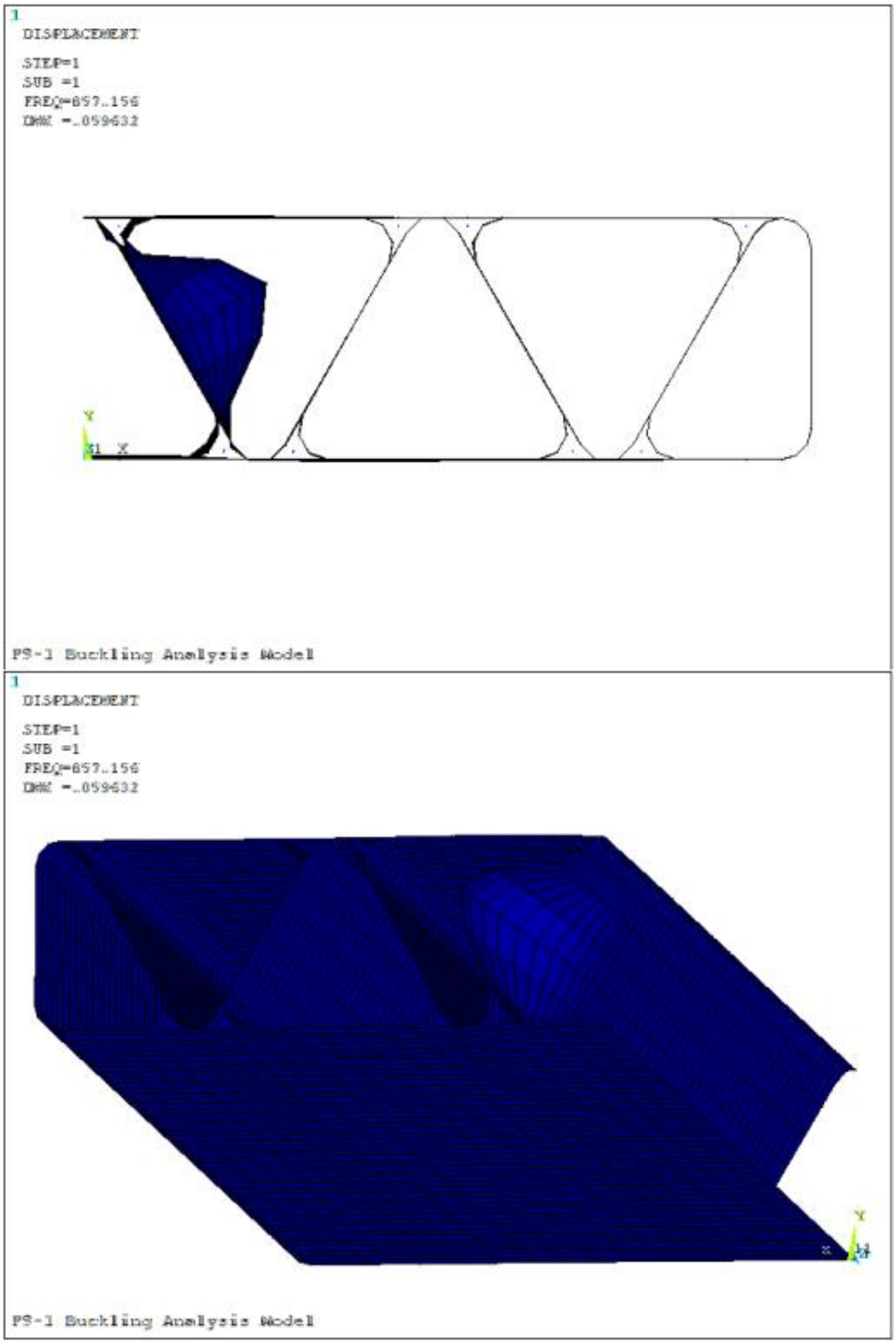

Figure 4.38: Fundamental buckling mode shape of deck F9-1 (quarter model)

The eigenvalue buckling loads of deck F7-2, deck F9-1 and deck F10-1 are plotted with dashed lines in Figure 4.39 through Figure 4.41.

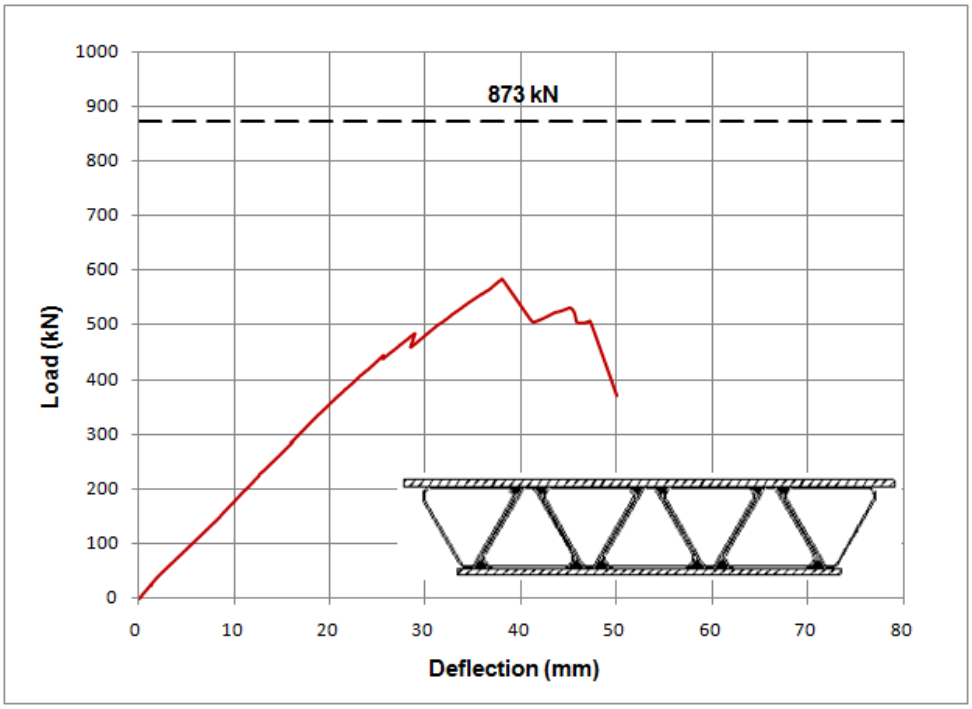

Figure 4.39: Nonlinear buckling load of deck F7-2

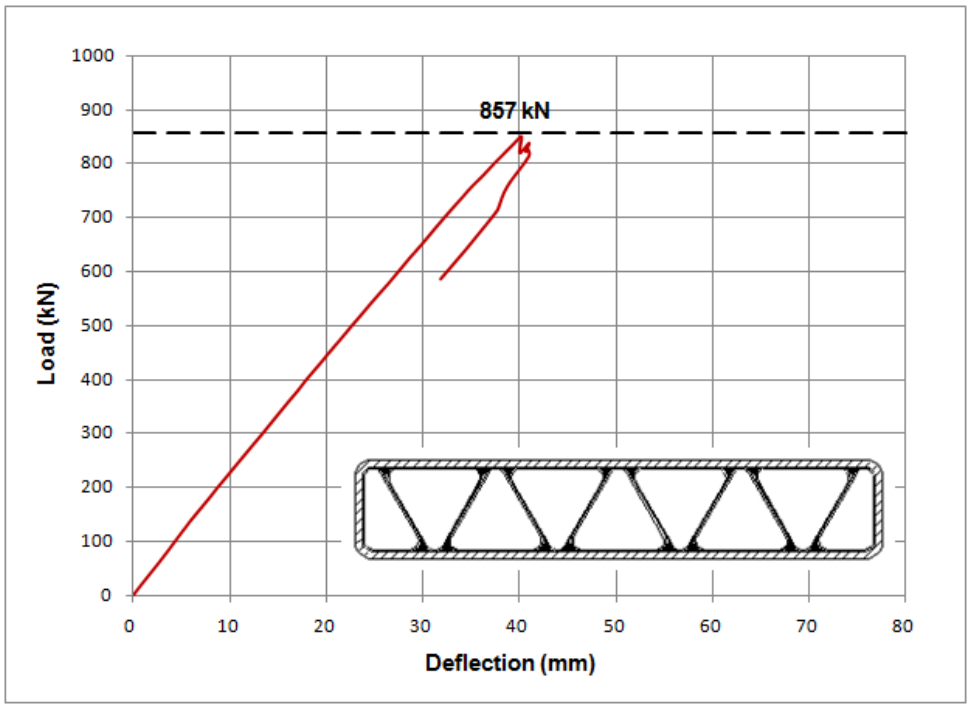

Figure 4.40: Nonlinear buckling load of deck F9-1

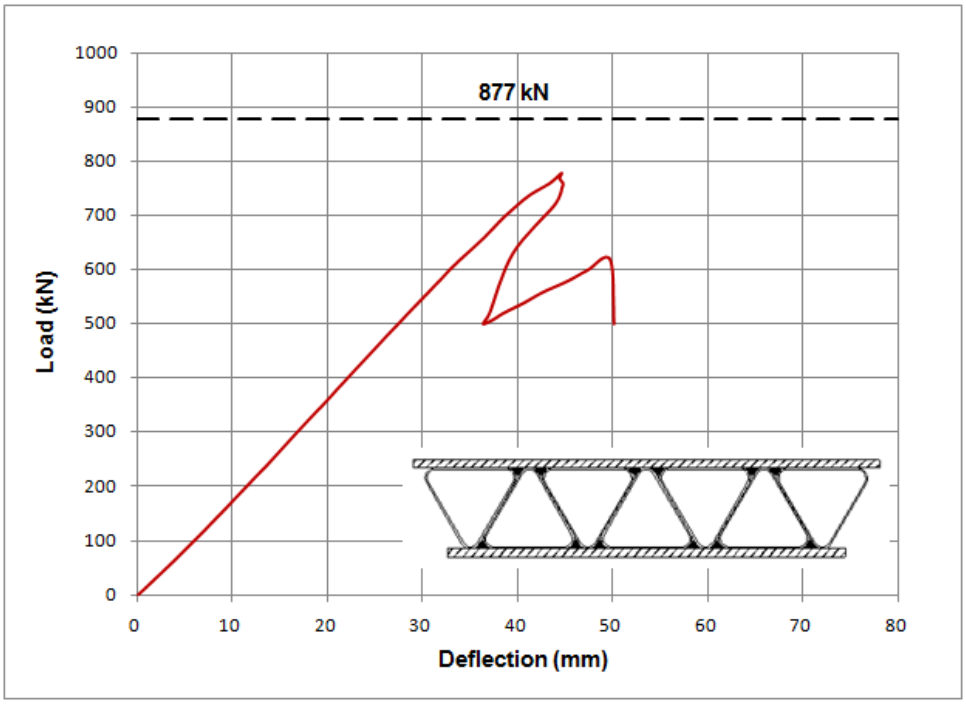

Figure 4.41: Nonlinear buckling load of deck F10-1

Since the failure of deck F7-2 was due to rapid delamination propagation, it was reasonable that the predicted eigenvalue buckling load was 49.5% higher than its actual failure load. For deck F9-1 and deck F10-1, delamination buckling was their failure mode and the delamination that happened to them was localized; therefore, the predicted eigenvalue buckling loads of deck F9-1 and deck F10-1 should be close to the test results. The analysis results confirmed that the predicted eigenvalue buckling loads of deck F9-1 and deck F10-1 were 1.2% and 12.4% higher than their actual failure loads, respectively.

Two reasons could explain why rapid delamination propagation happened to deck F7-2 but not deck F9-1 or deck F10-1: 1) all the components of deck F9-1 and deck F10-1 were glued together with epoxy resin before the final epoxy resin infusion process (Williams, 2000a; Crocker, 2002), as shown in Figure 4.42; 2) quality control was

improved for the manufacture of deck F9-1 and deck F10-1 after the fabrication of the first-generation and second-generation GFRP bridge decks.

Figure 4.42: Spreading epoxy resin on a triangular inside tube (Crocker, 2001)

The calculated eigenvalue buckling load of deck F9-1 was closer to its experimental failure load than the eigenvalue buckling load of deck F10-1 was. There were two reasons why this happened. First, the FPF load of deck F9-1 was 74 kN higher than the FPF load of deck F10-1. Second, compared with deck F10-1, deck F9-1 suffered less delamination before the final buckling failure took place. It was confirmed that filament-wound outside shell of deck F9-1 played an important role in restraining the delamination propagation.

Overall, the linear analysis model can predict the buckling failure load and the buckling mode shape of a FRP bridge deck successfully on the condition that limited damage

happens to the FRP bridge deck. Since the eigenvalue buckling analysis always over-predicts the buckling failure loads, it is recommended as an indicator of upper bound failure criterion for the design of FRP bridge decks.

4.3 Delamination Analysis Model

Delamination of FRP bridge decks is always a significant concern as an initiation of failure. To assess this matter, the delamination analysis model is developed to point out potential delamination zones.

4.3.1 Building the Delamination Analysis Model

Four types of elements were used to build the delamination analysis model, which were LINK8, SHELL91, TARGE170 and CONTA174. LINK8 element was employed to model the pultruded GFRP filler bars as same as in the linear analysis model. The other three types of elements were described as follows.

Instead of the SHELL99 (linear layered structural shell) element, the SHELL91 element was employed to model the equilateral-triangular inside tubes, the top and bottom plates of the second-generation GFRP deck, and the outside shell of the third-generation GFRP deck. SHELL91 is an eight-node, nonlinear layered structural shell element with six degrees of freedom at each node: translations in the nodal x, y and z directions and rotations about the nodal x, y and z axes (ANSYS, Inc., 2007a). Figure 4.43 shows the geometry, node locations, and the coordinate system of this element. Compared with the

SHELL99 element, the SHELL91 element can allow up to a maximum of 100 layers; however, it is more robust for nonlinear structural analysis. The layered configuration of each SHELL91 element, including orthotropic material properties, layer orientation angle and layer thickness, is defined in the same way as the SHELL99 element.

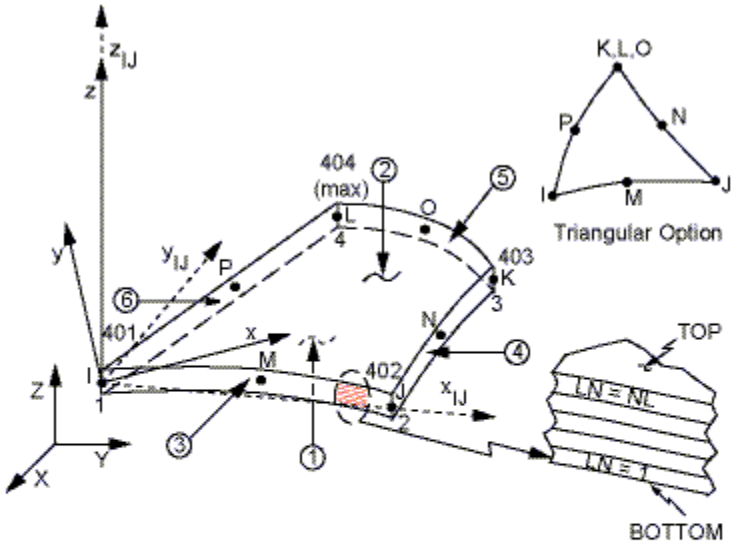

x_{IJ} = Element x-axis if ESYS is not supplied.

x = Element x-axis if ESYS is supplied.

LN = Layer Number

NL = Total Number of Layers

Figure 4.43: SHELL91 geometry (ANSYS, Inc., 2007a)

Interface delamination can be modeled with contact pairs that are bonded and have a defined cohesive zone material model. The typical 3-D surface-to-surface contact pair comprises the CONTA174 element and the TARGE170 element, which were used in the delamination analysis model. CONTA174, a 3-D eight-node surface-to-surface contact element, is utilized to represent contact and sliding between 3-D target surfaces and a deformable surface defined by this element (ANSYS, Inc., 2007a). Figure 4.44 shows the

geometry and node locations of this element. In the delamination analysis model, CONTA174 elements were located on the surfaces of the 3-D SHELL91 elements and they had the same geometric characteristics as the connected SHELL91 elements.

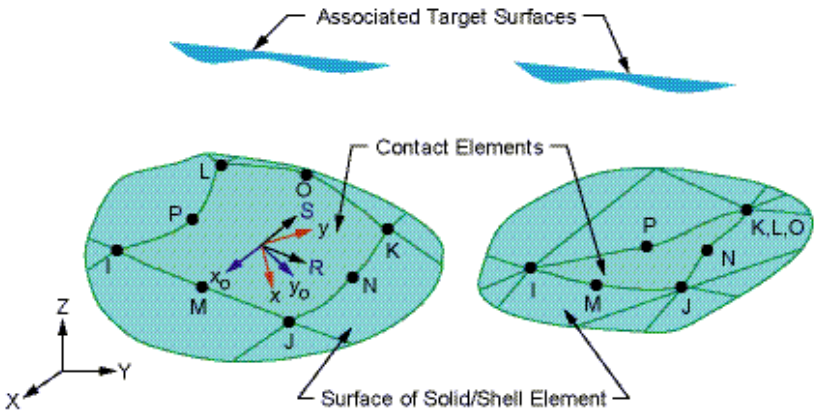

R = Element x-axis for isotropic friction

x_o = Element axis for orthotropic friction if **ESYS** is not supplied (parallel to global X-axis)

x = Element axis for orthotropic friction if **ESYS** is supplied

Figure 4.44: CONTA174 geometry (ANSYS, Inc., 2007a)

TARGE170, a 3-D target segment element, is used to represent a variety of 3-D target surfaces for the corresponding contact surfaces (ANSYS, Inc., 2007a). This target surface is discretized by TARGE170 elements and is paired with its corresponding contact surface through a shared real constant set. For rigid target surfaces, complex target shapes can be modeled easily using TARGE170 elements. For flexible targets, TARGE170 elements are placed on top of the line, shell or solid elements showing the boundary of the deformable target body. Figure 4.45 shows the geometry and node locations of this element.

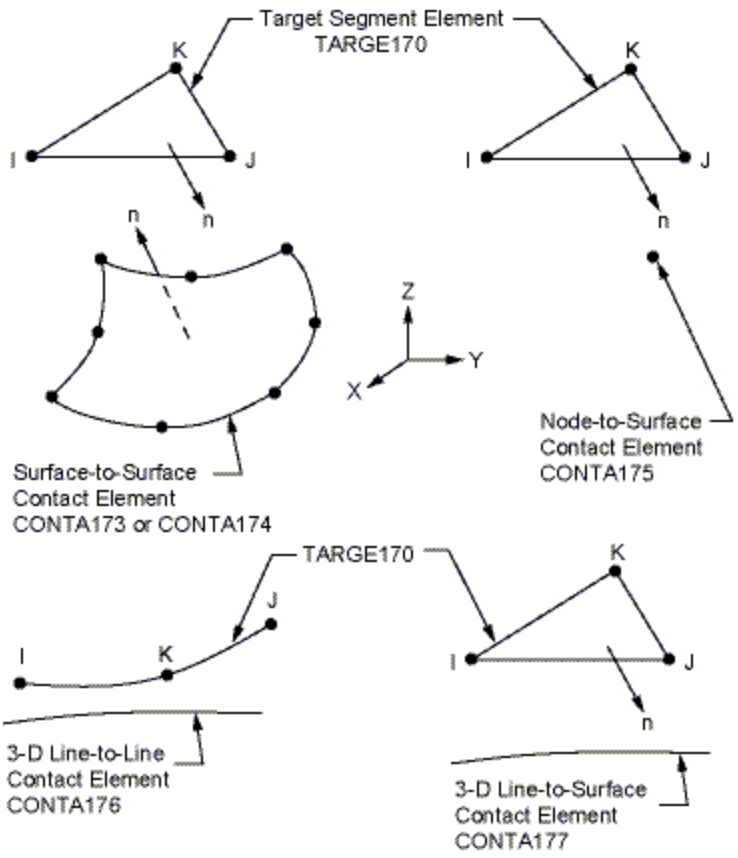

Figure 4.45: TARGE170 geometry (ANSYS, Inc., 2007a)

The Cohesive Zone Model (CZM), which was developed within the framework of damage mechanics and softening to simulate the delamination initiation and propagation, was utilized in the delamination analysis model. Contact pairs are placed between composite plies but do not represent any physical material. Delamination is understood as the development of a cohesive damage zone near the delamination front, separating the adjacent plies. The interface is characterized by constitutive equations that relate the traction acting on the interface to the corresponding interfacial separation. The three typical traction-separation laws for CZM are the exponential, trapezoidal, and bilinear

traction-separation laws. The bilinear cohesive zone material model proposed by Alfano and Crisfield (2001) was chosen in this delamination analysis.

Interfacial delamination allows three modes of separation: normal separation, tangential separation, and combined normal and tangential separation. The mode I delamination is described as the separation normal to the interface dominating the slip tangent to the interface. The normal tensile contact stress is plotted versus the contact gap in Figure 4.46. This curve is divided into three stages: linear elastic stage, linear softening stage, and decohesion stage. The slope of the curve depends on the normal contact stiffness and the debonding parameter. The area under the curve OAC is the critical fracture energy required for model I delamination. The mode II delamination is described as the slip tangent to the interface dominating the separation normal to the interface. The bilinear relationship between the tangential contact stress and the tangential slip distance is quite similar to that of mode I delamination (Figure 4.46).

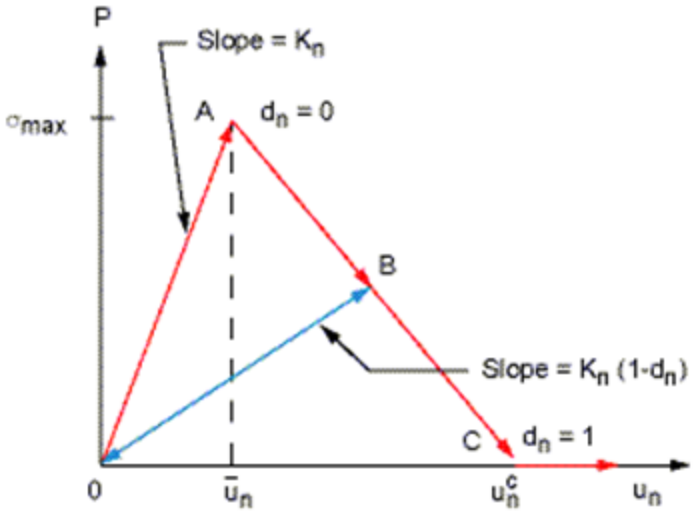

P = normal contact stress

K_n = normal contact stiffness

u_n = contact gap

$\bar{u}_n$ = contact gap at the maximum normal contact stress

u_n^c = contact gap at the completion of debonding

d_n = debonding parameter

σ_{max} = maximum normal contact stress

Figure 4.46: Normal contact stress and contact gap curve for bilinear cohesive zone material model (ANSYS, Inc., 2007d)

The mixed model delamination relies on both the normal and tangential components. Normal and tangential contact stresses together contribute to the total fracture energy. Debonding is completed before the critical fracture energy values of both components are reached. Consequently, an appropriate interaction relation to define the completion of delamination is considered as (Garg, 1988):

$$\left(\frac{G_n}{G_{cn}}\right) + \left(\frac{G_t}{G_{ct}}\right) = 1 \tag{4.18}$$

Where:

G_n = normal fracture energy

G_t = tangential fracture energy

G_{cn} = critical fracture energy for normal separation

G_{ct} = critical fracture energy for tangential slip

Modeling bilinear cohesive zone material behavior, the following material constants need to be determined: maximum normal contact stress (σ_{max}), maximum equivalent tangential contact stress (τ_{max}), critical fracture energy for normal separation (G_{cn}), critical fracture energy for tangential slip (G_{ct}), normal contact stiffness (K_n), and tangential contact stiffness (K_t). The maximum normal contact stress and maximum equivalent tangential contact stress usually can be found in the product data sheets provided by FRP manufacturers.

The critical fracture energies for normal separation and tangential slip are usually determined through laboratory tests. The Double Cantilever Beam (DCB) specimen and the Width-Tapered Double Cantilever Beam (WTDCB) specimen have been used by many researchers to determine the critical fracture energy for normal separation. The End-Notched Flexure (ENF) specimen and the End-Loaded Split (ELS) specimen are used to determine critical fracture energy for tangential slip. The test results from Prel et al. (1989) were employed in the delamination analysis model.

There are various empirical guidelines for selecting the contact stiffness of the interface. In order to simulate delamination process with CZM, it is necessary that the cohesive contribution to the global compliance before crack propagation be small enough to avoid introducing a fictitious compliance to the delamination analysis model. Travesa (2006) proposed the following closed-form formula for calculating the normal contact stiffness due to mechanical considerations:

$$K_n = \frac{\alpha E_{33}}{t} \tag{4.19}$$

Where:

t = thickness of an adjacent sublaminate

α = a parameter much larger than 1 ($\alpha \gg 1$)

It is noted that large values of contact stiffness may lead to spurious oscillations of the tractions. Therefore, the recommended value of α (=50) was chosen in this delamination analysis, which resulted in only 2% loss of stiffness due to the existence of the interface. Equation (4.19) is applicable for calculating the normal contact stiffness. For the tangential contact stiffness, the corresponding out-of-plane shear modulus needs to be used instead of E_{33}.

For deck F10-1, no photos related to delamination were published; therefore, the delamination analysis was not conducted on deck F10-1. Delamination analysis models of the second-generation and third-generation filament-wound GFRP bridge decks were built based on the dimensions of test specimens. Using the symmetry, only one-quarter of the model was created with appropriate symmetric boundary conditions. The applied load was also simulated as a uniformly distributed pressure over the loading area. But in

contrast to the linear analysis model, the delamination analysis model required the proper placement of the contact pairs with assigned cohesive zone material model. Locations of contact pairs for deck F7-2 are shown in Figure 4.47. The bold lines in this figure represent the contact pairs, which were placed between all the bridge deck components except at the interfaces between the outmost equilateral-triangular tube and two laid-up plates. The reasons for this arrangement were that no delamination was observed between the outmost equilateral-triangular tube and two laid-up plates during the test, and less nonlinear CONTA174 and TARGE170 elements could reduce processing time. Similar to deck F7-2, contact pairs with assigned cohesive zone material model were also placed in the appropriate positions of deck F9-1.

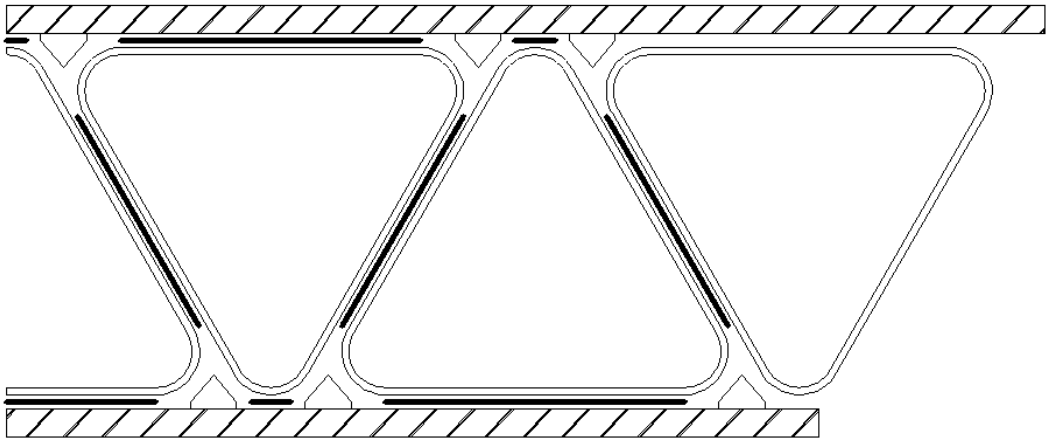

Figure 4.47: Locations of contact pairs for deck F7-2

Delamination analysis models of deck F7-2 and deck F9-1 are presented in Figure 4.48, Figure 4.49, respectively.

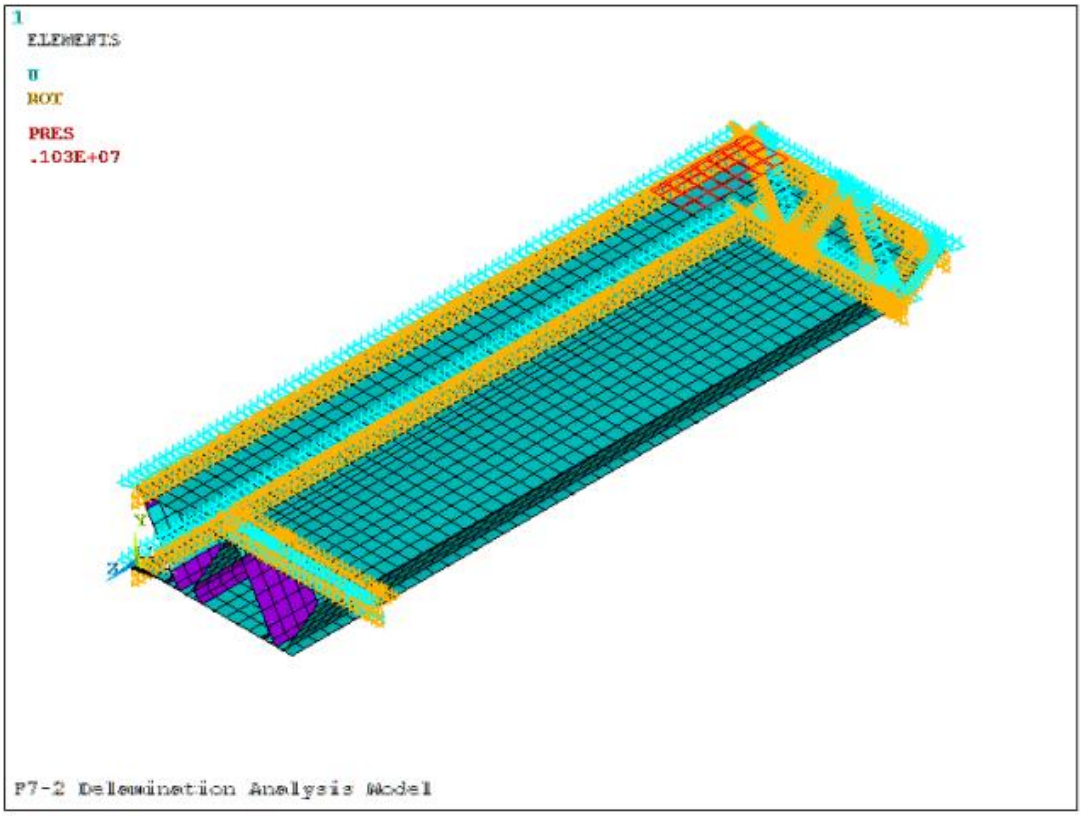

a. Isometric view

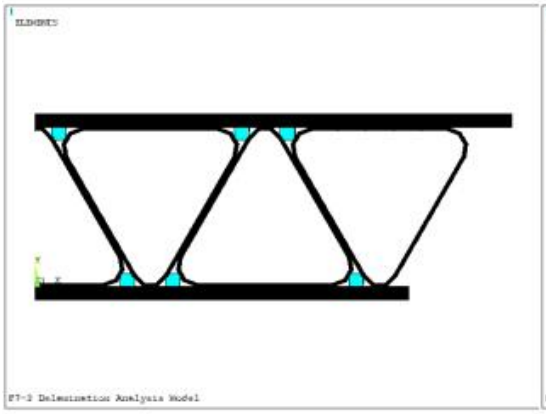

b. Front view

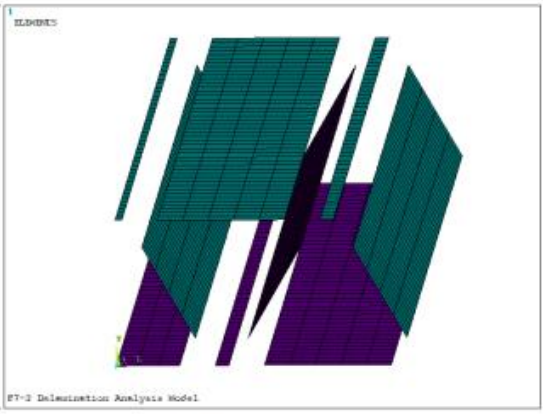

c. Contact pairs

Figure 4.48: Delamination analysis model of deck F7-2

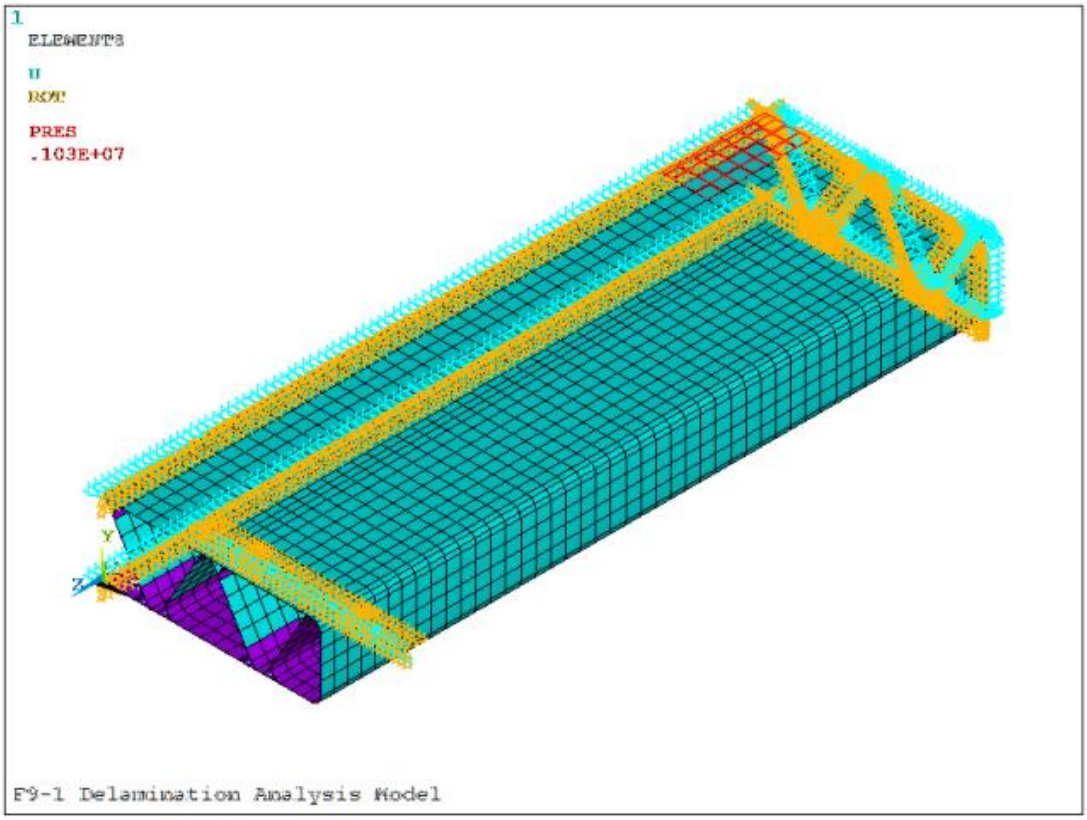

a. Isometric view

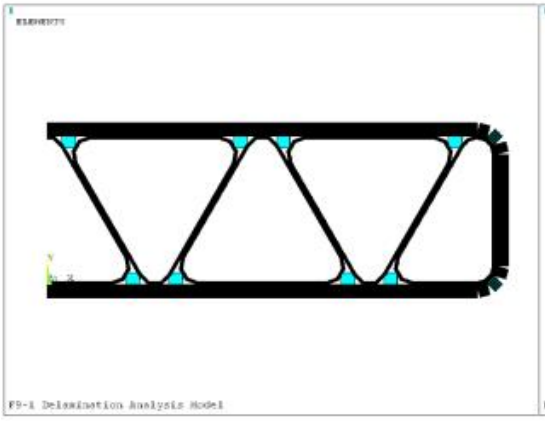

b. Front view

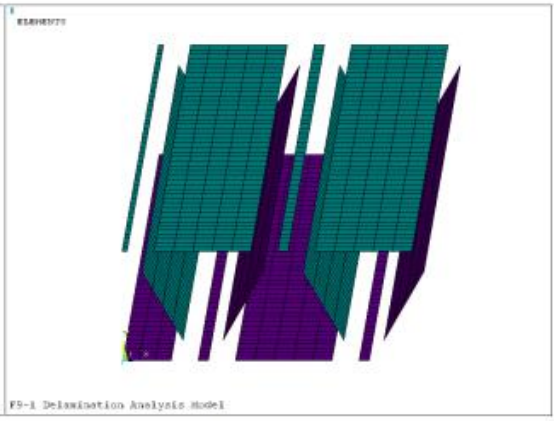

c. Contact pairs

Figure 4.49: Delamination analysis model of deck F9-1

4.3.2 Potential Delamination Zones

It is not feasible to predict the delamination onset load or to simulate delamination propagation of a FRP bridge deck based on available delamination analysis models. The argument for this conclusion is given as follows.

The advantage of CZM is its unification of delamination initiation and propagation within one model. On the other hand, the disadvantage of CZM is that extremely fine meshes are required to ensure a sufficient number of elements in the cohesive zone. If there are fewer elements in the cohesive zone, the distribution of tractions in front of the delamination tip cannot be represented accurately. The length of the cohesive zone (l_{cz}), defined as the distance from the delamination tip to the point where the maximum cohesive traction is reached, can be estimated by (Rice, 1980; Falk et al., 2001)

$$l_{cz} = \frac{9\pi}{32} E \frac{G_c}{(\tau^o)^2} \tag{4.20}$$

Where:

E = Young's modulus of the material

G_c = critical fracture energy

τ^o = maximum interfacial strength

The minimum number of elements required in the cohesive zone is still under discussion. Moës and Belytschko (2002) recommended using more than 10 elements; Falk et al. (2001) employed between 2 and 5 elements in their analyses; and, Mi et al. (1998) suggested using at least 2 elements.

For the second-generation and third-generation GFRP bridge decks, the cohesive zone length calculated using equation (4.20) was about 0.8 mm. Assuming only 2 elements were in the cohesive zone, the mesh size would be 0.4 mm, which is too small to implement for deck F7-2 and deck F9-1.

Travesa (2006) found that it was possible to simulate delamination propagation precisely by using coarse meshes and the adjusted constitutive models. The point was to lower the interfacial strengths artificially while keeping the critical fracture energies constant, which would result in the increase of the cohesive zone length and the improvement of the convergence rate of the solution. However, over-reduced interfacial strengths could lead to incorrect or unacceptable results, especially for complex delamination cases (Alfano and Crisfield, 2001). Travesa (2006) concluded that accurate analysis results could be attained with a mesh size 10 times larger than the mesh size calculated using the actual interfacial strengths. This technique could increase the mesh size of the two deck models from 0.4 mm to 4 mm, but the increased mesh size was still too small to put into practice.

The proposed delamination analysis model is approaching the limit of current finite element technology. The only solution left to obtain the delamination onset load and delamination propagation pattern of a FRP bridge deck is to introduce an advanced structural health monitoring system to the deck specimen. For example, Wang et al. (2001) sucessfully developed an active sensing diagnostic system with built-in diagnostics to detect delamination in composite structures.

Fortunately, the delamination analysis model can point out the potential delamination zones through plotting the contours of the contact sliding distance and the contact gap distance.

As described in Section 3.7.1, the final failure of deck F7-2 was signaled by the slippage of one triangular inside tube at the west end of the deck (Figure 3.10). Contact sliding distance and contact gap distance of deck F7-2 at the service load level (139 kN) are shown in Figure 4.50 and Figure 4.51, respectively. Comparing these two figures, it is easy to determine that the slip tangent to the interface was more detrimental than the separation normal to the interface. Although the circled areas in Figure 4.50 and Figure 4.51 had not delaminated yet at the service load level, it was conceivable that further development of these circled areas contributed to the final slippage of that triangular inside tube. As discussed in Section 4.2.5, the imperfection of the manufacturing process and lower level of quality control did make the delamination propagation much easier.

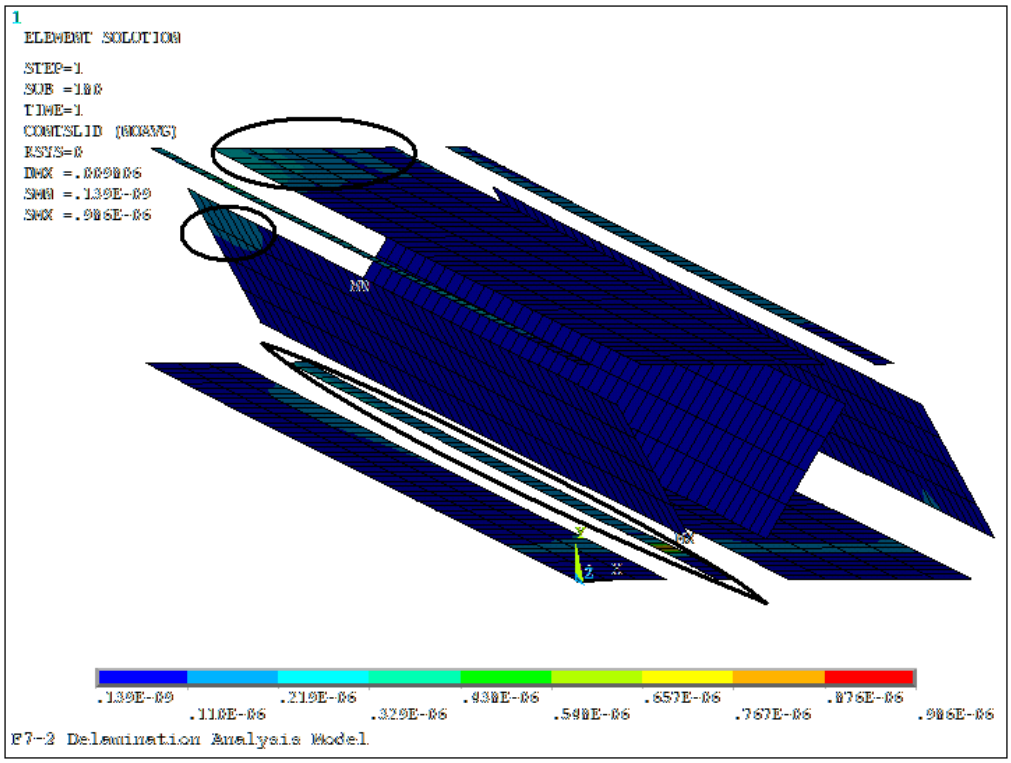

Figure 4.50: Contact sliding distance of deck F7-2 at the service load level

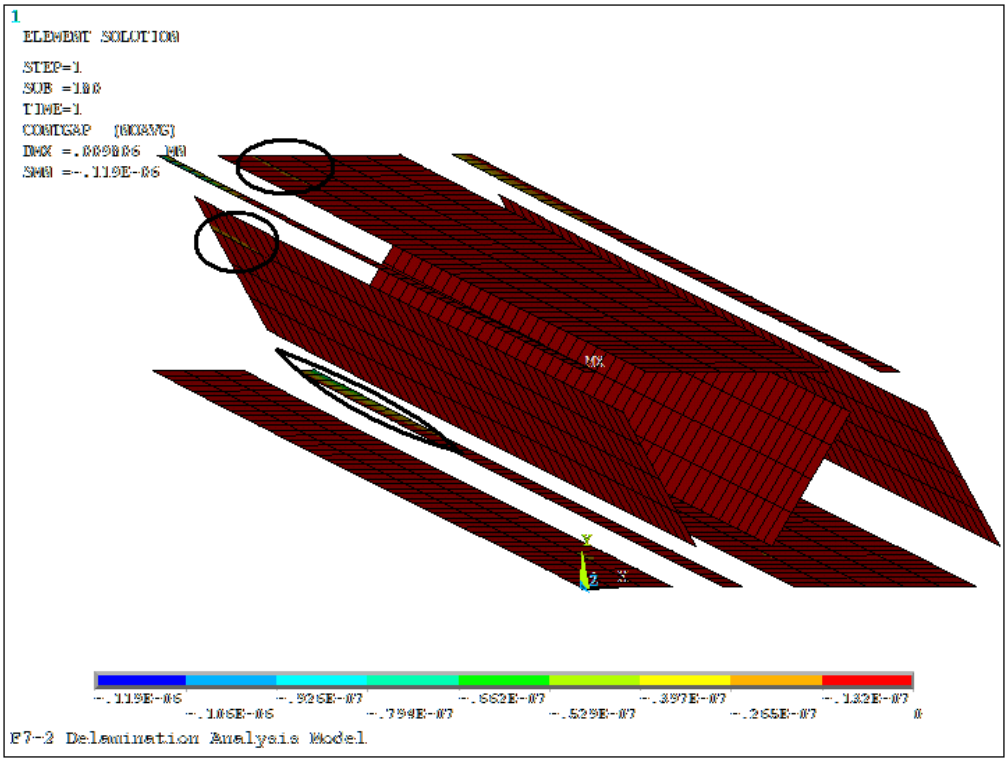

Figure 4.51: Contact gap distance of deck F7-2 at the service load level

The failure mode of deck F9-1 was delamination buckling between two of the middle triangular tubes (Figure 3.13). Contact sliding distance and contact gap distance of deck F9-1 at the service load level (139 kN) are shown in Figure 4.52 and Figure 4.53. Comparing these two figures, it is also noted that the slip tangent to the interface was more detrimental than the separation normal to the interface. The circled areas in Figure 4.52 and Figure 4.53 had not delaminated yet at the service load level, but it was conceivable that further development of these circled areas contributed to the final delamination between those two middle triangular tubes.

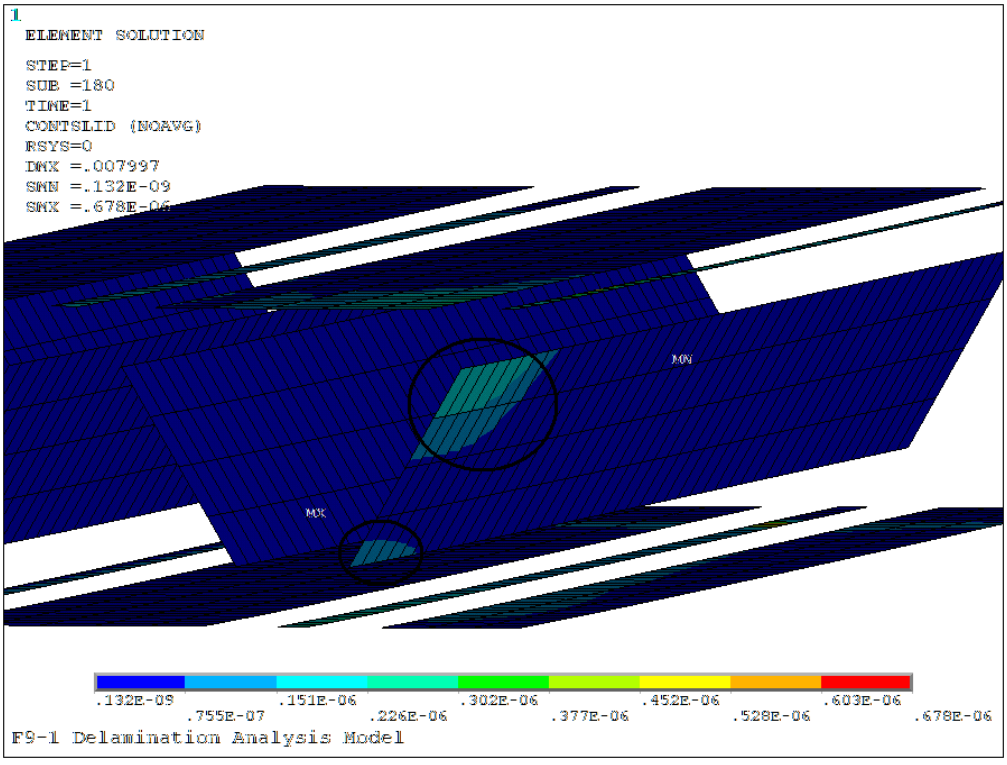

Figure 4.52: Contact sliding distance of deck F9-1 at the service load level

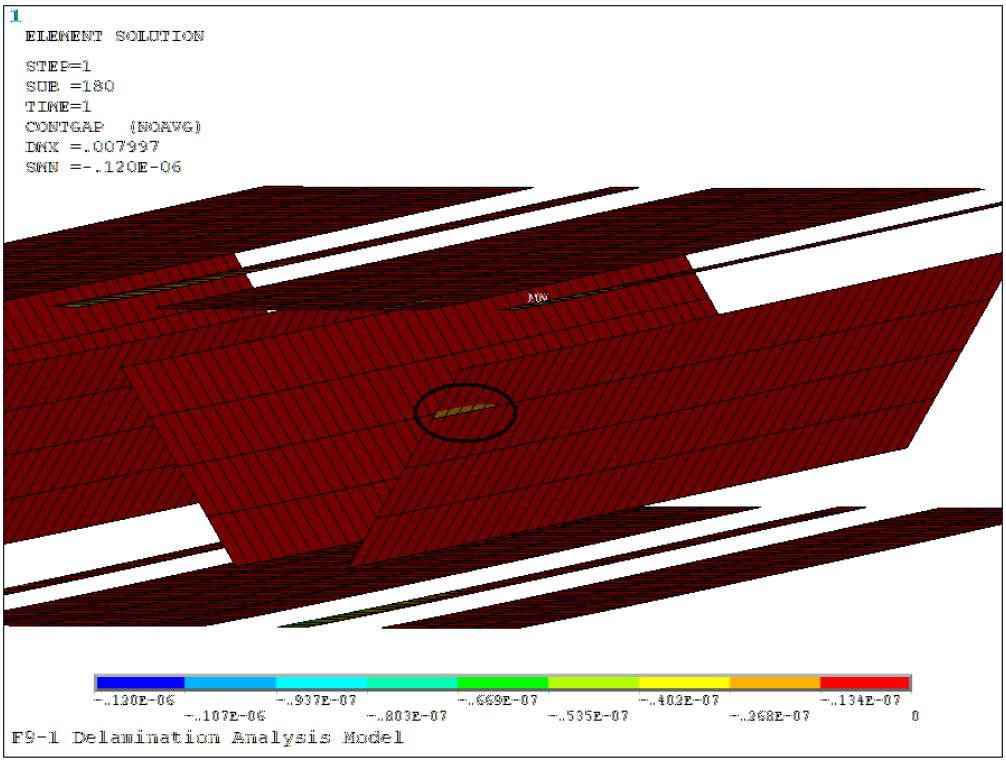

Figure 4.53: Contact gap distance of deck F9-1 at the service load level

Generally, the delamination analysis model can predict potential delamination zones successfully. This finding has two major benefits: first, it will help the FRP bridge deck manufacturers improve the quality control procedure in the potential areas of delamination; second, it presents to researchers an efficient and economical way to integrate the sensor network into the FRP bridge deck specimen in the future experimental testing.

Chapter 5

Conclusions and Recommendations

5.1 Conclusions

The structural behaviors of the second-generation (deck F7-2), third-generation (deck F9-1) and fourth-generation (deck F10-1) filament-wound GFRP bridge decks were experimentally investigated at the McQuade Structural Laboratory, The University of Manitoba. A systematic L&D method for analyzing FRP bridge decks was proposed in this thesis, which consisted of the linear analysis model and the delamination analysis model. A validation study of this L&D method was conducted based on the experimental results of these three generations of filament-wound GFRP bridge decks. Through comparing the experimental and theoretical results, the following conclusions can be drawn:

1. The load/deflection ratios of FRP bridge decks predicted by the linear analysis model were much closer to the experimental results than those predicted by the Classical Lamination Theory model.
2. The computed First-Ply Failure (FPF) loads of all the three decks were about 50 percent of their actual failure loads. Apparently, FPF did not result in the failure

of the whole FRP bridge deck. The load deflection relationships of the deck specimens could still behave linearly after exceeding the FPF loads.

3. It was extremely important to keep the service load below the FPF level in the design of FRP bridge decks.
4. The FPF analysis, based on the linear analysis model, was easy to carry out and required much less processing time than nonlinear analysis. It could be used as an indicator of lower bound failure criterion for the design of FRP bridge decks.
5. The linear analysis model could successfully predict the deflections and axial strains of a FRP bridge deck. However, the accuracies of the predicted deflections and axial strains at certain parts of the FRP bridge deck might be compromised due to the possibilities of lamina failure, delamination propagation, and structural buckling.
6. The linear analysis model could successfully predict the buckling failure load and the buckling mode shape of a FRP bridge deck on the condition that limited damage happened to the FRP bridge deck.
7. Because the eigenvalue buckling analysis always over-predicted the buckling failure loads, it could be used as an indicator of upper bound failure criterion for the design of FRP bridge decks.
8. It was not feasible to predict the delamination onset load or to simulate delamination propagation of a FRP bridge deck based on available delamination analysis models because of the requirement for extremely fine meshes.

9. The delamination analysis model could successfully point out the potential delamination zones through plotting the contours of the contact sliding distance and the contact gap distance.

The study strongly supported the validity of the proposed L&D method. This L&D method also could be applicable for FRP bridge decks manufactured by other processes, such as hand lay-up, VARTM, and pultrusion.

5.2 Recommendations for Future Work

For the further development in this research area, the following recommendations are worth consideration:

1. A new finite element model is needed to predict the delamination onset load and to simulate the delamination propagation of large composite structures used in the industry, such as FRP bridge decks.
2. An active sensing diagnostic system with a built-in network of piezoelectric materials is strongly recommended to monitor the extent and location of delamination within a FRP bridge deck.
3. The outcome of this thesis can be used for future development of FRP bridge deck design codes or guidelines.

References

Adams, D. F., Carlsson, L. A., and Pipes, R. B. (2003). *Experimental Characterization of Advanced Composite Materials* (3rd Edition ed.). Boca Raton, Florida, USA: CRC Press.

Alfano, G., and Crisfield, M. A. (2001). Finite element interface models for the delamination analysis of laminated composites: mechanical and computational issues. *International Journal for Numerical Methods in Engineering , 50* (7), 1701-1736.

ANSYS, Inc. (2007a). *ANSYS® Academic, Release 11.0, Help System, Elements Reference, Part I. Element Library.*

ANSYS, Inc. (2007b). *ANSYS® Academic, Release 11.0, Help System, Structural Guide, Chapter 7. Buckling Analysis.*

ANSYS, Inc. (2007c). *ANSYS® Academic, Release 11.0, Help System, Theory Reference, Chapter 15. Analysis Tools.*

ANSYS, Inc. (2007d). *ANSYS® Academic, Release 11.0, Help System, Theory Reference, Chapter 4. Structures with Material Nonlinearities.*

Aref, A. J., and Parsons, I. D. (2000). Design and performance of a modular fiber reinforced plastic bridge. *Composites Part B: engineering , 31* (6-7), 619-628.

Bhat, C. (2009, March 30). *Pultrusion process - composite manufacturing.* Retrieved January 18, 2010, from Scribd Web site: http://www.scribd.com/doc/13777193/pultrusion-process-composite-manufacturing

Creative Pultrusions, Inc. (2009, September 14). *SuperdeckTM Product Brochure.* Retrieved December 1, 2009, from Creative Pultrusions, Inc. Web site: http://www.creativepultrusions.com/LitLibrary/products/superdeck/brochure.pdf

Crocker, H. (2001). Photos about the fourth-generation of filament-wound GFRP bridge deck. Winnipeg, Manitoba, Canada.

Crocker, H. (2000). Photos about the third-generation of filament-wound GFRP bridge deck. Winnipeg, Manitoba, Canada.

Crocker, H., Shehata, E., Haldane-Wilsone, R., and Mufti, A. (2002). Innovative Fibre Reinforced Bridge Deck Modules. *The 3rd International Conference on Composites in Infrastructure.* San Francisco: University of Arizona.

Daniel, I. M., and Ishai, O. (1994). *Engineering Mechanics of Composite Materials* (1st Edition ed.). New York, NY, USA: Oxford University Press.

Dawood, M. (2003). *Development of a Transverse Connection for a Modular GFRP Bridge Deck.* The University of Manitoba, Department of Civil Engineering. Winnipeg: The University of Manitoba.

Falk, M. L., Needleman, A., and Rice, J. R. (2001). A critical evaluation of cohesive zone models of dynamic fracture. *Journal De Physique. IV , 11* (5), 543-550.

Federal Highway Administration. (2009, February 26). *National Bridge Inventory.* Retrieved August 2, 2009, from Federal Highway Administration: http://www.fhwa.dot.gov

Federal Highway Administration; Federal Transit Administration. (2006). *2004 Status of the Nation's Highways, Bridges, and Transit: Conditions and Performance.* Washington, DC: U.S. Department of Transportation.

Garg, A. C. (1988). Delamination - A Damage Mode In Composite Structures. *Engineering Fracture Mechanics , 29* (5), 557-584.

Gurit. (2009, July 13). *Composite Processing Within Manufacturing*. Retrieved January 17, 2010, from Gurit Web site: http://www.gurit.com/sector_introduction.asp?section=0001000100280010&itemTitle=Composite+Processing

Kansas Structural Composites, Inc. (1999, January 21). *Home page of Kansas Structural Composites, Inc.* Retrieved August 10, 2009, from Kansas Structural Composites, Inc. Web site: http://www.ksci.com

Kopeliovich, D. (2009, May 16). *Pultrusion*. Retrieved August 2, 2009, from SubsTech: http://www.substech.com/dokuwiki/doku.php?id=pultrusion

Lee, S. M. (1989). *Reference Book for Composites Technology* (1st ed., Vol. I). Lancaster, PA, USA: Technomic Publishing Company, Inc.

Mallick, P. (1993). *Fiber-Reinforced Composites: Materials, Manufacturing, and Design* (2nd ed.). New York, NY, USA: Marcel Dekker, Inc.

Martin Marietta Composites. (2005, October 25). *DuraSpan® Brochure.* Retrieved August 9, 2009, from Martin Marietta Materials Web site: http://www.martinmarietta.com/Products/pdf_DuraspanV2.pdf

Mi, Y., Crisfield, M. A., Davies, G., and Hellweg, H. B. (1998). Progressive delamination using interface elements. *Journal of Composite Materials , 32* (14), 1246-1272.

Moës, N., and Belytschko, T. (2002). Extended finite element method for cohesive crack growth. *Engineering fracture mechanics , 69* (7), 813-833.

Newhook, J., and Svecova, D. (2007). *Reinforcing Concrete Structures with Fibre Reinforced Polymers.* Winnipeg, MB: ISIS Canada Corporation.

O'Connor, J. S. (2008). GRP bridge decks and superstructures in the USA. *Reinforced Plastics , 52* (6), 26-31.

Parsons, I. D., White, S., Therriault, D., and Bignell, J. (2002). *Manufacture and Testing of a Filament Wound Composite Bridge Superstructure.* University of Illinois at Urbana-Champaign, Department of Civil and Environmental Engineering. Washington, DC: Transportation Research Board.

Plastic Plus, Inc. (2009, August 7). *Materials*. Retrieved February 21, 2010, from Plastic Plus, Inc. Web site: http://www.plasticplus.com/material/1_materials.html

Prel, Y., Davies, P., Benzeggagh, M. L., and De Charenteney, F. X. (1989). Mode I and Mode II Delamination of Thermosetting and Thermoplastic Composites. *Composite materials: fatigue and fracture, ASTM STP 1012 , 2*, 251–269.

Reeve, S. R. (2002, December 17). *FRP Composite Bridge Decks: Barriers to Market Development.* Retrieved January 27, 2010, from National Composite Center Web site: http://www.compositecenter.org/resources/NCC%20paper%20for%20CFC%20Polymer%20Conf%20v3.pdf

Rice, J. (1980). The Mechanics of Earthquake Rupture. In A. Dziewonski, and E. Boschi, *Physics of the Earth's Interior* (pp. 555-649). Amsterdam, North Holland, Netherlands: North-Holland Pub. Co.

Sams, M. (2005). Broadway Bridge Case Study: Bridge Deck Application of Fiber-Reinforced Polymer. *Journal of the Transportation Research Board* , 175–178.

Shehata, E., and Mufti, A. (2007). Development of a glass-fiber-reinforced-polymer bridge deck system. *Canadian Journal of Civil Engineering , 34* (3), 453-462.

Tang, B. M. (2003). FRP Composites Technology Brings Advantages to the American Bridge Building Industry. *The 2nd International Workshop on Structural Composites for Infrastructure Applications.* Cairo, Egypt.

Telang, N. M., Dumlao, C., Mehrabi, A. B., Ciolko, A. T., and Gutierrez, J. (2006). *Field Inspection of In-Service FRP Bridge Decks.* Washington, DC: Transportation Research Board.

Travesa, A. (2006). *Simulation of Delamination in Composites under Quasi-Static and Fatigue Loading using Cohesive Zone Models.* University of Girona, Department of Mechanical Engineering and Industrial Construction. Girona: University of Girona.

Wang, C. S., Wu, F., and Chang, F.-K. (2001). Structural health monitoring from fiber-reinforced composites to steel-reinforced concrete. *Smart Materials and Structures , 10* (3), 548-552.

Williams, B. (2000b). Photos about the second-generation of filament-wound GFRP bridge deck. Winnipeg, Manitoba, Canada.

Williams, B. (2000a). *The Development of GFRP Bridge Deck Modules.* The University of Manitoba, Department of Civil Engineering. Winnipeg, MB: The University of Manitoba.

Zureick, A. H., Shih, B., and Munley, E. (1995). Fiber-Reinforced Polymeric Bridge Decks. *Structural Engineering Review , 7* (3), 257-266.

Appendixes

Appendix A: Instrumentation for the second-generation GFRP bridge deck

There were fourteen 6 mm long electrical resistance strain gauges installed on the top and bottom plates of the second-generation GFRP bridge deck. Thirteen strain gauges were placed in the longitudinal direction of the deck; one strain gauge was placed in the transverse direction of the deck.

Three LVDTs were installed at the midspan of the deck to measure the midspan deflection. Another LVDT was positioned at the west support, and its readings were useful in determining the net midspan deflection.

The instrumentation layout of deck F7-2 can be found in Figure A.1, Figure A.2 and Figure A.3. Note that all the dimensions in these figures are in millimeters.

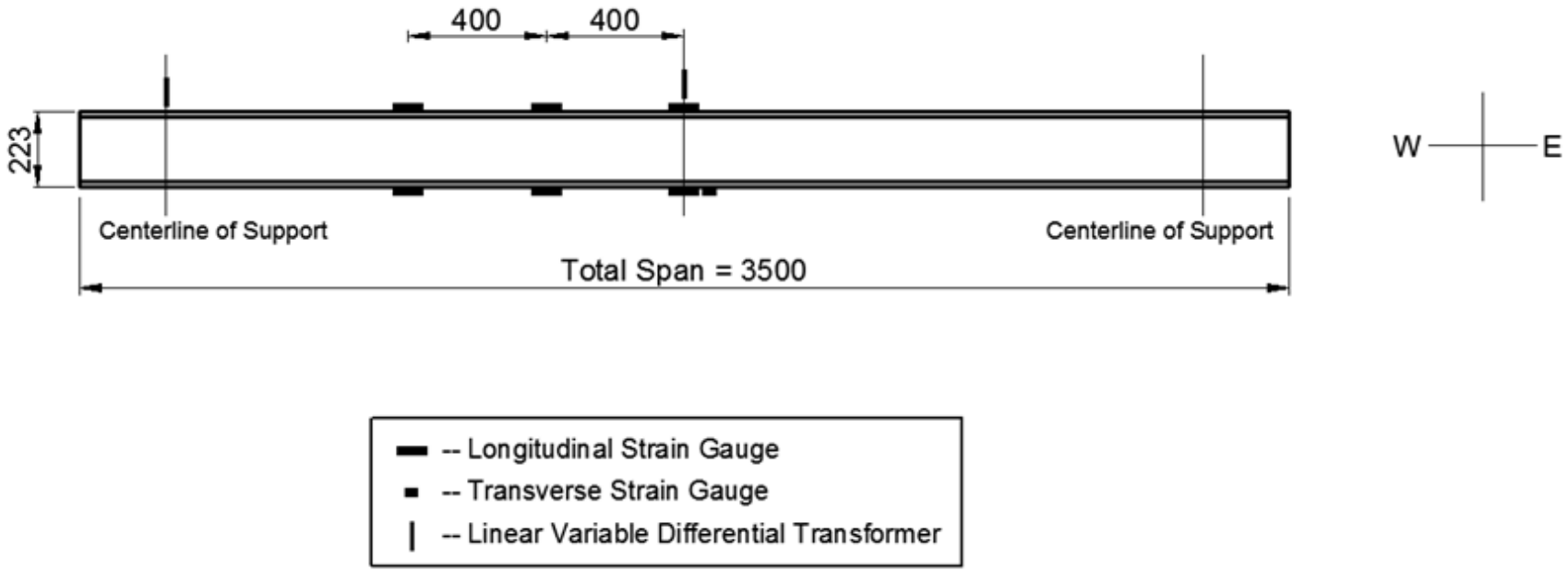

Figure A.1: Elevation view of the instrumentation layout of deck F7-2 (adapted from Williams, 2000b)

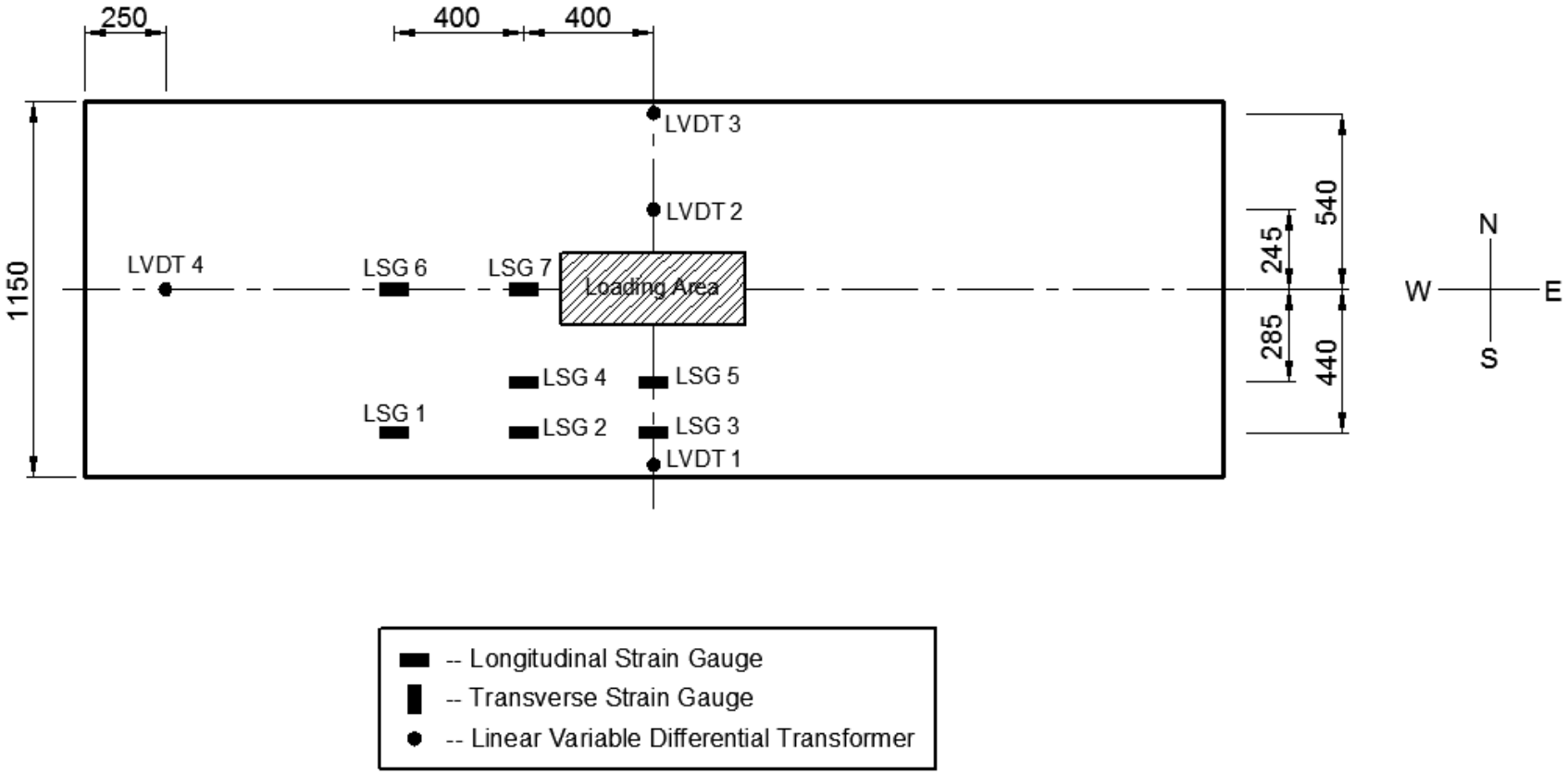

Figure A.2: Top view of the instrumentation layout of deck F7-2 (adapted from Williams, 2000b)

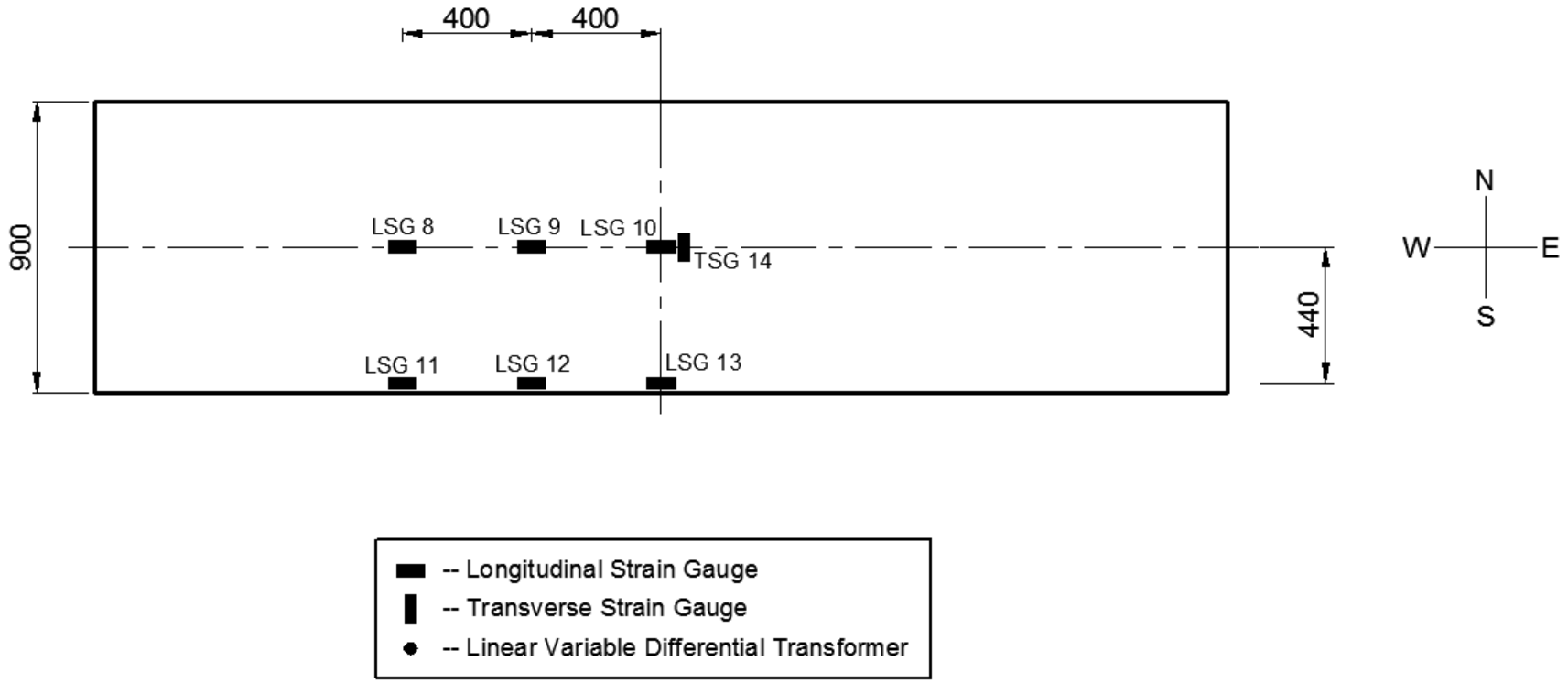

Figure A.3: Bottom view of the instrumentation layout of deck F7-2 (adapted from Williams, 2000b)

Appendix B: Instrumentation for the third-generation GFRP bridge deck

Fifteen electrical resistance strain gauges were installed on the top and bottom plates of the third-generation GFRP bridge deck. Only one strain gauge was placed in the transverse direction of the deck; the other fourteen strain gauges were placed in the longitudinal direction of the deck.

Four LVDTs were installed on the surface of the top plate. Three of them were placed at the midspan and another one was placed at the west support. This arrangement of LVDTs was to obtain the net midspan deflection.

The instrumentation layout of deck F9-1 can be found in Figure B.1, Figure B.2 and Figure B.3. Note that all the dimensions in these figures are in millimeters.

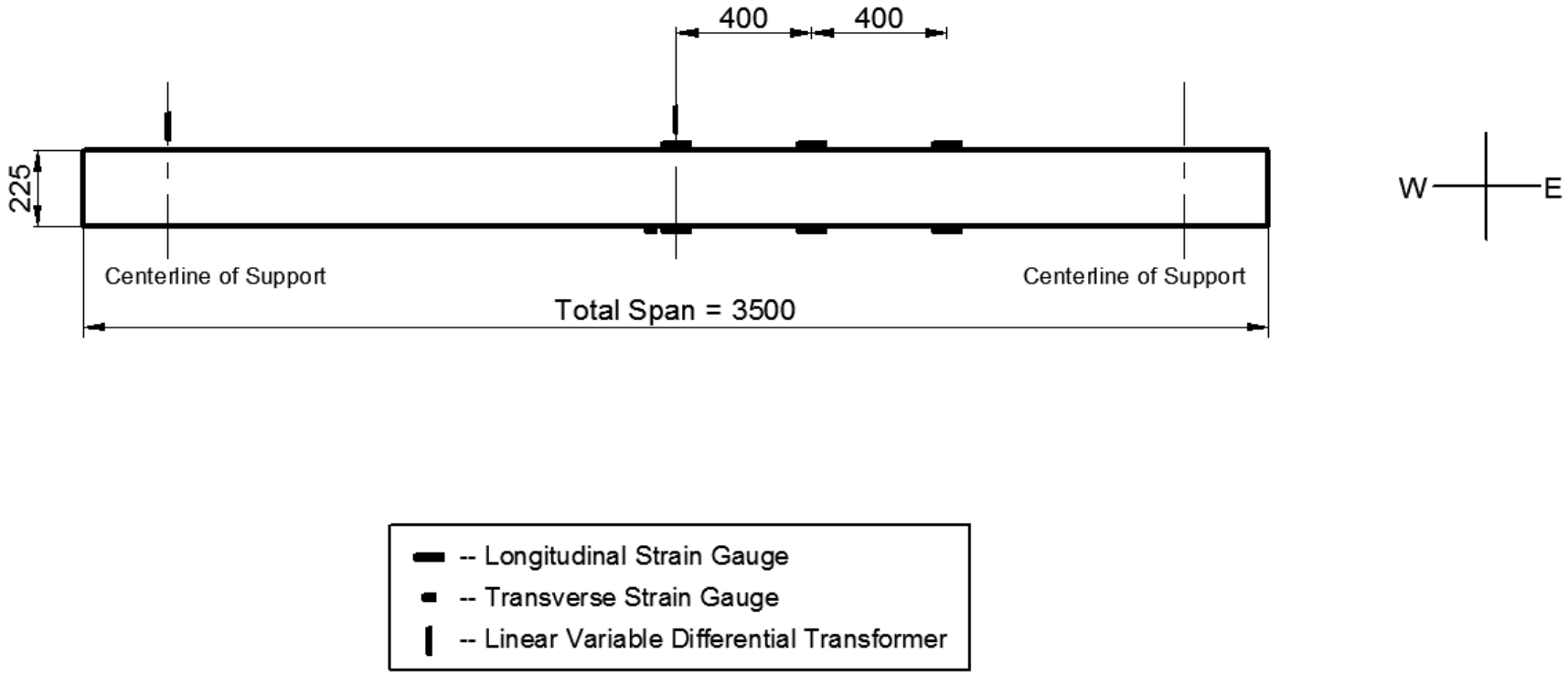

Figure B.1: Elevation view of the instrumentation layout of deck F9-1 (adapted from Crocker, 2000)

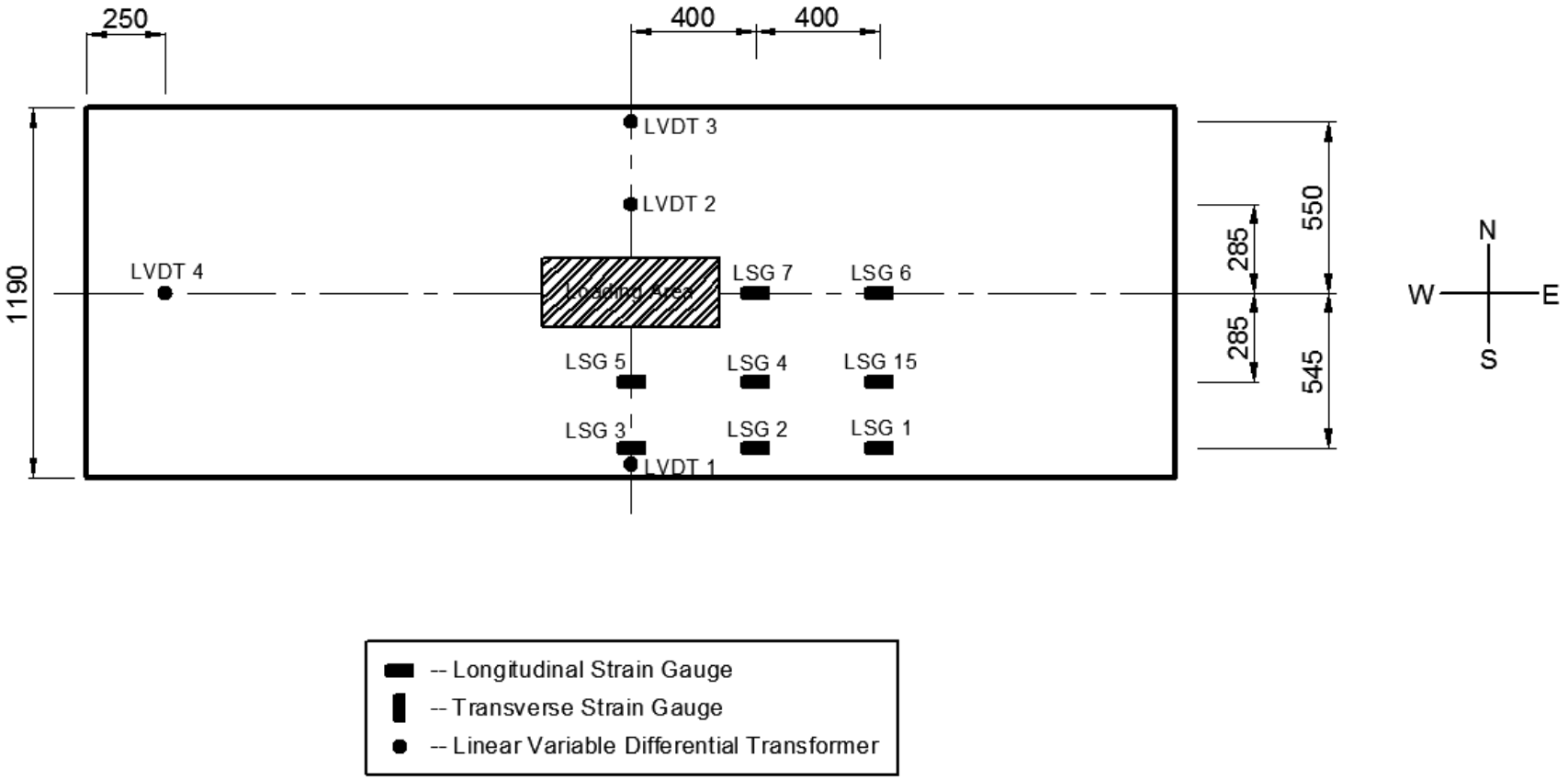

Figure B.2: Top view of the instrumentation layout of deck F9-1 (adapted from Crocker, 2000)

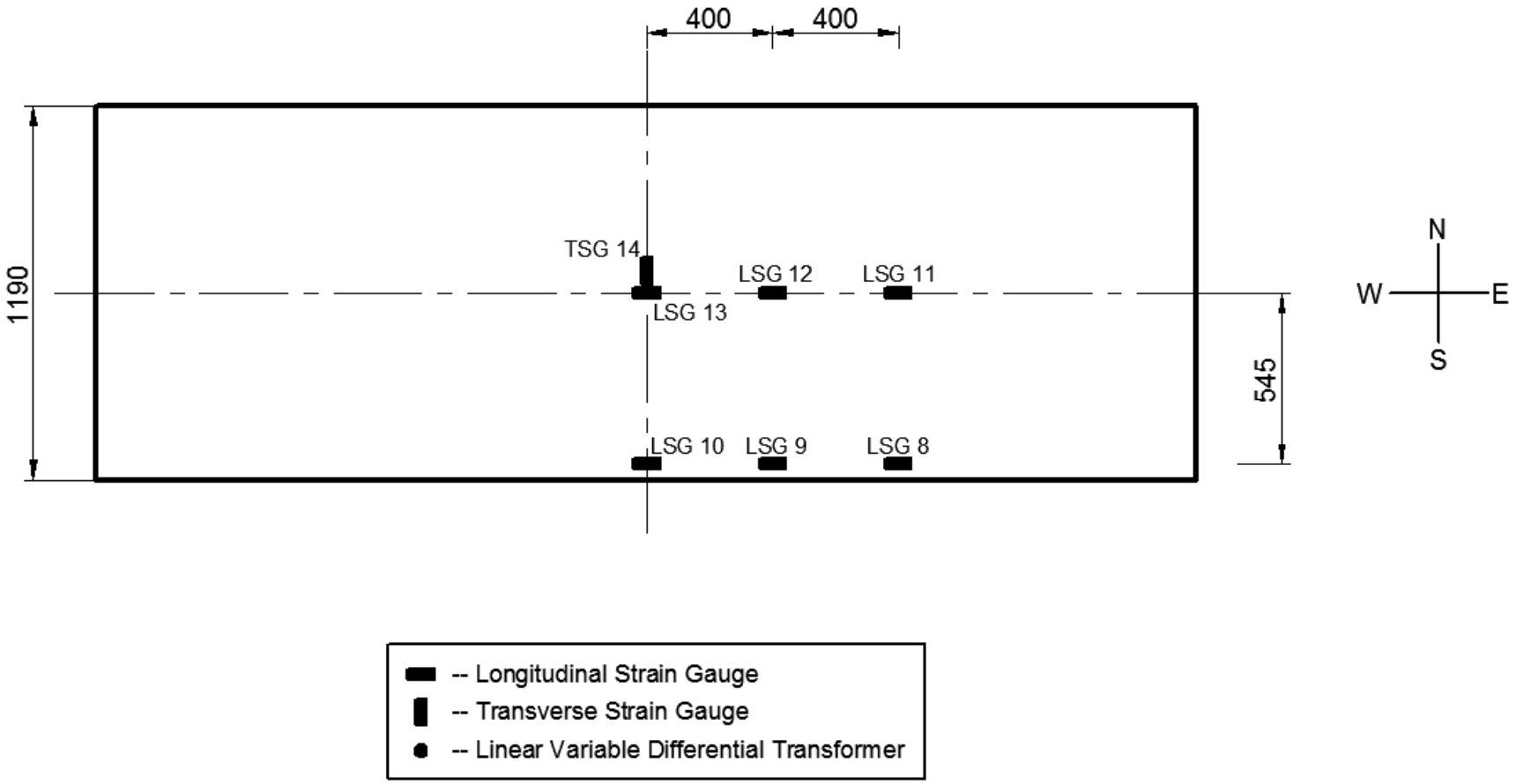

Figure B.3: Bottom view of the instrumentation layout of deck F9-1 (adapted from Crocker, 2000)

Appendix C: Instrumentation for the fourth-generation GFRP bridge deck

Twenty-four electrical resistance strain gauges and three fiber optic sensors were installed on the fourth-generation GFRP bridge deck. Because the data collected from strain gauges and fiber optic sensors were not published elsewhere and several strain gauges and fiber optic sensors were broken during installation, only LVDTs were shown in the instrumentation layout of the fourth-generation GFRP deck.

The arrangement of LVDTs was similar to the second-generation and third-generation GFRP bridge decks. In order to determine the net midspan deflection, three LVDTs were positioned at the midspan and another one was positioned at the west support.

The instrumentation layout of deck F10-1 can be found in Figure C.1 and Figure C.2. Note that all the dimensions in these figures are in millimeters.

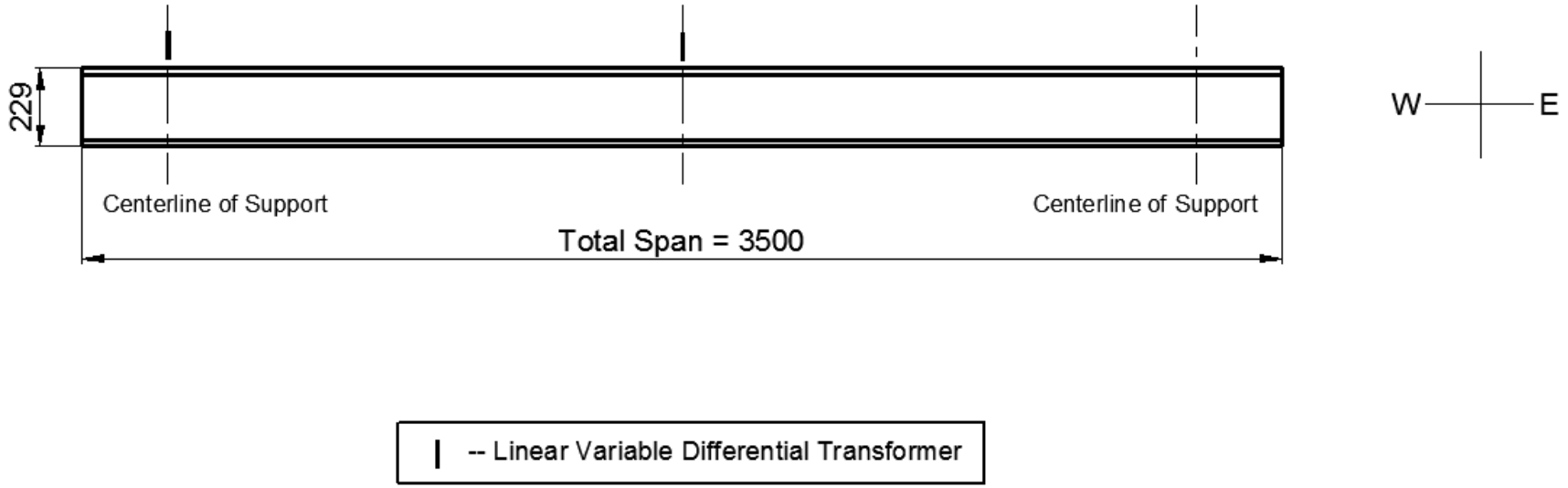

Figure C.1: Elevation view of the instrumentation layout of deck F10-1 (adapted from Crocker, 2001)

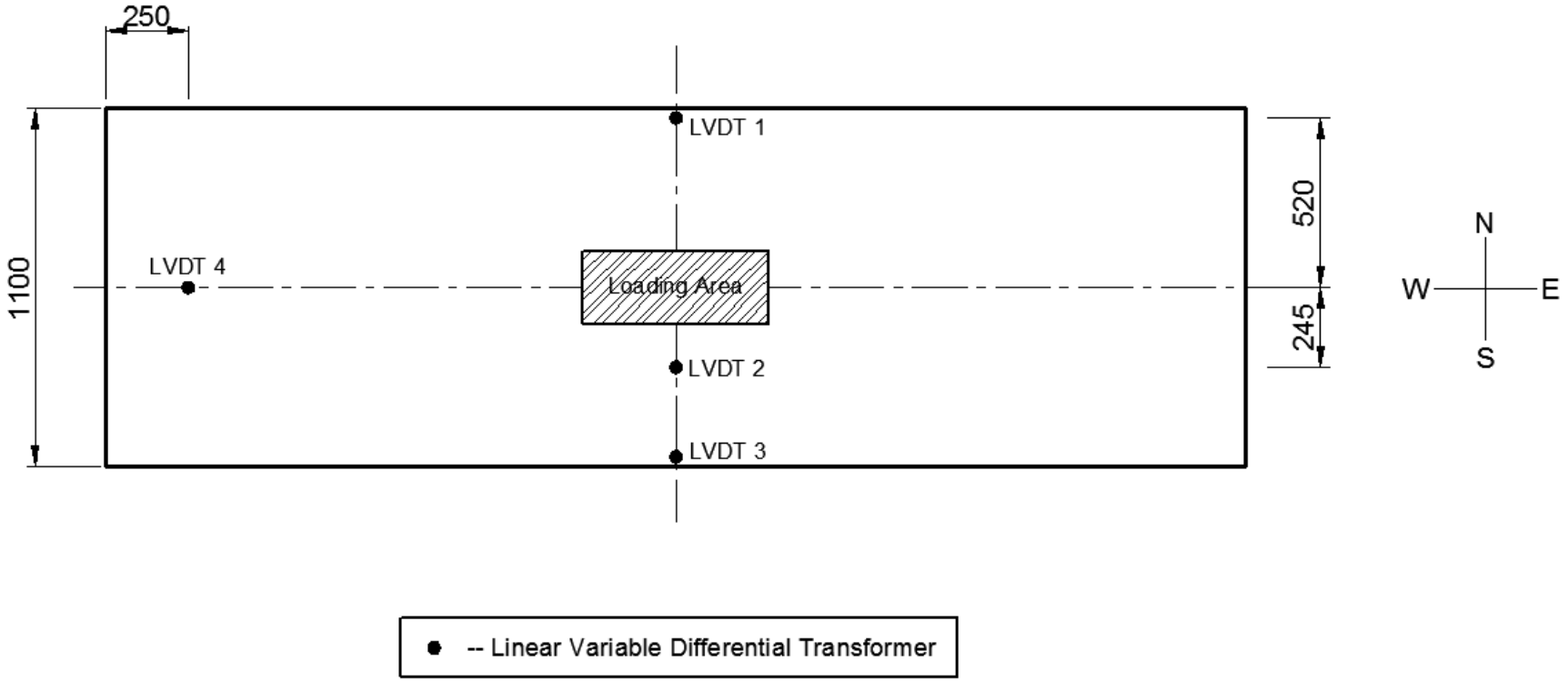

Figure C.2: Top view of the instrumentation layout of deck F10-1 (adapted from Crocker, 2001)